Dissertation

Influence of Hexokinase 1 Rings on Mitochondrial Function During Energy Stress

submitted by

BSc MSc

Johannes Pilic

for the Academic Degree of

Doctor of Philosophy (PhD)

at the

Medical University of Graz

Gottfried Schatz Research Center

Molecular Biology and Biochemistry

under the Supervision of

Assoz. Prof. Priv.-Doz. Mag. Pharm. Dr. rer. nat. Roland Malli

2024

Declaration

I hereby declare that this thesis is my own original work and that I have fully acknowledged by name all of those individuals and organizations that have contributed to the research for this thesis. Due acknowledgment has been made in the text to all other material used. Throughout this thesis and in all related publications I followed the “Standards of Good Scientific Practice and Ombuds Committee at the Medical University of Graz”.

Zurich, August 13th, 2024 *Johannes Pilic*

Disclosures

Part of this thesis has been published in:

Pilic J, Gottschalk B, Bourgeois B, Habisch H, Koshenov Z, Oflaz FE, Erdogan YC, Miri SM, Yiğit EN, Aydın MŞ, Öztürk G, Eroglu E, Shoshan-Barmatz V, Madl T, Graier WF, and Malli R. Hexokinase 1 forms rings that regulate mitochondrial fission during energy stress. *Molecular Cell.* 2024. https://doi.org/10.1016/j.molcel.2024.06.009

Pilic J, Oflaz FE, Gottschalk B, Erdogan YC, Graier WF, Malli R. Visualizing interactions of VDAC1 in live cells using a tetracysteine tag. *bioRxiv*. 2023. https://doi.org/10.1101/2023.09.08.556841

The following co-authors contributed to my first-author publications:

Benjamin Gottschalk[1], Benjamin Bourgeois[2,3], Hansjörg Habisch[3], Zhanat Koshenov[1], Furkan E. Oflaz[1], Yusuf C. Erdogan[1], Seyed M. Miri[4,5], Esra N. Yiğit[4,6], Mehmet Ş. Aydın[4], Gürkan Öztürk[4], Emrah Eroglu[4,6], Varda Shoshan-Barmatz[7], Tobias Madl[2,3], Wolfgang F. Graier[1,2], and Roland Malli[1,2]

[1] Gottfried Schatz Research Center, Molecular Biology and Biochemistry, Medical University of Graz, Neue Stiftingtalstraße 6/4 8010, Graz, Austria

[2] BioTechMed Graz, Mozartgasse 12/2, 8010, Graz, Austria

[3] Otto Loewi Research Center, Medicinal Chemistry, Medical University of Graz, 8010 Graz, Austria

[4] Regenerative and Restorative Medicine Research Center (REMER), Research Institute for Health Sciences and Technologies (SABITA), Istanbul Medipol University, Istanbul 34810, Türkiye

[5] Molecular Biology, Genetics and Bioengineering Program, Faculty of Engineering and Natural Sciences, Sabanci University, Istanbul 34956, Türkiye

[6] Department of Physiology, International School of Medicine, Istanbul Medipol University, Istanbul 34810, Türkiye

[7] Department of Life Sciences and the National Institute for Biotechnology in the Negev, Ben-Gurion University of the Negev, Beer-Sheva 84105, Israel

I confirm that all co-authors have agreed to use their data in my thesis. I have obtained permissions to reproduce the figures from my publications in my thesis.

During my PhD thesis, I contributed to the following publications:

Koshenov Z, Oflaz FE, Hirtl M, **Pilic J**, Bachkoenig OA, Gottschalk B, Madreiter-Sokolowski CT, Rost R, Malli R, Graier WF. Sigma-1 Receptor Promotes Mitochondrial Bioenergetics by Orchestrating ER Ca^{2+} Leak during Early ER Stress. *Metabolites*. 2021; 11(7):422. https://doi.org/10.3390/metabo11070422

Luschnig P, Kienzl M, Roula D, **Pilic J**, Atallah R, Heinemann A, Sturm EM. The JAK1/2 inhibitor baricitinib suppresses eosinophil effector function and restricts allergen-induced airway eosinophilia. *Biochemical Pharmacology.* 2021; 192:114690. https://doi.org/10.1016/j.bcp.2021.114690

Secilmis M, Altun HY, **Pilic J**, Erdogan YC, Cokluk Z, Ata BN, Sevimli G, Zaki AG, Yigit EN, Öztürk G, Malli R, Eroglu E. A Co-Culture-Based Multiparametric Imaging Technique to Dissect Local H_2O_2 Signals with Targeted HyPer7. *Biosensors*. 2021; 11(9):338. https://doi.org/10.3390/bios11090338

Reichmann F, **Pilic J**, Trajanoski S, Norton WHJ. Transcriptomic underpinnings of high and low mirror aggression zebrafish behaviours. *BMC Biol*, 2022; 20(1):97. https://doi.org/10.1186/s12915-022-01298-z

Curcic S, Erkan-Candag H, **Pilic J**, Malli R, Wiedner P, Tiapko O, Groschner K. TRPC3 governs the spatiotemporal organization of cellular Ca^{2+} signatures by functional coupling to IP3 receptors. *Cell Calcium*, 2022; 108:102670. https://doi.org/10.1016/j.ceca.2022.102670

Acknowledgments

PhD student, Johannes Pilic, received funding from the Austrian Science Fund (FWF, I3716-B27 to Roland Malli) and the Medical University of Graz through the PhD Program Molecular Medicine MOLMED. The Results section, for the most part, represent already published work listed as Pilic *et al*., 2024[184] and *Pilic et al*., 2023[185] in the Reference section.

Danksagung

Zuallererst möchte ich meinem Mentor, Roland Malli, für seine ständige Unterstützung, gute Laune und Geduld vom Herzen danken. Ich hätte mir keinen besseren Mentor wünschen können.

Weine Wertschätzung möchte ich auch den Mitgliedern meines Dissertationskomitees, Wolfgang Graier, Corina Madreiter-Sokolowski und Varda Shoshan-Barmatz, ausdrücken. Auch bei meinen Kollaborationspartnern möchte ich mich bedanken, insbesondere bei Tobias Madl und Emrah Eroglu. Euer aufschlussreiches Feedback hat maßgeblich zur Verbesserung meiner Arbeit beigetragen.

Herzlichst danke ich meinen geschätzten Kollegen, die zur fröhlich entspannten Arbeitsatmosphäre beigetragen haben und mir bei verschiedenen Methoden zur Seite standen. Ein besonderer Dank geht an Benjamin Gottschalk für seine stetige Hilfe, Erklärungen und anregenden Diskussionen. Die schöne Zeit bei diversen Feiern, Ausflügen und Abenden mit euch allen werde ich gerne in Erinnerung behalten.

Meiner Familie und der Familie meiner geliebten Partnerin bin ich äußerst dankbar für ihre Unterstützung, Liebe und ihren Glauben an mich bedanken.

Schließlich möchte ich meiner wundervollen Partnerin, Kathi Rauch, meinen tiefsten Dank aussprechen. Deine bedingungslose Liebe, aufbauenden Worte und Verständnis haben mir viel Kraft gegeben.

Table of contents

List of Abbreviations

2-DG	2-Deoxyglucose
3BP	3-Bromopyruvate
AMPK	AMP-activated protein kinase
AR	Aspect Ratio
ATP	Adenosine Triphosphate
BAK	Bcl-2 homologous antagonist/killer
BFP	Blue Fluorescent Protein
CFP	Cyan Fluorescent Protein
CTP	Cytidine Triphosphate
DMEM	Dulbecco's Modified Eagle Medium
DNA	Deoxyribonucleic Acid
Drp1	Dynamin-related protein 1
ECAR	Extracellular Acidification Rate
ER	Endoplasmic Reticulum
FCCP	Carbonyl cyanide-p-trifluoromethoxyphenylhydrazone
FCS	Fetal Calf Serum
FF	Form Factor
FlAsH	Fluorescein arsenical hairpin binder
FP	Fluorescent Protein
GAPDH	Glyceraldehyde 3-phosphate dehydrogenase
G6P	Glucose-6-Phosphate
GFP	Green Fluorescent Protein
Glk1	Glucokinase 1
HDCR	High Data Rate
HK	Hexokinase

HKDC1	Hexokinase Domain-Containing 1
HeLa	Henrietta Lacks (cell line)
INS-1	Insulinoma 1 (cell line)
DNA	Deoxyribonucleic Acid
MBD	Mitochondrial Binding Domain
MICU1	Mitochondrial Calcium Uptake 1
MCF-7	Michigan Cancer Foundation-7 (cell line)
MOAS	Mitochondria on a string
mRNA	Messenger Ribonucleic Acid
mCh	mCherry
NLRP3	NOD-like receptor pyrin domain-containing 3
NMR	Nuclear Magnetic Resonance
OCR	Oxygen Consumption Rate
OMM	Outer Mitochondrial Membrane
PBS	Phosphate-Buffered Saline
ReAsH	Resorufin Arsenical Hairpin binder
RFP	Red Fluorescent Protein
sfGFP	Superfolder Green Fluorescent Protein
SH-SY5Y	Human neuroblastoma cell line
TC	Tetracysteine
TBS	Tris Buffered Saline
TMRM	Tetramethylrhodamine Methyl Ester
VDAC1	Voltage-Dependent Anion Channel 1
YFP	Yellow Fluorescent Protein

List of Figures and Tables

Zusammenfassung

Unsere Zellen sind ständigen Schwankungen in der Verfügbarkeit von Nährstoffen ausgesetzt. Wie Zellen mit diesen Herausforderungen meistern, ist noch nicht vollständig geklärt. Jüngste Forschungsergebnisse deuten darauf hin, dass Stoffwechselenzyme in der Lage sind, sich schnell an Veränderungen der Nährstoffverfügbarkeit anzupassen.

In der ersten Hälfte meiner Doktorarbeit entdeckten wir, dass das erste glykolytische Enzym, Hexokinase 1 (HK1), bei Glukoseentzug Ringe um Mitochondrien bildet. HK1 katalysiert die ATP-abhängige Phosphorylierung von Glukose zu Glukose-6-Phosphat (G6P). Unsere Experimente haben gezeigt, dass die Abwesenheit von ATP und G6P, und nicht von Glukose an sich, die Bildung von HK1-Ringen fördert. Wir beobachteten, dass HK1-Ringe Mitochondrien an Kontaktstellen mit dem Endoplasmatischen Retikulum (ER) und MiD51, einem Rezeptor der mitochondrialen Teilungsmaschinerie, einschnüren. Überraschenderweise förderten die einschnürenden HK1-Ringe die mitochondriale Teilung nicht. Stattdessen hemmten die HK1-Ringe die mitochondriale Teilung, indem sie das wichtigste Spaltprotein, Drp1, vom Pro-Spaltrezeptor Mff verdrängten. In Zusammenarbeit mit Experten für Strukturbiologie haben wir Mutationen identifiziert, die die Bildung von HK1-Ringen verhindern oder fördern. Anhand dieser Mutationen konnten wir zeigen, dass HK1-Ringe den mitochondrialen Stoffwechsel bei Energiestress regulieren. Diese Ergebnisse deuten darauf hin, dass HK1 ein neuartiger mitochondrialer Energiestresssensor ist, der die Form und Stoffwechselaktivität von Mitochondrien reguliert.

In der zweiten Hälfte meiner Doktorarbeit konzentrierten wir uns auf den Voltage-dependent anion channel 1 (VDAC1), einer wichtigen Pore in der äußeren Mitochondrienmembran, der nachweislich mit HK1 interagiert. Im Vergleich zu HK1 war VDAC1 mit herkömmlichen Methoden in lebenden Zellen nur schwer sichtbar zu machen. Wir haben das Problem der Visualisierung von VDAC1 überwunden, indem wir es mit dem Tetracystein (TC)-Motiv markierten, das mit spezifischen Farbstoffen angefärbt werden kann. Dieser Ansatz zeigte, dass TC-markiertes VDAC1 eine clusterartige Verteilung auf Mitochondrien aufweist. Ähnlich wie bei HK1 befanden sich die meisten VDAC1-Cluster an Kontaktstellen mit dem ER. Allerdings wurde während des Glukoseentzugs keine signifikante Kolokalisierung zwischen VDAC1 und HK1 beobachtet, was darauf hindeutet, dass diese Proteine mit unterschiedlichen Regionen des ER interagieren. Unsere Ergebnisse zeigen, dass der TC-Tag für die Bildgebung von VDAC1 in lebenden Zellen geeignet ist.

Abstract

Our cells experience constant fluctuations in nutrient availability. How cells deal with these challenges is incompletely understood. Recent research indicates that metabolic enzymes are able to adapt quickly to changes in nutrient availability.

During the first half of my PhD, we discovered that the first glycolytic enzyme, hexokinase 1 (HK1), forms rings around mitochondria during glucose depletion. HK1 catalyzes the ATP-dependent phosphorylation of glucose to glucose-6-phosphate (G6P). Our experiments have revealed that the absence of ATP and G6P, and not glucose per se, drives the formation of HK1-rings. HK1-rings were observed to constrict mitochondria at contact sites with the endoplasmic reticulum (ER) and MiD51, a receptor of the mitochondrial division machinery. Surprisingly, the constricting HK1-rings did not promote mitochondrial division. Instead, HK1-rings inhibited mitochondrial division by displacing the major fission protein, Drp1, from the pro-fission receptor, Mff. In collaboration with experts in structural biology, we identified mutations that prevented or promoted the formation of HK1-rings. By using these mutations, we showed that HK1-rings regulate mitochondrial metabolism during energy stress. These findings suggest that HK1 is a novel mitochondrial energy stress sensor that regulates the morphology and metabolic activity of mitochondria.

During the second half of my PhD, we focused on the voltage-dependent anion channel 1 (VDAC1), an essential mitochondrial transporter, that has been shown to interact with HK1. Compared to HK1, VDAC1 was difficult to visualize with conventional approaches in living cells. We overcame the problem of visualizing VDAC1 by tagging it with the tetracysteine (TC) motif that can be stained with specific dyes. This approach revealed that TC-tagged VDAC1 had a cluster-like distribution on mitochondria. Similar to HK1, the majority of VDAC1-clusters were located at contact sites with the ER. However, no significant colocalization between VDAC1 and HK1 was observed during glucose depletion, suggesting that these proteins interact with different regions of the ER. Our results demonstrate that the TC-tag is suitable for live-cell imaging of VDAC1.

1 Introduction

1.1 Metabolic enzymes can have more than one function

The human proteome comprises approximately 20,000 proteins.[1] Initially, it was assumed that one protein has one function, but this view became outdated and researchers recognized that proteins can and must have multiple functions to maintain human physiology. Among the first proteins identified to have multiple functions were crystallins. Crystallins make up large portions of the eye lens and are essential for cellular transparency.[2] In 1982 Ingolia and Craig identified that heat shock proteins in *Drosophila* had unexpected protein sequence similarities to mammalian α-crystallins.[3] This resemblance prompted inquiries into the evolutionary links between these protein classes. Surprisingly, α-crystallin was expressed in other tissues beyond the eye lens.[4–6] Another surprising finding was that crystallins are identical to metabolic enzymes. For example, the ε-crystallin from birds and reptiles is the same as lactate dehydrogenase.[7–9] These findings suggested that a single gene could give rise to proteins with at least dual functions, challenging the conventional understanding of proteins having single functions. The term 'moonlighting' was suggested to describe proteins that have multiple functions.[10] There are over 250 entries of moonlighting human proteins (http://moondb.hb.univ-amu.fr). Moonlighting proteins commonly translocate to other subcellular compartments and perform diverse functions. For example, the glycolytic enzyme glyceraldehyde 3-phosphate dehydrogenase (GAPDH) translocates into the nucleus during glucose starvation.[11] In the nucleus, GAPDH interacts with the histone deacetylase Sirtuin 1 and activates autophagy.[11] Moonlighting enzymes can also bind directly to DNA to regulate gene transcription, which was comprehensively reviewed by Boukouris, Zervopoulos, and Michelakis in 2016.[12] The change in interaction partners is another common moonlighting function. Another example is the mitochondrial protein cytochrome c which functions as an electron carrier. However, changes in mitochondrial membrane permeability promote the transition of cytochrome c into the cytosol.[13] In the cytosol, cytochrome c activates apoptosis by interacting with the apoptotic protease activating factor 1.[14]

Relatively early, moonlighting proteins were noted to consist of ubiquitous proteins, such as metabolic enzymes.[15] The active sites of enzymes typically account for a small portion of the surface area, leaving most of the area for other purposes.[15] It was suggested that widely conserved proteins offer a basis for evolutionary diversification of functions.[16] But this suggestion does not entirely explain why metabolic enzymes, and other similar conserved proteins, are more likely to acquire moonlighting functions. One explanation could be that metabolic enzymes rarely experience constant levels of cofactors and substrates. For example, under physiological iron levels, the cytosolic aconitase binds an iron-sulfur cluster at the active site to catalyze the isomerization of citrate to isocitrate. When cellular iron levels drop, aconitase loses its iron-sulfur cluster, binds to iron-responsive elements in the mRNA of transferrin receptor mRNA, and reduces the degradation of transferrin receptor mRNA, thereby promoting iron uptake.[17–19] Based on these reports, it appears logical that metabolic enzymes are compelled to develop additional cellular functions given the constant changes in the metabolic state of cells.

1.2 Biological relevance of enzyme polymerization

In the previous chapter, I introduced how metabolic enzymes can change their subcellular localization and interaction partners. In this chapter, I will provide background information about the functional consequences of changes in the shape of enzymes. In the last 15 years, it has become increasingly evident that metabolic enzymes have functions beyond their catalytic activity. These 'non-catalytic' functions are quite common. A study in budding yeast revealed that one-third of enzymes with knockout phenotypes could be restored by versions of the enzymes that are catalytically inactive,[20] suggesting that these enzymes had essential non-catalytic functions. The field of non-catalytic enzyme functions gained great interest when a screen of enzymes labeled with fluorescent proteins identified that a common non-catalytic function of enzymes is the reorganization into clusters during nutrient starvation.[21] Subsequent screens have identified over 60 metabolic enzymes that form protein clusters in response to various cellular stressors,[21–24] but also under physiological conditions.[25] The finding that the clusters form dynamically and are reversible, suggests that these observations are not overexpression

artifacts. Enzymes can polymerize into large structures, such as filaments and rings. Enzyme polymers can also change their shape. For example, bacterial aldehyde alcohol dehydrogenase can form two distinct filaments: an inactive filament with compressed conformation and an active filament with extended conformation in the presence of cofactors.[26]

The functional consequences of enzyme polymerization are not entirely clear. However, we are beginning to understand several biological roles of enzyme polymerization (Figure 1). It has been suggested that enzyme polymerization controls metabolic flux to adapt to cellular needs.[27] Approximately 20 enzyme polymers have been described to control the flux of metabolic pathways.[28] Enzyme polymerization can stabilize and lock the inactive conformation of an enzyme. For example, the yeast glucokinase polymerizes into inactive filaments (Figure 2) to prevent excessive glycolysis during spikes in glucose levels.[29] Filamentation of glucokinase was found to be crucial for cellular fitness, as mutant yeast with non-polymerizing glucokinase had lower viability when challenged with spikes in glucose levels compared to yeast with wild-type glucokinase.[29] Inactive filaments and self-assemblies of enzymes have been suggested to store and protect enzymes from proteasomal degradation during nutrient starvation.[21,30] Therefore, the polymerization of enzymes could be a mechanism for rapid enzyme inhibition without requiring slow degradation processes. Perhaps more counterintuitively, enzyme polymerization can also increase enzyme activity. Over half of the identified filament-forming metabolic enzymes assemble in the active conformation.[28] Active enzyme filaments, such as human CTP synthase filaments, have been linked to increased metabolic demand.[31] Additionally, glycolytic enzymes have been shown to form cytosolic foci during hypoxia to increase glycolytic activity.[32] Therefore, the polymerization of enzymes could be a rapid mechanism to increase pathway flux without requiring slower transcription and translation processes.

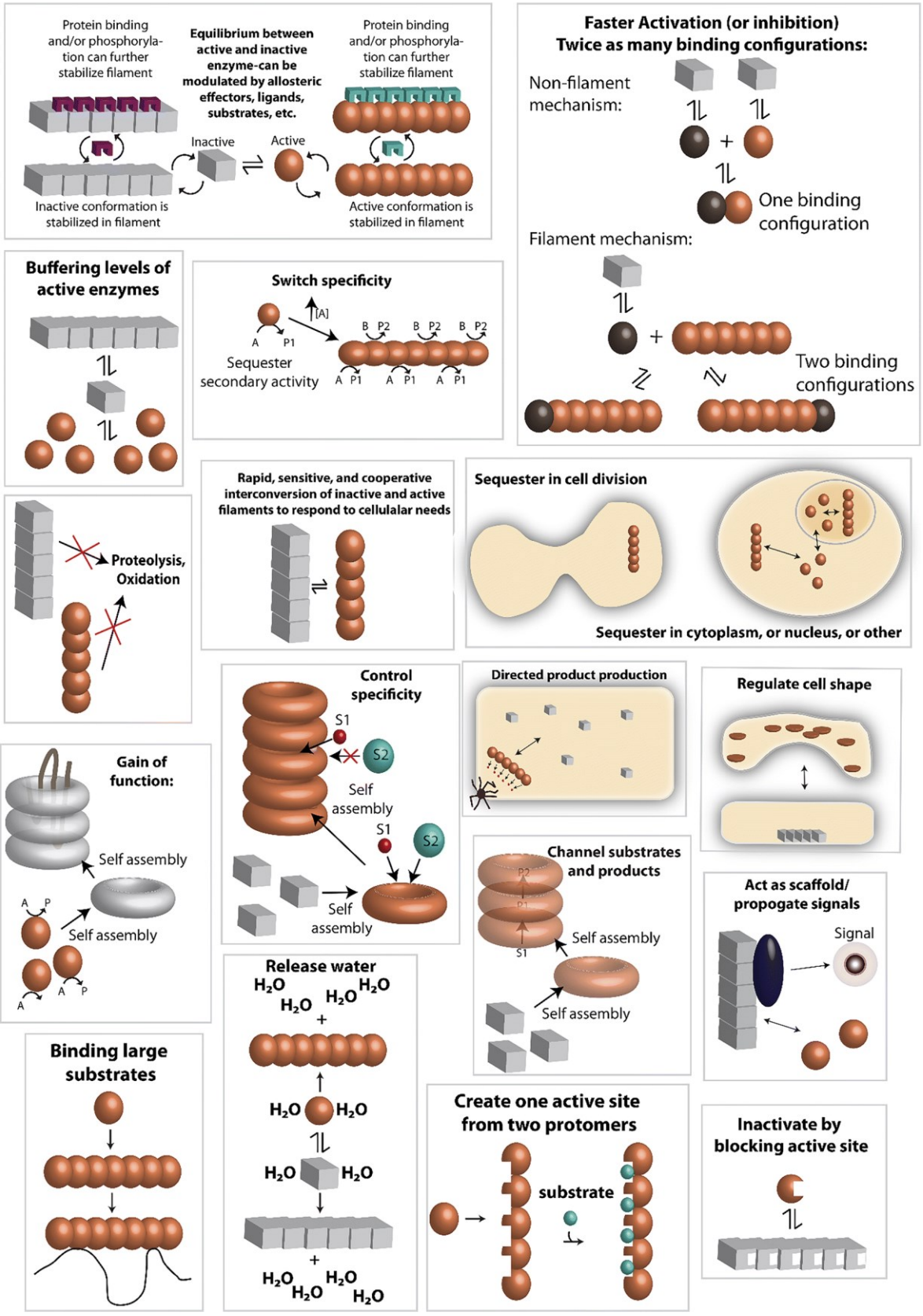

Figure 1. Biological roles of filament-forming enzymes. Grey squares, inactive enzyme; Copper spheres, active enzyme.[28] [Figure panels reproduced with permission from Park and Horton, 2019.]

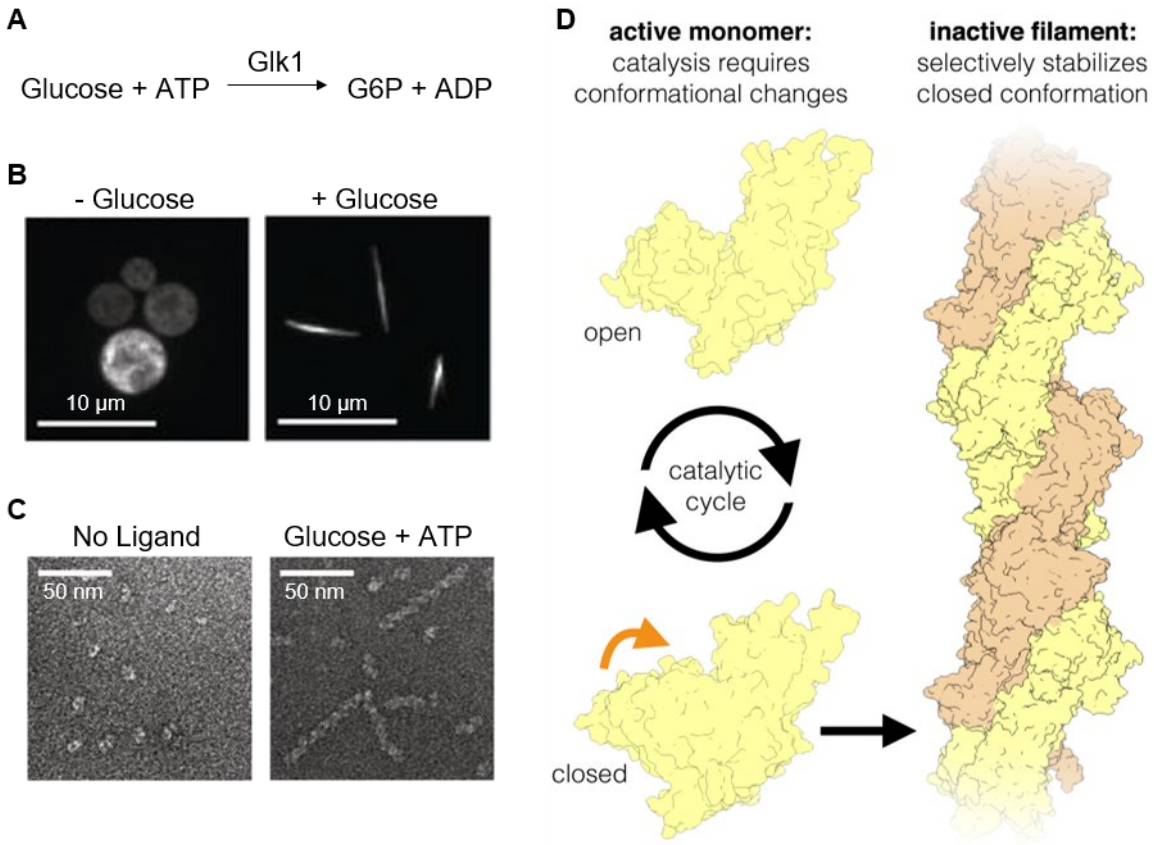

Figure 2. Yeast glucokinase (Glk1) forms inactive filaments. (**A**) Reaction catalyzed by Glk1. (**B**) Fluorescence images of stationary-phase Glk1-msfGFP before or after glucose addition.[29] (**C**) Electron micrographs of negatively stained Glk1 without ligands or saturating glucose and ATP.[29] (**D**) Glk1 forms two-stranded filaments that stabilize the closed conformation, inhibiting the enzyme activity.[27] [Figure 2B and 2C adapted with permission from Stoddard *et al*., 2020. Figure 2D reproduced with permission from Lynch, Kollman and Webb, 2020.]

However, control of metabolic flux is not the only function of enzyme polymerization. In 2019, Park and Horton made an excellent and comprehensive review of known cases of enzyme polymerization, their structural details, and potential functional roles in cellular processes.[28] A less frequent function of enzyme polymerization is the change in substrate specificity. For example, SgrAI, a sequence-specific endonuclease, cleaves 17 distinct DNA sequences when polymerized, whereas non-polymerized SgrAI only cleaves three DNA sequences.[33–35] Enzyme polymerization can also help cells regulate water availability by reducing enzyme surface area and, thus, the amount of water needed for enzyme hydration.[36] For example, adenylate kinase in plants is believed to form filaments during the night when the enzyme is not needed, to release water resources.[37] Enzyme polymerization has also been suggested to fulfill mechanical functions. For example, CTP Synthase in *Caulobacter crescentus* forms a filament

that regulates the curvature of the bacterium.[38] Interestingly, cytoskeletal proteins have been suggested to have evolved from enzymes that can form filaments.[39] Additionally, enzyme polymers have been proposed to act as scaffolds for binding partners.[28] Finally, there is the idea that enzyme polymers themselves could act as cellular sensors for different stressors.[28]

We are slowly beginning to understand the function consequences of enzyme polymerization. For example, enzyme polymerization has been linked to aging. In budding yeast, glutamate synthase polymerizes during aging, disrupting cellular amino acid homeostasis.[40] Inhibiting polymerization of glutamate synthase by mutating the polymerization interface restored amino acid levels in aged cells, and extended lifespan.[40] Given the diverse functions associated with enzyme polymerization, targeting enzyme polymerization could serve as an effective therapeutic approach for regulating cellular metabolism.

1.3 Exploring non-catalytic roles of mammalian hexokinase 1

Most studies on enzyme polymerization have focused on yeast and not mammalian enzymes (reviewed in Miura, 2022). It cannot be assumed that yeast and mammalian enzymes behave similarly, as differences in enzyme polymerization have been observed in different species. For example, CTP synthase forms different types of filaments in yeast, prokaryotes, and animals (Figure 3A-D).[42,43] Furthermore, CTP synthase filaments have different functions in different phyla (Figure 3E): Human CTP synthase filaments stabilize the active conformation, while prokaryotic CTP synthase filaments stabilize the inactive conformation.[31] Therefore, I think it is worthwhile to investigate enzyme polymerization in mammalian cells.

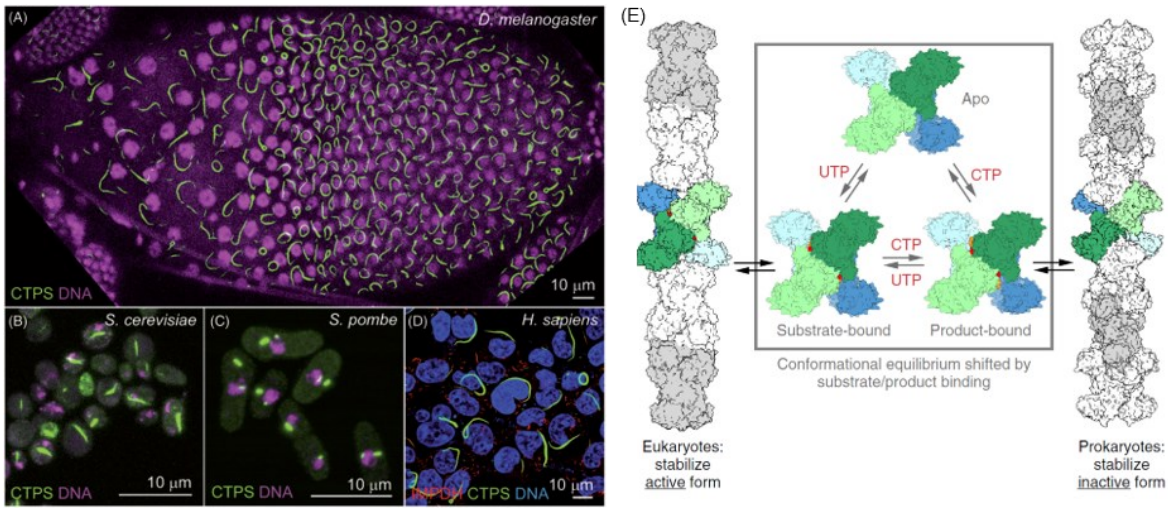

Figure 3. CTP synthase forms different filaments. (**A**) in fruit flies,[25] (**B**) budding yeast,[22] (**C**) fission yeast,[44] and (**D**) humans.[45,46] (**E**) CTP synthase filaments have different functions in humans and bacteria.[31] [Left figure panel reproduced with permission from Aughey and Liu, 2015. The right figure panel reproduced with permission from Lynch et al., 2017.]

Another understudied area in the field of enzyme polymerization is how the binding of enzymes to membranes affects enzyme polymerization. Theoretically, enzymes should polymerize faster on membranes than in solution [47]. I am aware of only one recent study studying the polymerization of the membrane-bound hydrogen-dependent CO_2 reductase (HDCR).[48] However, the functional consequences of the polymerization of membrane-bound HDCR were not discovered. It was suggested that membrane binding could stabilize HDCR polymers and facilitate the nucleation of new polymers.[48] Since the non-catalytic functions of membrane-bound mammalian enzymes are understudied, I focused my PhD project on the non-catalytic functions of mammalian hexokinase 1 (HK1), which is bound to the outer mitochondrial membrane.

There are other reasons why we focused on HK1. First, the ability to polymerize was described to be higher in enzymes that catalyze branch-point reactions of metabolic pathways.[24] For example, phosphofructokinase is one of the key enzymes controlling the flux of glycolysis,[49] and has been shown to form filaments.[50] Hexokinase catalyzes the ATP-dependent phosphorylation of glucose. The product of this reaction, glucose-6-phosphate (G6P), is a branch-point intermediate in three different metabolic pathways: glycolysis, pentose phosphate pathway, and glycogen synthesis. Second, many enzymes form filaments during nutrient starvation; therefore, I reasoned that investigating HK1 during glucose depletion would likely

uncover new non-catalytic enzyme functions. Also, glucose levels are easy to manipulate. Finally, the yeast glucokinase is evolutionarily related to HK1 and has been shown to form filaments.[29] Therefore, I reasoned that HK1 likely forms polymers during changes in substrate availability.

1.3.1 Properties of mammalian hexokinases

There are five isoenzymes of hexokinase found in mammalians (HK1, HK2, HK3, glucokinase, and hexokinase domain-containing 1), which differ in catalytic properties, subcellular location, and tissue distribution (Table 1).[51–54]

Table 1. Properties of mammalian hexokinases.

Isoform	K_m for glucose	Subcellular location	Tissue distribution
Hexokinase 1	30 µM	Outer mitochondrial membrane	All tissues, high expression in the brain
Hexokinase 2	300 µM	Outer mitochondrial membrane	muscle and adipose tissue
Hexokinase 3	3 µM	perinuclear	White blood cells
Glucokinase	8 mM	cytosol	Liver, pancreas
Hexokinase domain-containing 1	?	Outer mitochondrial membrane	All tissues

HK1 is found in all tissues and is highly expressed in brain tissues, where it acts as the pacemaker of glycolysis.[55] The recently discovered HKDC1, a product of HK1 gene duplication, is found in many tissues.[54,56] HK2 is abundant in insulin-responsive tissues such as muscle and adipose tissue. HK3 is weakly expressed in most tissues but highly expressed in white blood cells.[57] Glucokinase is found in the liver and pancreas, where it acts as a glucose sensor.[58] Within the cell, glucokinase is found in the cytosol, whereas HK3 has been reported to be located in the perinuclear region.[58,59] In contrast, HK1, HK2, and HKDC1 contain an N-terminal 21 amino acid long mitochondrial binding domain.[60,61]

1.3.2 Functional significance of hexokinase-mitochondria binding

Mitochondria are the primary source of ATP production in most eukaryotic cells. Mitochondrial localization is thought to provide mitochondrial HKs preferential access to mitochondrial ATP; in return mitochondrial HKs provide ADP for oxidative phosphorylation.[62] This hypothesis has been questioned as cytosolic ATP levels are well above the K_m for ATP of mitochondrial HKs.[63] However, mitochondrial HKs have been shown to link glycolysis to the mitochondrial ATP pool.[64] Several studies have shown that mitochondrial HKs have functions beyond mitochondrial bioenergetics. For example, HK1 and HK2 have been demonstrated to have antiapoptotic properties, possibly through interaction with voltage-dependent anion channel 1 (VDAC1), the main gate for cytochrome c release.[65–69] Dissociation of HK2 from mitochondria has been shown to promote apoptosis.[70,71] Interestingly, mitochondrial binding and glucose phosphorylation are required for the protective effects of HK1 and HK2.[63] In this study, overexpression of full-length HK1 or HK2 protected cells against cell death and decreased levels of reactive oxygen species.[63] Whereas glucose-binding mutated and truncated HKs, lacking the mitochondrial binding domain, only exerted partial effects.[63] Pointing to the importance of the mitochondrial location of HK1 in glycolysis regulation, it has been shown that truncated HK1 inhibits cytosolic GAPDH, thereby regulating the metabolic fate of glucose.[72] Dissociation of HK1 from mitochondria has been shown to reduce mitochondrial pyruvate flux.[73] Dissociation of HK1 from mitochondria in endothelial cells has been also linked to heart failure.[74] In conclusion, the significance of hexokinase-mitochondria binding goes beyond bioenergetics, influencing diverse cellular functions. The next chapter explores additional non-catalytic functions of mitochondrial hexokinases, unravelling their impact on cellular physiology.

1.3.3 Other non-catalytic functions of mitochondrial hexokinases

Multiple hexokinase isoforms exist within the same cell, suggesting functions beyond basic catalysis. Indeed, numerous non-catalytic functions are known for mitochondrial HKs, as comprehensively reviewed in Rodríguez-Saavedra *et al*., 2021.[75] Among the HK isoforms, HK2 has been studied the most, primarily because

of its role in the development of cancer.[76] Consequently, additional functions of HK2 have been identified. For example, HK2 was found to locate to mitochondria endoplasmic reticulum contact sites (MERCs) in neoplastic cells.[77] The displacement of HK2 from MERCs led to Ca^{2+} overload-induced cell death.[77] A recent study confirmed that the dissociation of HK2 from mitochondria leads to a release of ER Ca^{2+}.[78] Moreover, HK2 has been shown to localize to the nucleus in haemopoietic stem cells to maintain stemness.[79] Furthermore, HK2 has been shown to translocate to the cytosol during glucose depletion, possibly to regulate glycogen formation.[80] Additionally, one study found that bacterial peptidoglycan can inhibit HK2 activity and trigger the dissociation of HK2 from mitochondria.[81] In the cytosol, HK2 activates NOD-like receptor pyrin domain-containing 3 (NLRP3) inflammasome, thus acting as a sensor for bacterial peptidoglycan.[81] A subsequent study from the same group has shown that HK2 dissociation from mitochondria is a common feature of NLRP3-inflammasome activation.[78]

The non-catalytic functions of HK1 are much less studied. One study reported that HK1 can phosphorylate histone 2A in the absence of glucose.[82] However, the physiological relevance of this finding remains unclear. HK1 has also been shown to be involved in the cellular response to DNA damage: DNA damage leads to cytosolic relocalization and inactivation of HK1 to prevent glycolysis.[83]

1.3.4 The role of mitochondrial hexokinases in diseases

As HK1 is highly expressed in the brain and the retina, it is not surprising that several studies link mutations in HK1 to neurological diseases, and retinitis pigmentosa.[84–88] Mitochondrial HKs are overexpressed in many types of cancers, characterized by rapid cell proliferation and a glycolytic phenotype.[89–91] In cancer cells, overexpression of mitochondrial HKs has been linked to high rates of glucose fermentation to lactate even under the presence of oxygen, known as aerobic glycolysis or the Warburg effect.[76,92] Otto Warburg hypothesized that aerobic glycolysis stems from defects in mitochondrial respiration.[93,94] However, non-cancerous cells with healthy mitochondria are able to perform aerobic glycolysis to promote cell proliferation.[95–97] Mathematical models have shown that aerobic glycolysis aims to meet cellular energy demands, which mitochondrial oxidative phosphorylation cannot satisfy, during fast proliferation.[98]

High glycolytic flux, a characteristic of the Warburg effect, limits the import of pyruvate into mitochondria, leading to elevated production and secretion of lactate, which is believed to promote tumorigenesis.[99,100] Thus, strategies to target and inhibit the catalytic activity of mitochondrial HKs have been of major interest in cancer therapy.[101,102] Two of the most studied HK inhibitors are 2-deoxyglucose (2-DG) and 3-bromopyruvate (3BP). 2-DG competes with glucose for binding at HKs. In contrast to glucose-6-phosphate, phosphorylated 2-DG cannot be metabolized further, thereby blocking glycolysis and depleting cellular ATP levels.[103,104] Although 2-DG has shown promising results in preclinical studies, the hypoglycemia-like side effects of 2-DG in clinical studies have been concerning.[105,106] 3BP, a pyruvate analog, is one of the most potent antiglycolytic drugs under investigation. 3BP has been shown to dissociate HK2 from mitochondria; however, the exact mechanism is not fully understood.[107,108] Moreover, it has been suggested that 3BP inhibits glycolysis mainly by alkalizing the active site of glyceraldehyde-3-phosphate dehydrogenase (GAPDH), with only minor effects on the activity of HK2.[109] Similar to 2-DG, monotherapy with 3BP has shown limited antitumor effects.[110] Therefore, combination treatments need to be found for more promising cancer therapies.

1.4 Significance of HK-VDAC1 interaction in cellular processes

Mitochondrial HKs have been shown to interact with the voltage-dependent anion channel 1 (VDAC1), the main transporter in the outer mitochondrial membrane (OMM), regulating metabolic and energy homeostasis.[111–113] VDAC1 has been reported to control mitochondrial apoptotic pathways via interaction with various proteins.[114–116] The interaction of VDAC1 with pro- or antiapoptotic proteins can affect the permeability of the OMM and promote or inhibit cell death.[117–122] The cell protective interaction between mitochondrial HKs and VDAC1 has been well described. For example, it has been reported that overexpression of VDAC1 can promote cell death, which is mitigated by co-overexpression of HK2.[123]

Due to the significance of the HK-VDAC1 interaction in promoting cell growth and survival, disrupting HK-VDAC1 interaction has been recognized as a potentially viable therapeutic approach for impeding the proliferation of rapidly growing cancer cells.[124–128] Although certain VDAC1 residues crucial for binding with HK1 and HK2 have been recognized, structural details remain poorly understood.[65,66,124,129–131]

Two protein-protein docking studies proposed the direct insertion of the mitochondrial binding domains from HK1 or HK2 into the pore of VDAC1.[132,133] However, a recent study critiqued several crucial aspects of the previous HK-VDAC1 interaction models.[134] For example, it was unclear why HK1 binding does not completely block the maximal conductance of VDAC1, since the proposed plugged model would suggest blockage of the entire channel.[65,117,124,129] Moreover, at the docking interface, the hydrophobic mitochondrial binding domain of HK1 or HK2 does not align well with the highly charged inner surface of VDAC1.[134,135]

It has been suggested that VDAC1 enhances the binding of HKs to the OMM.[136] Nevertheless, mitochondrial HKs are capable of binding to the OMM even when VDAC1 is not present.[123,137] Truncation of the mitochondrial binding domains of mitochondrial HKs hinders HK binding to the OMM, even when VDAC1 is present.[63,138] Furthermore, super-resolution imaging of FLAG-tagged VDAC1 and immunolabeled HK1 suggested that VDAC1 clusters on the OMM, whereas HK1 is more homogenously distributed on the OMM.[139] It has been hypothesized that mitochondrial HKs insert first into the OMM and the membrane-bound HKs from a complex with VDAC1.[134] Using molecular dynamics and Brownian dynamics simulations, it has been shown that HK2 partially blocks the conductance of VDAC1 and that phosphorylation of VDAC1 can disrupt the HK2-VDAC1 interaction.[134] These findings can be expanded to HK1-VDAC1 interaction as HK1 and HK2 have high sequence and structural homology.

1.5 Live-cell Imaging of Enzymes and Mitochondria: Fluorescence Microscopy Techniques and Biosensors

Live-cell imaging has revolutionized our view of metabolic enzymes by allowing the direct observation of protein-protein interactions and compartmentalization of metabolism within cells. In addition, live-cell imaging has greatly impacted our view on the moonlighting functions of metabolic enzymes by allowing us to monitor metabolic activities in real-time using genetically encoded reporters, as comprehensively reviewed in Depaoli et al., 2019 and Chandris, Giannouli and Panayotou, 2021.[140,141] This technology has provided insights into the spatiotemporal orchestration of complex biochemical processes, such as monitoring cellular energy status, ion concentration, and metabolite levels.

The isolation of green fluorescent protein (GFP) in the early 1960s was a major breakthrough in cell biology.[142,143] Three decades later, GFP became a key tool in molecular biology after successful cloning and expression.[144–146] Evolving the fluorescent properties of GFP led to a broad palette of colored fluorescent proteins.[147,148] Genetically encoded fluorescent probes allow to visualize a wide range of cellular processes, such as gene expression, protein movement, interactions, trafficking, and organelle dynamics.[149–152] By incorporating localization sequences, the probes can be directed to various subcellular compartments, enabling the study of localized cellular events.[153,154] In parallel, genetically encoded reporters were developed, which typically include one or two fluorescent proteins connected to specific domains that can bind to an analyte or undergo chemical modifications through signaling processes. This interaction influences the spectral properties of the fluorescent proteins, offering a measurable readout for different cell signaling events and metabolic processes.[155–158] Single FP-based reporters, though intensiometric, are advantageous for multispectral imaging.[159] Förster resonance energy transfer (FRET)-based reporters inherently offer a ratiometric readout, which allows for accurate analyte quantification since changes in FRET ratios are not affected by expression levels.[160] The versatility of genetically encoded reporters can be enhanced by modifying FPs or sensor domains, creating multicolored sensor variants for simultaneous measurements of multiple parameters.[140,159,161,162] By visualizing the metabolic activity of cells, live-cell imaging has enabled a better understanding of their function and regulation, which is essential for studying metabolism in health and disease.[163–165] The capability to observe metabolic processes at the single-cell level has also enabled the creation of new tools for high-throughput screening and for identifying compounds that influence cellular metabolic activities.[166]

Live-cell imaging has furthered our knowledge of mitochondria by enabling the observation of mitochondrial movement, fission, and fusion. These processes are crucial for maintaining proper mitochondrial function and overall cellular health, as comprehensively reviewed in Glancy, 2020.[167] Although biochemical methods and protein analyses can help to evaluate mitochondrial function,[168–170] microscopic observations can be used to assess mitochondrial function in intact cells. There are three main ways to visualize mitochondria for fluorescence microscopy: First,

mitochondria can be quickly stained with fluorescent dyes; however, results should be interpreted with caution due to the potential toxicity of the dyes.[171] Second, mitochondria can be visualized in fixed cells with immunofluorescence using mitochondria-specific antibodies. However, the downside of this approach is the non-specific antibody labeling and the potential introduction of artifacts due to cellular fixation.[172] Last, mitochondria can be observed using genetically encoded fluorescent proteins that are directed to specific proteins or mitochondrial compartments. providing stable and specific labeling of mitochondrial structures.[153] Because the small internal components and distances within mitochondria are very small, electron microscopy is commonly used for visualizing mitochondrial ultrastructure. However, with advancements in microscopy techniques, such as high- and super-resolution microscopy, it is now possible to visualize mitochondrial ultrastructure in living cells. For example, a fast and gently super-resolution microscopy approach (structured illumination microscopy; SIM), showed that cristae are unevenly distributed in mitochondria, and areas of decreased cristae density correspond to locations where mitochondrial fission occurred.[173] The same technology was recently used to visualize mitochondrial cristae dynamics and the redistribution of components of the mitochondrial Ca^{2+} uptake machinery.[174,175] Obtaining these findings through electron microscopy is challenging because of its static nature. Although live-cell imaging of mitochondria can be challenging due to phototoxicity, progress in developing faster and gentler microscopy methods, and improvements in more stable fluorophores are enhance our ability to observe how mitochondria function in cells.

1.6 Challenges of visualizing VDAC1

The large size of FPs has been reported to interfere with the targeting and functions of the tagged proteins.[176] This issue has been observed in the case of GFP-tagged VDAC1.[177,178] The precise incorporation of VDAC1 into the outer mitochondrial membrane depends on the tags' specific position, charge, and length.[179] Research indicates that longer tags can cause VDAC1 misplacement,[177–179] likely because the tag masks the recognition of the targeting signal.[180] Therefore, we reasoned that tagging VDAC1 with a short tag will not interfere with the localization and function of VDAC1.

1.6.1 The tetracysteine-tag is a promising alternative

A widely used and relatively small tag in molecular biology is the small fragment of the self-complementing split-FP approach.[181] Unfortunately, with a size of 16 residues for the small fragment, we anticipate that the split FP approach will not be suitable for tagging VDAC1. The tetracysteine (TC)-tag, which has only six residues (CCPGCC), has been shown to be valuable alternative to conventional FP imaging.[182] The TC-tag can be visualized by fluorogenic dyes, such as FlAsH-EDT_2 or the red-shifted ReAsH-EDT_2.[183] Therefore, we believe that TC-tagging is a promising approach to visualize VDAC1.

1.7 Aims and hypotheses

The subcellular localization of mitochondrial HKs is highly relevant for their canonical function in glucose phosphorylation and their non-canonical functions, such as influencing VDAC1-dependent apoptosis. We propose that observing mitochondrial HKs in living cells is crucial to understand how HK1 transitions between different functions. Thus, the main goal of my PhD is to visualize and track the dynamics of mitochondrial HKs, in relation to other outer mitochondrial membrane proteins, including VDAC1, using advanced high-resolution imaging techniques. We will focus on developing new protocols to capture changes in the distribution of mitochondrial HKs, particularly HK1, in response to different cellular stressors. Additionally, we will investigate whether these changes are specific to cancer cells, or if cancer cells exhibit a unique dynamic profile in this context.

Aims

- To explore and characterize the non-catalytic functions of HK1.
- To investigate the live-cell dynamics of HK1 and understand its organization during fluctuations in glucose availability.
- To assess whether the TC-tag affects the subcellular location of VDAC1.
- Identify treatments that affect the binding of HKs to mitochondria.

Hypotheses:

- We hypothesize that HK1 has non-catalytic functions that are crucial in cellular processes.
- We predict that HK1 undergoes structural reorganization during glucose depletion.
- With its shorter length and specific characteristics, we hypothesize that the TC-tag will allow for the precise visualization of VDAC1 in live cells, overcoming the complications associated with larger fluorescent protein tags.
- We predict that combination treatments will disrupt the binding of HKs to mitochondria.

2 Materials and Methods

Material and methods are published in Pilic *et al*., 2024[184] and *Pilic et al*., 2023[185].

2.1 Cell culture

HeLa S3, SH-SY5Y, MCF7, and MEF cells were cultured in Dulbecco's modified Eagle's medium (DMEM D5523, Sigma-Aldrich), which was supplemented with 10% fetal calf serum (FCS), 10 mM $NaHCO_3$, 50 U/mL penicillin-streptomycin, 1.25 µg/mL amphotericin B, and 25 mM HEPES, with the pH adjusted to 7.45 using NaOH. U2OS Fis1-GFP cells received an additional 15 mM glucose. INS-1 cells were grown in GIBCO RPMI medium 1640, supplemented with 10% FCS, 10 mM HEPES, 2 mM L-glutamine, 1 mM sodium pyruvate, 0.05 mM beta-mercaptoethanol, 50 U/mL penicillin-streptomycin, and 1.25 µg/mL amphotericin B. All cells were incubated in a humidified incubator with 5% CO_2 at 37°C.

2.2 Transfection

Cells were seeded in 6-well plates on 30 mm glass coverslips (Paul Marienfeld GmbH & Co. KG, Lauda-Königshofen, Germany) and transfected using PolyJet (SignaGen Laboratories) following the manufacturer's instructions. Briefly, 3 µl of PolyJet reagent was combined with 1 µg of plasmid DNA in 100 µl of DMEM, free of serum and antibiotics, for each well. The transfection mixture was added to 1 ml of culture medium and incubated for 8 hours, after which it was replaced with 2 ml of fresh culture medium. Imaging was performed 24 to 48 hours post-transfection.

2.3 Imaging of subcellular protein dynamics

Prior to imaging, cells were transferred to a storage buffer composed of 135 mM NaCl, 5 mM KCl, 2 mM $CaCl_2$, 1 mM $MgCl_2$, 10 mM HEPES, 2.6 mM $NaHCO_3$, 0.44 mM KH_2PO_4, 0.34 mM Na_2HPO_4, 10 mM D-glucose, 2 mM L-glutamine, 1X MEM amino acids, 1X MEM vitamins, 1% penicillin-streptomycin, and 1% amphotericin B, with the pH adjusted to 7.45 using NaOH.

High-resolution imaging was conducted using a confocal laser scanning microscope (Axiovert 200 M, Zeiss) equipped with a 100×/1.45 NA oil immersion

objective (Plan-Fluor, Zeiss) and a Nipkow-based confocal scanner unit (CSU-X1, Yokogawa Electric Corporation). Diode lasers (Visitron Systems, Pucheim, Germany) provided the excitation light, with BFP, CFP, YFP, GFP, and RFP fusion constructs being excited by 405, 445, 488, and 561 nm lasers, respectively. Emission was detected by a CoolSNAP HQ2 CCD Camera (Photometrics Tucson, Arizona, USA) using specific filters for each fluorophore (ET445/58m, ET460/50m, ET525/36m, ET535/30m, and ET630/75m by Chroma Technology Corporation). FlAsH was excited in a manner similar to GFP for two-color imaging and like YFP for three-color imaging.

Super-resolution imaging was performed with a structured illumination microscope (Nikon) fitted with a 100×/1.49 NA oil immersion objective (CFI Apochromat TIRF, Nikon), standard filter sets, and two iXon EMCCD cameras (Andor). GFP and RFP fusion constructs were excited with 488 and 561 nm lasers, respectively.

2.4 Image analysis

Image analysis was conducted using Fiji software. Z-stack images, captured with a step size of 200 nm, were processed with deconvolution and background subtraction using a rolling ball radius of 50 to 300 pixels. For colocalization analysis, the TrackMate plugin was employed to detect and quantify colocalization between protein clusters, and the ImageJ plugin Coloc2 was used to calculate the Pearson and Manders' coefficients. 3D images of a luminal ER marker were thresholded to assess ER morphology using the Sauvola local threshold and Li global threshold. ER morphology parameters were evaluated with the ImageJ plugin 3D Manger. The width of mitochondria was determined using the full width at half maximum. To evaluate mitochondrial morphology, 2D images of a mitochondrial matrix marker were thresholded with the Otsu method. The Aspect Ratio was calculated as the ratio of the longest to the shortest axes of the mitochondrial matrix marker. The Form Factor was determined using the following formula:

$$Form\ Factor = \frac{Perimeter^2}{4\pi \times \mathrm{Area}}$$

2.5 Single-cell ATP and glucose imaging

ATP and glucose FRET imaging was performed using an inverted microscope (IX73 system, Vienna, Austria) equipped with a 40×/1.4 NA oil immersion objective (UPLXAPO40XO, Olympus) and an optical beam splitter (Photometrics DV2, Photometrics, Tucson, AZ, USA). HeLa cells expressing either the mitochondria-targeted mtAT1.03 or the cytosolic FLII12Pglu-700uDelta6 CFP-YFP-based biosensors were imaged. CFP excitation in the FRET pair was achieved with an LED-based light source (LEDHub, Omicron) and a 427/10 Brightline HC excitation filter (Semrock). Emission light was detected using a Retiga R1 CCD camera (Teledyne QImaging) with a CFP/YFP/mCherry triple LED HC emission filter (Semrock).

2.6 Mitochondrial membrane potential measurements

Cells were stained with 25 nM tetramethylrhodamine methyl ester (TMRM; Molecular Probes, Invitrogen) for 15 minutes at 37°C prior to measuring membrane potential with a Nikon Eclipse Ti2 microscope. This microscope was fitted with a 40×/1.15 NA water immersion objective (CFI Apochromat, Nikon), standard filter sets, and two Kinetix Scientific CMOS cameras (Photometrics). Excitation of TMRM was achieved with 580 nm light from pE-800 (CoolLED). For each iteration, 6x6 images were stitched, background subtracted, and subjected to thresholding using the Triangle method before quantifying TMRM intensity.

2.7 Perfusion of cells during live cell imaging

Transfected cells on 30 mm coverslips were positioned in a PC30 perfusion chamber (NGFI, Graz, Austria) and perfused at a flow rate of approximately 1 ml per minute using a gravity-based perfusion system (PS9, NGFI). The glucose-containing buffer included 135 mM NaCl, 5 mM KCl, 2 mM CaCl2, 1 mM MgCl2, 10 mM HEPES, and 10 mM D-glucose, with the pH adjusted to 7.45 using NaOH. The glucose-free buffer was prepared by substituting glucose with 10 mM D-mannitol.

2.8 Cell permeabilization

Cells were perfused with 10 µM digitonin for 4 minutes using a buffer designed to mimic intracellular ion composition. This buffer contained 10 mM NaCl, 110 mM KCl, 1 mM MgCl2, 0.1 mM EGTA, 10 mM HEPES, and 10 mM D-glucose, with the pH adjusted to 7.4 using NaOH. For glucose-free conditions, the buffer substituted glucose with 10 mM D-mannitol. In dose-response experiments, increasing concentrations of ATP or glucose-6-phosphate (G6P) were added to the glucose-free intracellular buffer, and the percentage of cells displaying HK1-clusters was assessed. Additionally, for phosphate addition experiments, 100 µM G6P was mixed with phosphate-buffered saline (PBS).

2.9 Immunofluorescence

Wild-type HeLa cells, HeLa cells transfected with VDAC1-TC, and MCF7 cells were cultured in 6-well plates on 30 mm coverslips until reaching approximately 80% confluency. HeLa cells were used to analyze endogenous VDAC1, while MCF7 cells were used to examine endogenous HK1. The cells were then taken from the incubator and incubated in a storage buffer containing 1 µM MitoTracker Red CMXRos for HeLa cells or 1 µM FlAsH for MCF7 cells for 15 minutes at 37°C. HeLa cells were washed with 100 µM BAL, whereas MCF7 cells were perfused with glucose-free buffer for 30 minutes to induce HK1 clustering. Control MCF7 cells were perfused with glucose buffer. Following this, all cells were washed twice with PBS and fixed with 4% paraformaldehyde at room temperature for 15 minutes. After fixation, the cells were washed three times with PBS and blocked with 5% BSA in PBS for one hour with gentle shaking. The blocking buffer was then replaced with a 1:1000 dilution of VDAC1 mouse monoclonal antibody (abcam, #14734) or a 1:1000 dilution of HK1 rabbit monoclonal antibody (Cell Signaling, #2024) in PBS with 5% BSA. The cells were incubated with the primary antibody overnight at 4°C with gentle shaking. The following day, the primary antibody solution was removed, and the cells were washed three times with PBS. Secondary antibodies, Alexa Fluor 568 goat anti-mouse or Alexa Fluor 488 goat anti-rabbit (Thermo Fisher Scientific) at a 1:2500 dilution, were then applied. The cells were incubated in the dark for 2 hours at room temperature with gentle shaking. Finally, the cells were washed three times

with PBS for 5 minutes, mounted using Vectashield antifade mounting medium (Vectorlabs), and the coverslips were sealed with nail polish.

2.10 Protein extraction and Immunoblot

To evaluate VDAC1 protein levels, cells were plated in 6-well plates and transfected with 0.5 µg of plasmid DNA. After 48 hours, the cells were harvested using RIPA buffer (25 mM Tris-HCl, 150 mM NaCl, 5 mM EDTA, 1% Triton X-100, 1% sodium deoxycholate, 0.1% SDS; pH adjusted to 7.60 with NaOH) containing a protease inhibitor cocktail (Sigma). Protein concentration was measured using the BCA Assay (ThermoFisher Scientific) with a CLARIOstar Plus (BMG Labtech). For each condition, 30 µg of protein were separated on a 12.5% SDS-polyacrylamide gel and transferred to a PVDF membrane (Merck Millipore). The membrane was blocked with 5% milk powder (Merck Millipore) in TBS-Tween (20 mM Tris, 0.14 M NaCl, 0.1% Tween-20, pH 7.6) for 1 hour at room temperature. The membrane was then cut and incubated overnight at 4 °C with gentle shaking in a blocking solution containing either a 1:5000 dilution of monoclonal mouse VDAC1 antibody (abcam, #186321) or a 1:1000 dilution of monoclonal mouse β-actin antibody (Sigma, A5316). Following incubation, the membranes were washed three times for 5 minutes with 0.1% TBS-Tween buffer and then incubated with a 1:3000 dilution of HRP-conjugated secondary anti-mouse antibody for 1 hour at room temperature. After washing, the membranes were exposed to a chemiluminescent reagent (ThermoFisher Scientific), and the resulting signal was detected using the ChemiDoc MP Imaging System (Biorad). The relative optical density was analyzed using Fiji software.

2.11 Seahorse measurements

Cells were plated onto XF96 polystyrene cell culture microplates (Agilent, Seahorse) and grown until they reached 100% confluency. Prior to measurement, the cells were washed and transferred to XF assay medium supplemented with 1 mM sodium pyruvate, 2 mM glutamine, and 5.5 mM D-glucose. The XF96 extracellular flux analyzer (Agilent, Seahorse) was then used to measure the ratio of oxygen consumption rate (OCR, pmol O_2/min) to extracellular acidification rate (ECAR, mpH/min).

2.12 Chemicals

To label the inner mitochondrial membrane, cells were incubated with 200 nM MitoTracker Red CMXRos (Thermofisher) in a storage buffer for 10 minutes at 37°C, followed by washing with the same buffer. Actin polymerization was inhibited by exposing the cells to 10 µM cytochalasin D (Sigma) in a glucose buffer. Mitochondrial fission was induced by treating the cells with either 2 µM FCCP (Sigma) or 4 µM ionomycin (Abcam) for 10 minutes in the glucose buffer. Apoptosis was triggered by treating the cells with 10 µM staurosporine (Sigma) for one hour in the storage buffer. ER stress was induced by incubating the cells with 1 µM tunicamycin (Sigma) for two hours in the storage buffer. Additionally, mitochondrial DNA was stained with 1 µM STYO13 (Molecular Probes) for 15 minutes.

2.13 Generation of 3D structures of VDAC1-fusion constructs

The 3D structures of GFP-VDAC1, VDAC1-GFP, and VDAC1-TC were generated using ColabFold v1.5.2-patch, a modified version of AlphaFold2 that utilizes MMseqs2 for sequence alignment and structural prediction. The 3D structures were visualized with UCSF Chimera.

2.14 NMR metabolomic profiling

Nuclear Magnetic Resonance (NMR) sample preparation and analysis were performed as described previously.[186] Briefly, cell pellets were combined with 600 µl of methanol (in a 2:1 ratio), while 200 µl of cell supernatants were mixed with 400 µl of methanol. The samples were then lysed using a Precellys homogenizer and stored at -20 °C for one hour before further processing. Next, the samples were centrifuged at 10,000 rpm and 4 °C for 30 minutes. The supernatants were lyophilized, and 500 µl of NMR buffer (containing 0.08 M Na_2HPO_4, 5 mM 3-trimethylsilyl propionic acid-2,2,3,3,-d4 sodium salt (TSP), and 0.04% NaN3 in D2O, adjusted to pH 7.4 with 8 M HCl and 5 M NaOH) were added to the samples, which were then placed into 5 mm NMR tubes. All NMR measurements were performed at 310 K using an AVANCE™ Neo Bruker Ultrashield 600 MHz spectrometer with a TXI probe head, and the data were processed as previously described.[187] For the ^1H 1D NMR experiments, the 1D CPMG (Carr-Purcell-Meiboom-Gill) pulse

sequence (cpmgpr1d) was used with the following parameters: 512 scans, 73,728 points in F1, a spectral width of 11,904.76 Hz, 512 transients, and a recycle delay of 4 seconds. Water suppression was achieved through pre-saturation. The spectra were acquired and automatically processed using Bruker Topspin 4.0.2 software, which included exponential line broadening of 0.3 Hz, phasing, and referencing to TSP at 0.0 ppm. The processed spectra were then imported into Matlab2014b, where regions corresponding to water, TSP, and residual methanol signals were removed. Data analysis and figure generation were performed with MetaboAnalyst 5.0.

2.15 Plasmids

Table 2. Plasmids used for transfection during my PhD studies.

Name	Description	Source
HK1-GFP	HK1 marker	[63] Addgene #21917
HK1-mRuby3	HK1 marker	[188]
HK1-ATPmut-GFP	ATP binding mutant G862A.[189]	[184]
Monomeric-HK1-GFP	E280A, R283A, G284Y mutations prevent dimerization of HK1.[190]	[184]
HKDC1-GFP	Hexokinase domain containing 1	[184]
HK2-GFP	HK2 marker	[63] Addgene #21920
HK1N-HK2C-GFP	The N-terminal half of HK1 fused to C-terminal half of HK2	[184]
HK2N-HK1C-GFP	N-terminal half of HK2 fused to C-terminal half of HK1	[184]
Truncated-HK1-GFP	Lacks mitochondrial binding domain (MBD)	[63] Addgene #21918
HK1MBD-GFP	Mitochondrial binding domain of HK1	[184]
HK2MBD-HK1-GFP	Mitochondrial binding domain of HK1 was replaced by MBD of HK2	[184]
HK1-L6A-GFP	Mutation in the MBD	[184]
HK1-L7A-GFP	Mutation in the MBD	[184]
HK1-F11A-GFP	Mutation in the MBD	[184]
HK1-L14A-GFP	Mutation in the MBD	[184]
mitoDsRed	Mitochondrial matrix marker	Addgene #44386
mito-sfGFP	Mitochondrial matrix marker	[191]
mitoBFP	Mitochondrial matrix marker	Addgene #49151
ComplexIV8-mRuby2	Cristae membrane marker	[192]

MICU1-CFP	MICU1 marker	[175]
BFP-KDEL	ER lumen marker	Addgene #49150
mCh-ER3	Luminal ER marker	Addgene #55041
mCh-Sec61β	Membrane ER marker	Addgene #49155
GFP-BAK	BAK marker	Addgene #32564
mCherry-Actin	Actin marker	Addgene #54957
tagRFP-Tubulin	Tubulin marker	Evrogen #FP145
mCherry-Parkin	Parkin marker	Addgene #23956
mCherry-Drp1	Drp1 marker	Addgene #49152
mCh-Fis1	Fis1 anchor	Addgene #182580
mCh-Mff	Mff marker	Addgene #157760
mCh-MiD51	MiD51 marker	[193]
FLII12Pglu-700uDelta6	Cytosolic FRET-based glucose sensor.[194]	Addgene #17866
GFP-VDAC1	GFP fused to the N-terminus of VDAC1	Addgene #211735
VDAC1-VDAC1	GFP fused to the C-terminus of VDAC1	Addgene #211734
VDAC1-TC	TC-tag fused to the C-terminus of VDAC1	Addgene #211733

3 Results

3.1 HK1 forms rings during energy stress

To explore the non-catalytic functions of HK1 and its dynamic behavior during glucose fluctuations, we visualized HeLa cells that coexpressed HK1-GFP with mitoDsRed, a mitochondrial matrix marker. In the presence of glucose, HK1 was found to be uniformly distributed around the mitochondria (Figure 4A, left images)[184]. Removal of glucose lead to the formation of HK1-clusters on mitochondria (Figure 4A, right images)[184]. During glucose depletion, these HK1-clusters became more prominent (Figure 4B)[184] and ultimately formed rings around mitochondria (Figure 4C)[184]. HK1-clusters slightly deformed mitochondria (Figure 4D)[184], whereas HK1-rings completely encircled mitochondria (Figure 4E)[184]. These structures disassembled within two minutes of glucose readdition, indicating that the clustering is a dynamic, regulated response rather than an artifact of GFP overexpression.

To rule the possibility that the formation of HK1-rings is an overexpression artifact of GFP,[195] we conducted immunofluorescence analysis. Glucose deprivation led to the formation of endogenous HK1-clusters in MCF-7 cells. (Figure 4F)[184]. HK1 was weakly expressed in HeLa cells and was not located at mitochondria (Figure 4G). Next, we assessed HK1-clustering in different cells. Approximately 90% of HeLa cells expressing HK1-GFP formed HK1-clusters after 20 min of glucose deprivation (Figure 4H)[184]. Similar results were observed in SH-SY5Y neuroblastoma cells and in mouse embryonic fibroblasts (Figure 4H)[184]. In contrast, less than 10% of rat insulinoma cells (INS-1) formed HK1-clusters following 20 min of glucose deprivation (Figure 4H)[184]. Given that INS-1 cells are able to sustain ATP levels for extended periods of glucose deprivation,[64] we reasoned that the formation of HK1-clusters results from ATP deficiency rather than glucose deficiency. We explored the formation of HK1-clusters more directly with genetically encoded biosensors for mitochondrial ATP and cytosolic glucose levels.[194,196]

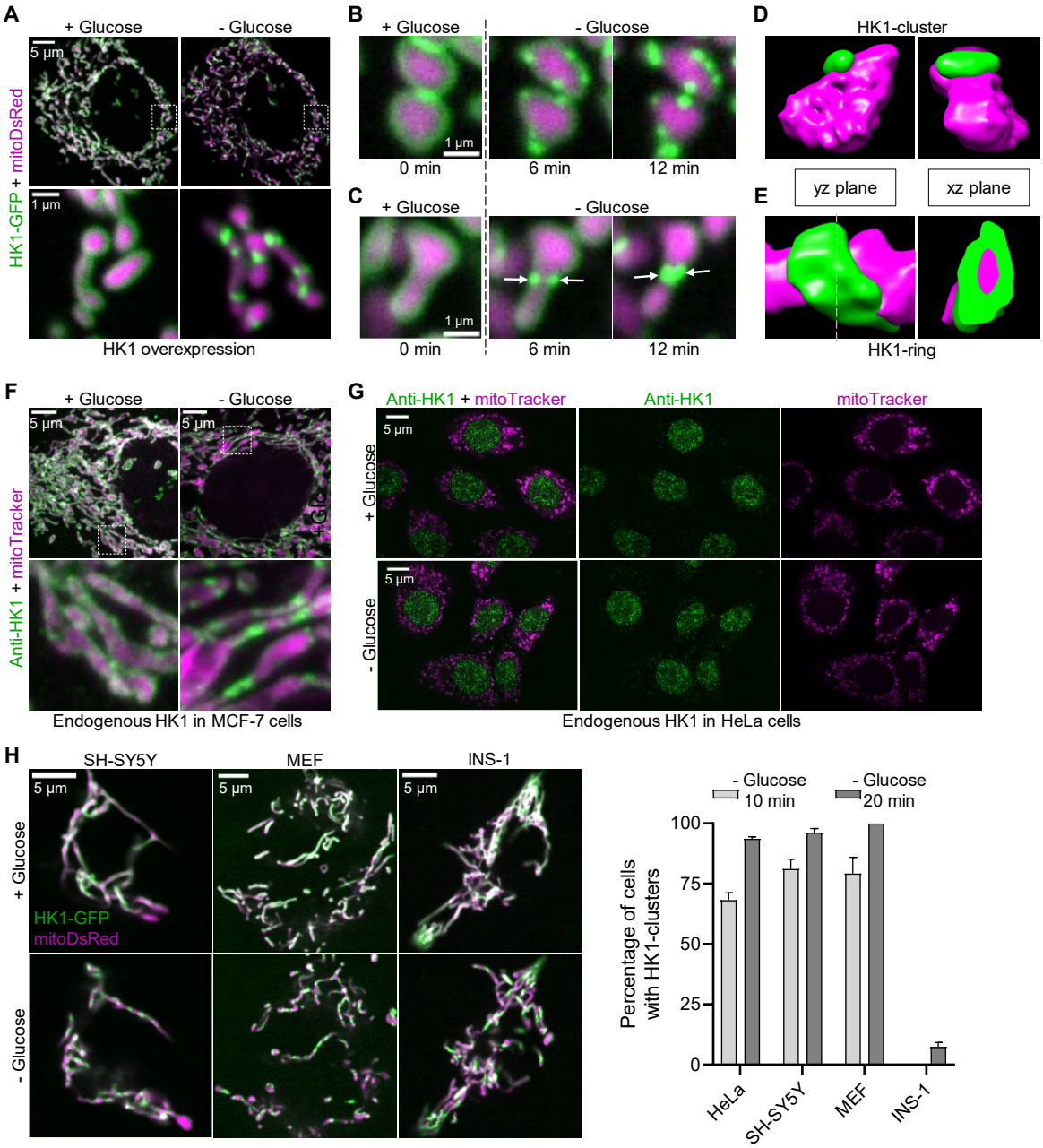

Figure 4. Hexokinase 1 clusters into ring-like structures during glucose depletion. (**A**) HK1 forms bright clusters when glucose is depleted. Confocal images of a HeLa cell expressing HK1-GFP and mitoDsRed with 10 mM glucose (left) and after 15 min of glucose depletion (right). The upper panels show an overview of the cell, and the dashed squares are magnified below.[184] (**B** and **C**) HK1-clusters grow in size and form ring-like structures around mitochondria. Time-lapse images of HeLa cells expressing HK1-GFP and mitoDsRed were acquired as glucose was depleted. The maturation of multiple HK1-clusters (B) or the formation of an HK1-ring (white arrows in C) is shown.[184] (**D** and **E**) 3D reconstructions reveal the shape of HK1-clusters and HK1-rings. Three-dimensional reconstruction of single mitochondria in HeLa cells expressing HK1-GFP and mitoDsRed. Shown are the frontal view (left panels) and side view (right panels) of an HK1-cluster and an HK1-ring.[184] (**F**) Endogenous HK1 in MCF-7 cells forms ring-like structures during glucose depletion. Immunofluorescence images of MCF-7 cells stained with anti-HK1 (green) and mitoTracker (magenta) with 10 mM glucose (left) or after 30 min of glucose depletion (right). The upper panels show an overview of the cells, and the dashed squares are magnified below.[184] (**G**) Endogenous HK1 in HeLa locates to the nucleus. Immunofluorescence images of HeLa cells stained with anti-HK1 (green) and mitoTracker (magenta) with 10 mM glucose (top) or after 30 min of glucose depletion (bottom). (**H**) HK1-clustering occurs in various cell types. The left panel shows confocal images of SH-SY5Y, MEF, and INS-1 cells expressing HK1-GFP and mitoDsRed with 10 mM glucose

(top) and without glucose (bottom). The right bar graph shows the percentages of cells with HK1-clusters (mean ± SEM) as glucose is depleted for 10 min (light gray) or 20 min (dark gray). Number of cells: HeLa (n = 110), SH-SY5Y (n = 53), MEF (n = 24), INS-1 (n = 54).[184] [Figure panels reproduced from Pilic *et al*., 2024.]

The formation of HK1-clusters following glucose depletion closely correlated with the reduction in mitochondrial ATP levels (Figure 5A)[184]. Conversely, glucose levels decreased well before the formation of HK1-clusters (Figure 5A)[184]. We subsequently adjusted intracellular ATP and glucose levels and monitored HK1-clustering in HeLa cells permeabilized with digitonin. HK1-clusters rapidly formed after permeabilization (Figure 5D)[184]. Consistent with our hypothesis, addition of ATP caused the disassembly of HK1-clusters (Figure 5B and Figure 5D)[184]. Surprisingly, HK1-clusters did not disassemble in the presence of glucose in permeabilized cells (Figure 5E)[184]. Compared to ATP, glucose-6-phosphate (G6P) was more effective in disassembling HK1-clusters. (Figure 5B and Figure 5F)[184]. Importantly, the addition of G6P did not raise mitochondrial ATP levels (Figure 5C), suggesting that G6P cannot be metabolized to generate ATP in permeabilized cells. Binding of G6P to HK1 is weakened by phosphate.[197,198] Therefore, we investigated whether phosphate influences the formation of HK1-clusters. The addition of phosphate promoted HK1-clustering, even with G6P present (Figure 5G)[184]. We then investigated how ATP facilitates HK1-clustering in intact cells. We created a GFP-tagged version of the HK1 mutant (G862A), which is characterized by its impaired ATP-binding ability.[189] Cells containing the ATP-binding mutant showed a greater tendency to form clusters than those with the wild-type HK1 (Figure 5H)[184]. Given that AMPK is activated during energy stress and targets mitochondria,[199] we examined its potential impact on HK1-clustering. Activation of AMPK with AICAR did not induce HK1-clustering in the presence of glucose (Figure 5I, left panel)[184]. Inhibition of AMPK with dorsomorphin did not prevent HK1- clustering during glucose depletion (Figure 5I, right panel). Our data indicate that the absence of ATP and G6P drives HK1-clustering independently of AMPK activity.

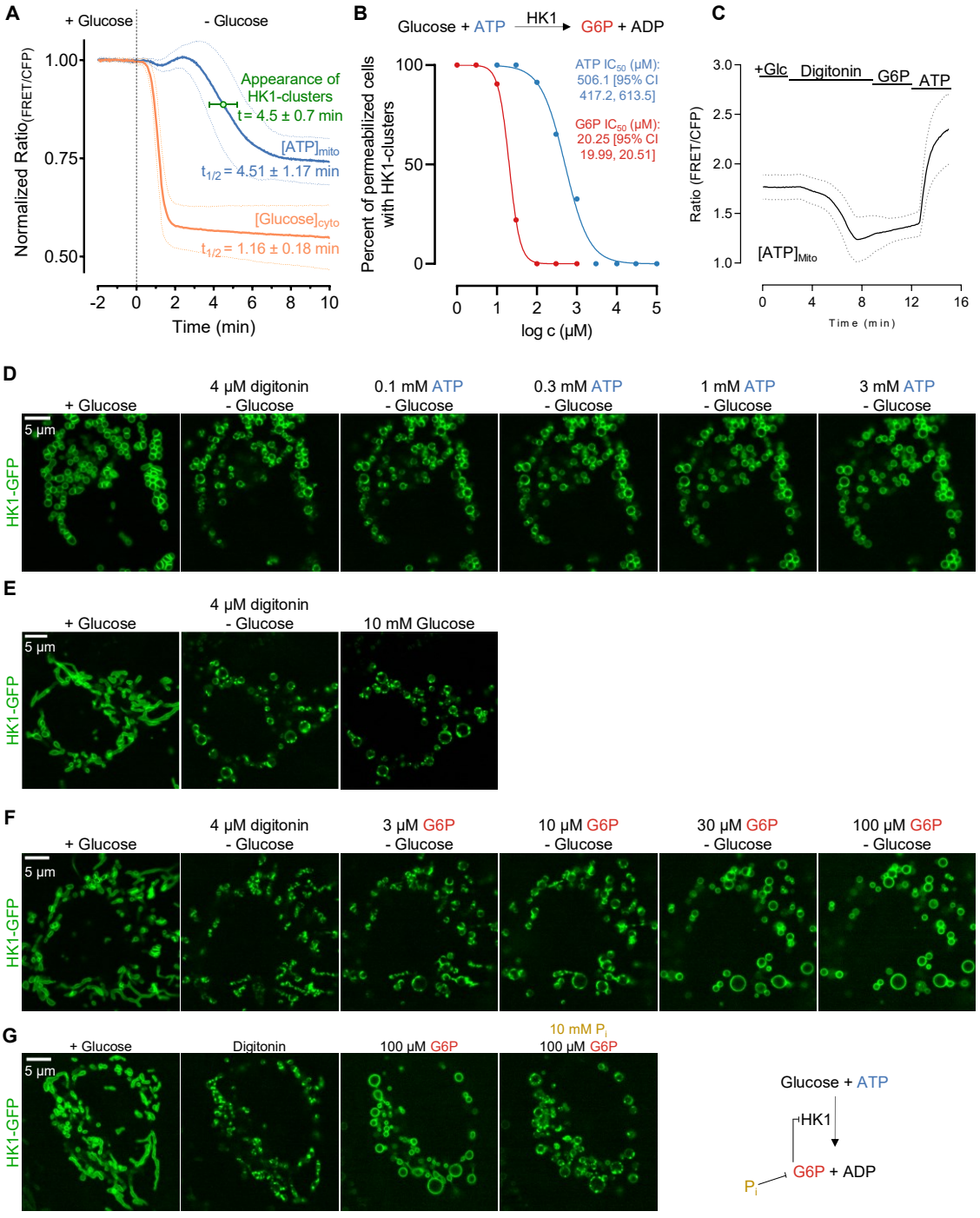
A
+ Glucose
- Glucose
Normalized Ratio(FRET/CFP)
1.00
0.75
0.50
Appearance of HK1-clusters
t= 4.5 ± 0.7 min
[ATP]mito
t1/2 = 4.51 ± 1.17 min
[Glucose]cyto
t1/2 = 1.16 ± 0.18 min
-2 0 2 4 6 8 10
Time (min)
B
Glucose + ATP
HK1
G6P + ADP
Percent of permeabilized cells with HK1-clusters
100
50
0
ATP IC50 (μM): 506.1 [95% CI 417.2, 613.5]
G6P IC50 (μM): 20.25 [95% CI 19.99, 20.51]
0 1 2 3 4 5
log c (μM)
C
+Glc
Digitonin
G6P
ATP
Ratio (FRET/CFP)
3.0
2.5
2.0
1.5
1.0
[ATP]Mito
0 4 8 12 16
Time (min)
D
+ Glucose
4 μM digitonin - Glucose
0.1 mM ATP - Glucose
0.3 mM ATP - Glucose
1 mM ATP - Glucose
3 mM ATP - Glucose
5 μm
HK1-GFP
E
+ Glucose
4 μM digitonin - Glucose
10 mM Glucose
5 μm
HK1-GFP
F
+ Glucose
4 μM digitonin - Glucose
3 μM G6P - Glucose
10 μM G6P - Glucose
30 μM G6P - Glucose
100 μM G6P - Glucose
5 μm
HK1-GFP
G
+ Glucose
Digitonin
100 μM G6P
10 mM Pi
100 μM G6P
5 μm
HK1-GFP
Glucose + ATP
HK1
G6P + ADP
Pi

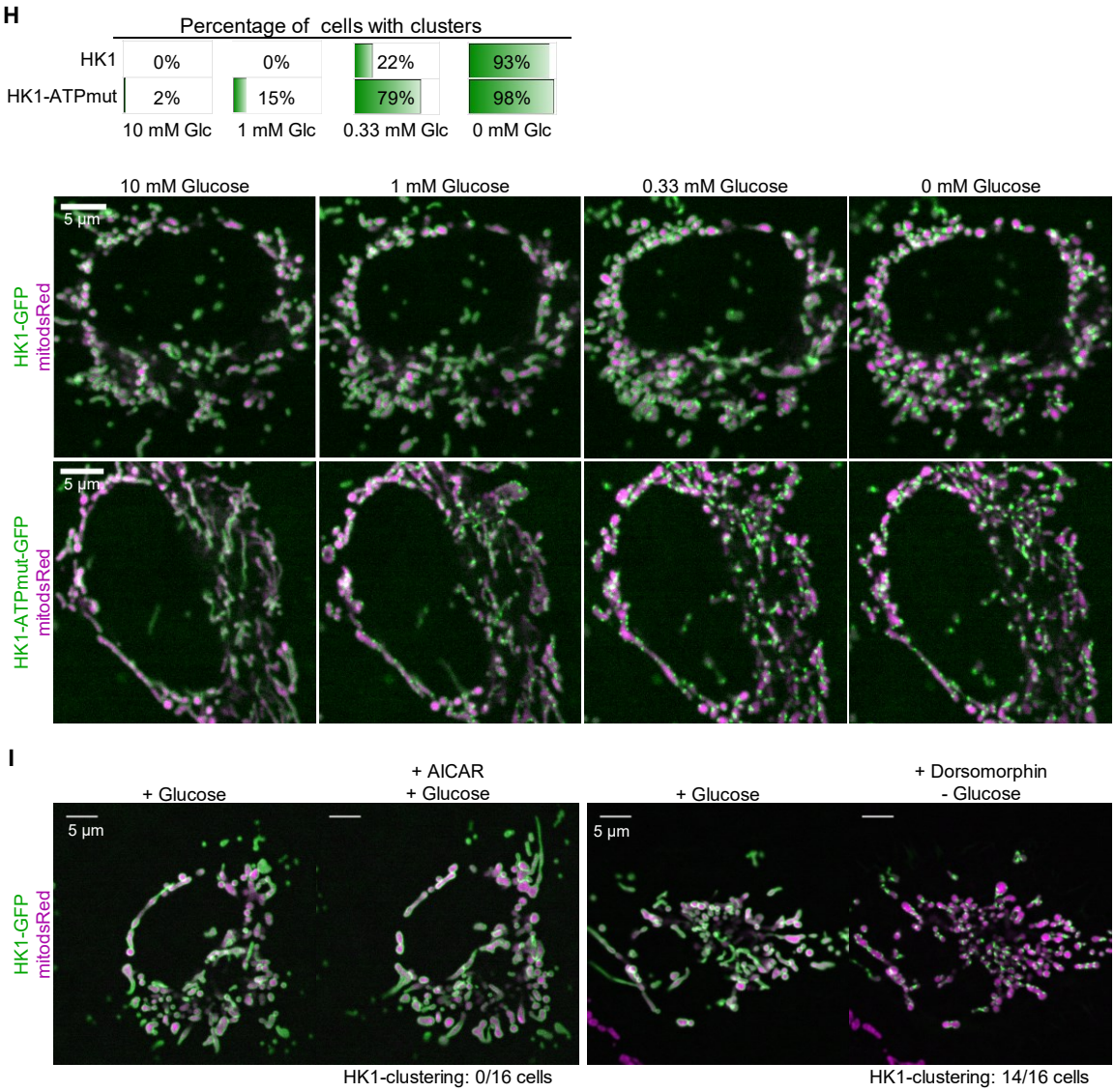

Figure 5. Lack of ATP and G6P drives HK1-clustering. (**A**) The appearance of HK1-clusters correlates more tightly with mitochondrial ATP than cytosolic glucose levels. Shown are curves of mitochondrial ATP levels (blue, n = 123 HeLa cells expressing mtAT1.03) and cytosolic glucose levels (orange, n = 67 HeLa cells expressing FLII12Pglu-700uDelta6) as glucose is depleted. Time-lapse images of HeLa cells expressing HK1-GFP were acquired at intervals of 5 s and used to assess the appearance of HK1-clusters (green, n = 10) as glucose is depleted. Data are presented as mean ± SD.[184] (**B**) ATP and G6P disassemble HK1-clusters in a concentration-dependent manner. The mean inhibitory effects of ATP (blue, n = 46 cells) and G6P (red, n = 95 cells) on the proportion of digitonin-permeabilized HeLa cells with HK1-clusters are shown as logarithmic concentration-response curves.[184] (**C**) Cell permeabilization correlates with a drop in mitochondrial ATP. Shown are curves of mitochondrial ATP levels (blue, n = 7 HeLa cells expressing mtAT1.03) as cells are permeabilized with 4 µM digitonin before being treated with 100 µM G6P and 2 mM ATP. Data are presented as mean ± SD. (**D**-**F**) ATP and glucose-6-phosphate (G6P) disassemble HK1-clusters in a concentration-dependent manner. Time-lapse images of HK1-GFP-expressing HeLa cells permeabilized with 4 µM digitonin before being treated with ATP (D), glucose (E), or G6P (F). Time-lapse images were acquired at intervals of 7 min.[184] (**G**) Phosphate (Pi) promotes HK1-clustering despite the presence of G6P. Time-lapse images of HK1-GFP-expressing HeLa cells permeabilized with 4 µM digitonin before being treated with G6P and Pi. Time-lapse images were acquired at intervals of 7 min. The circuit on the right shows the regulation of the HK1 reaction.[184] (**H**) The ATP-binding mutant (G862A) is more likely to form clusters than the wild-type enzyme. Time-lapse images of HeLa cells expressing mitoDsRed and HK1-GFP or HK1-ATPmut-GFP were acquired at intervals of 7 min as glucose was gradually depleted (bottom). The percentages of cells with clusters of HK1

(n = 41) and HK1-ATPmut (n = 47) were calculated (top).[184] (**I**) HK1 forms clusters independent of AMPK activity. Confocal images of HeLa cells expressing HK1-GFP and mitoDsRed with glucose and after 15 min of treatment with 1 mM AICAR (left panel) or after 15 min of glucose depletion in the presence of 10 μM dorsomorphin (right panel). [Figure panels reproduced from Pilic *et al.*, 2024.]

3.2 HK1-rings constrict mitochondria at contact sites with the ER

We noticed that mitochondria were constricted where HK1-rings formed (Figure 6A, left panel)[184]. To investigate this, we coexpressed HK1-GFP with mitoDsRed and measured the mitochondrial matrix at these sites of HK1-rings. When glucose was removed, the matrix diameter at HK1-rings significantly reduced. This constriction reversed once glucose was reintroduced and the HK1-rings disassembled. (Figure 6A, right graph)[184]. Given that actin plays a role in mitochondrial constriction,[200,201] we investigated how actin polymerization influences the formation of HK1-rings. To assess actin distribution relative to HK1, we coexpressed HK1-GFP and mCh-Actin. Inhibiting actin polymerization did not affect HK1 localization when glucose was available or prevent the formation of HK1-rings after glucose deprivation (Figure 6B)[184]. Since we noted reduced mitochondrial motility during glucose depletion, we also investigated whether inhibiting tubulin polymerization impacted HK1 ring formation by coexpressing HK1-GFP with tagRFP-Tubulin. Inhibition of tubulin polymerization did not affect HK1 localization or the formation of HK1-rings (Figure 6C). These results indicate that actin and tubulin polymerization are not essential for the formation of HK1-rings.

We speculated that the formation of HK1-rings might lead to a decrease in the density of cristae membranes at the sites where mitochondria are constricted. To visualize changes in mitochondrial structure, we coexpressed HK1-GFP with ComplexIV8-mRuby2, a marker targeting the cristae membranes. The regions occupied by HK1-rings were devoid of cristae membranes (Figure 7A)[184]. To determine if the mitochondrial matrix was present in cristae-deficient regions, we introduced mitoBFP, a blue fluorescent marker of the mitochondrial matrix. (Figure 7B)[184]. HK1-rings exhibited significantly reduced colocalization with cristae membranes compared to the mitochondrial matrix. (Figure 7D)[184].

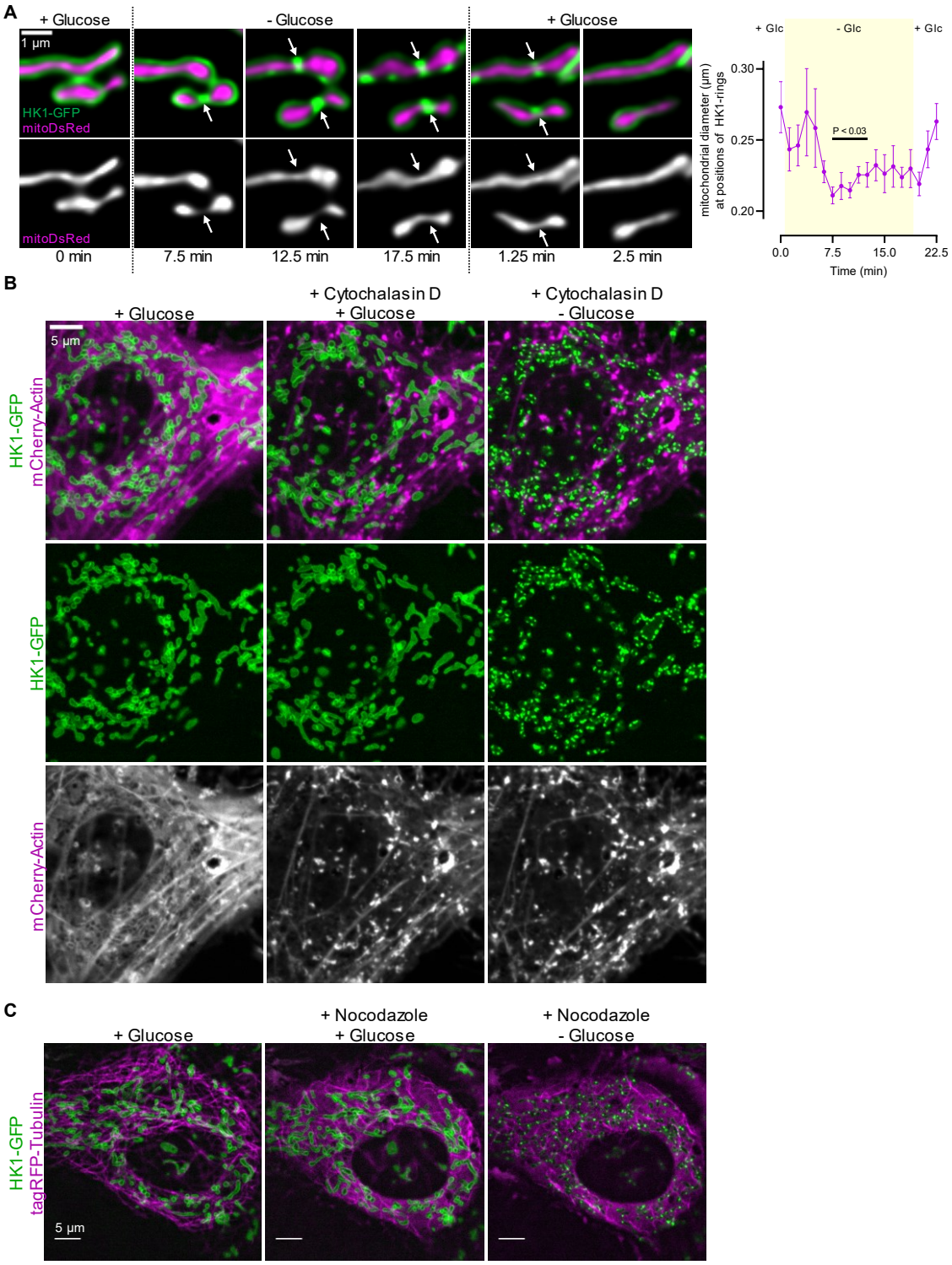

Figure 6. HK1-rings constrict mitochondria. (**A**) HK1-rings constrict mitochondria. Time-lapse images of a HeLa cell expressing HK1-GFP and mitoDsRed were acquired as glucose was removed and readded (left panel). Images are maximum intensity projections of z-stacks (6 sections, spaced 0.2 µm apart). Arrows indicate sites of mitochondrial constriction at positions of HK1-rings. The diameter of the mitochondrial matrix (mean ± SEM, n = 7) was measured at positions of HK1-rings (right graph). The difference between basal and glucose-depleted mitochondrial diameter was evaluated using one-way ANOVA with Dunnett post hoc test.[184] (**B**) The formation of HK1-rings does not require actin polymerization. Time-lapse images of a HeLa cell expressing HK1-GFP and mCherry-Actin were acquired at intervals of 10 min under three different conditions: With 10 mM glucose (left), after treatment with 10 µM cytochalasin D (middle), and after glucose depletion in the presence of 10 µM cytochalasin D (right).[184] (**C**) The formation of HK1-rings does not require tubulin

polymerization. Time-lapse images of a HeLa cell expressing HK1-GFP and mCherry-Actin were acquired at intervals of 10 min under three different conditions: With 10 mM glucose (left), after treatment with 5 µg/ml nocodazole (middle), and after glucose depletion in the presence of 5 µg/ml nocodazole (right). [Figure panels reproduced from Pilic *et al*., 2024.]

Next, we tested whether cristae junction proteins are also displaced from the positions of HK1-rings. Therefore, we coexpressed HK1-mRuby3 with a marker of mitochondrial calcium uptake 1 (MICU1), which contributes to the structural integrity of cristae junctions.[175] MICU1 was displaced by HK1-rings during glucose deprivation (Figure 7C). These results suggest that cristae are displaced at the sites of HK1-rings.

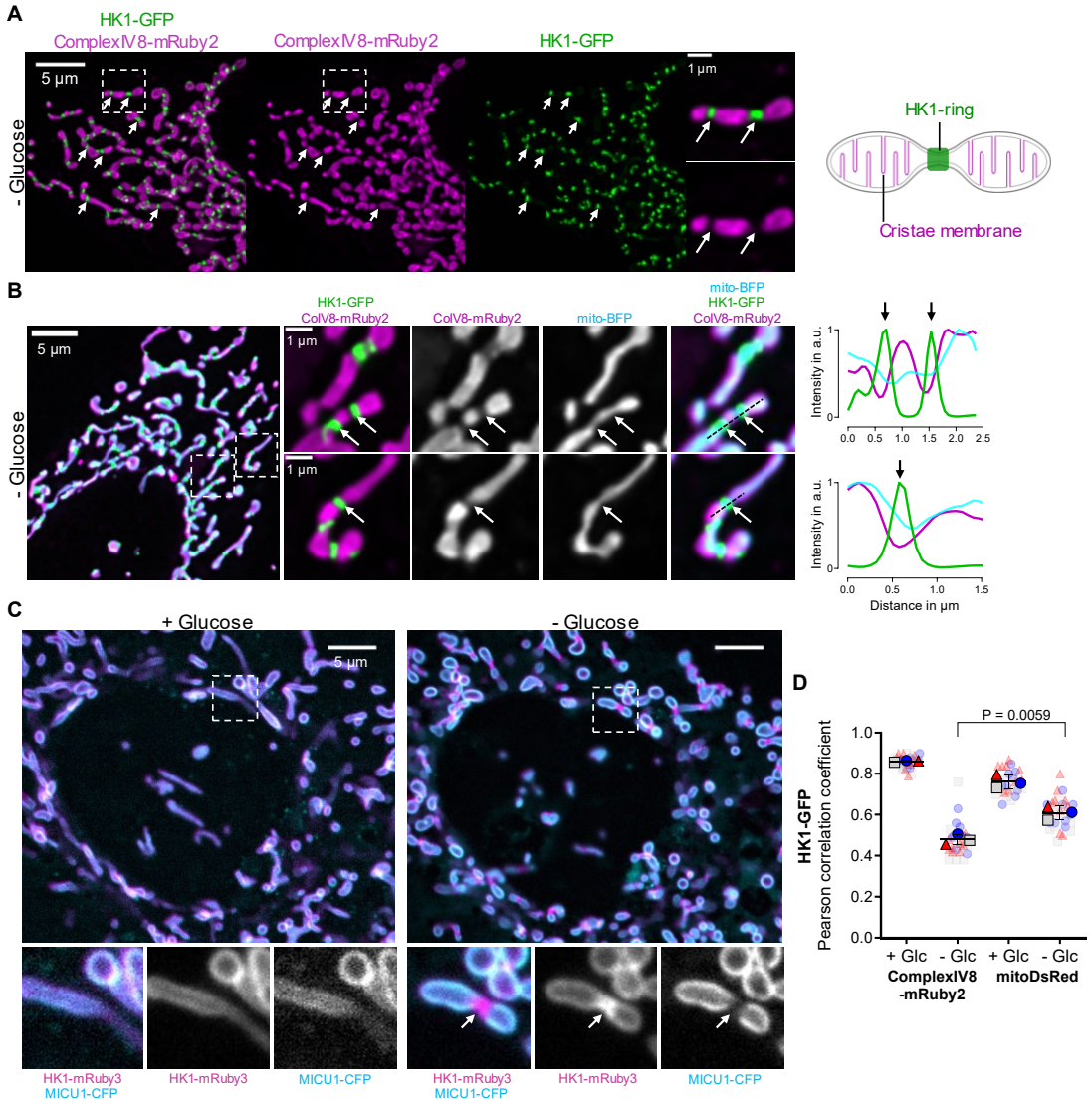

Figure 7. HK1-rings displace cristae. (**A**) Cristae membranes are absent at positions of HK1-rings. Confocal images of a HeLa cell expressing HK1-GFP and ComplexIV8-mRuby2 (cristae membrane) after 15 min of glucose depletion (left panel). Images are maximum intensity projections of z-stacks (51 sections, spaced 0.2 µm apart). Arrows indicate positions of HK1-rings. Dashed squares are magnified on the right side of the overview images. Cartoon shows that cristae membranes are displaced at positions of HK1-rings (right).[184] (**B**) Mitochondrial matrix is present in cristae-free regions at positions of HK1-rings. Confocal images of a HeLa cell expressing HK1-GFP,

ComplexIV8-mRuby2 (cristae membrane), and mitoBFP (matrix) after 15 min of glucose depletion. Images are maximum intensity projections of z-stacks (36 sections, spaced 0.2 µm apart). The left image shows an overview of the cell, and the dashed squares are magnified on the right side. Dashed lines represent line scan graphs on the right and show the relative fluorescence intensity of HK1 (green), cristae membrane (magenta), and mitochondrial matrix (blue) along the length of the line. Arrows point to positions of HK1-rings.[184] (**C**) HK1-rings displaces cristae junction proteins. Confocal images of a HeLa cell expressing HK1-mRuby3 and MICU1-CFP before (left) after 15 min of glucose depletion (right). Dashed squares are magnified below the overview images. Arrows indicate positions of HK1-rings. (**D**) HK1-rings colocalize less with cristae membrane than with mitochondrial matrix. The Pearson correlation coefficient is shown between HK1-GFP and ComplexIV8-mRuby2 (cristae membrane), or mitoDsRed (matrix) with 10 mM glucose or after 15 min of glucose depletion. The beeswarm SuperPlot represents each cell with a color-coded dot according to the experimental day. Two-tailed unpaired t-test was used for statistical analysis (n = 3). Data are presented as mean ± SD.[184] [Figure panels reproduced from Pilic *et al*., 2024.]

Given that the ER plays a role in the constriction of mitochondrial,[202,203] we examined if HK1-rings are associated with the ER marker BFP-KDEL. HK1-rings were found to colocalize with the ER (Figure 8A, white arrows)[184]. It was frequently observed that HK1 clusters from adjacent mitochondria came into contact (Figure 8C)[184]. The ER was positioned at the interfaces where HK1-clusters were in contact (Figure 8A, yellow arrows)[184]. The vast majority of HK1-rings and HK1-clusters were found to colocalize with intersecting and adjacent ER tubules (Figure 8B)[184]. Next, we investigated the temporal correlation between the ER and the formation of HK1-rings. We coexpressed HK1-GFP with mCh-Sec61β, a membrane ER marker. During imaging we observed that the ER is located at regions of HK1-rings already before the formation of HK1-rings (Figure 8D). Since mitochondria DNA (mtDNA) replication occurs at ER-mitochondria contact sites,[204] we investigated the temporal correlation between mtDNA and forming HK1-rings. We expressed HK1-GFP and stained mtDNA with STYO13, a cell-permeant nucleic acid dye. During imaging we observed that the mtDNA is located at positions of HK1-rings before HK1-rings had formed (Figure 8E). These data indicate that the ER could play a crucial role in directing where HK1-rings form under energy stress conditions.

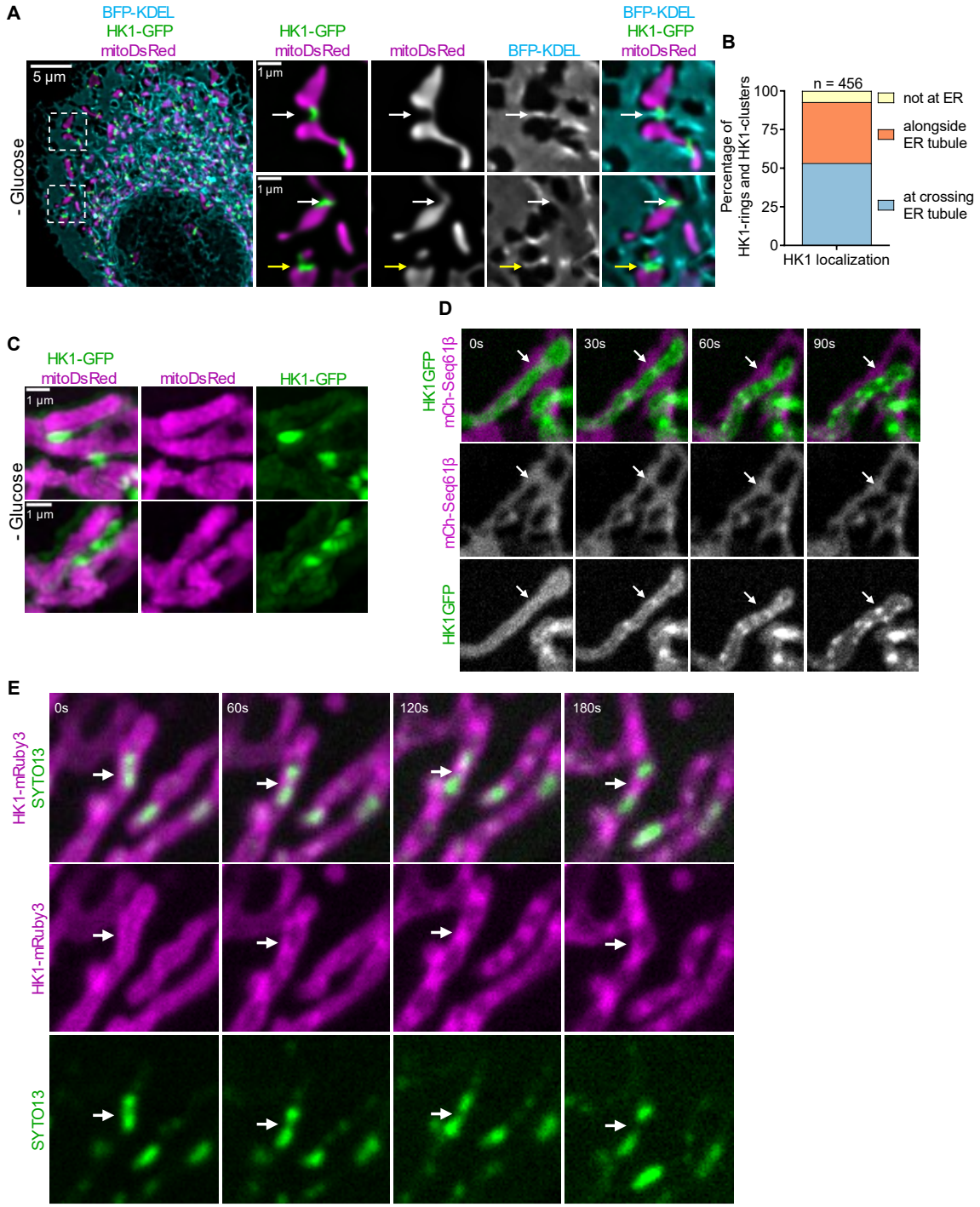

Figure 8. HK1-rings are located at ER-mitochondrial contact sites. (**A**) Confocal images of a HeLa cell expressing HK1-GFP, mitoDsRed, and BFP-KDEL (ER) after 15 min of glucose depletion. The left image shows an overview of the cell, and the dashed squares are magnified on the right side. White arrows point to positions of HK1-rings, and yellow arrows to HK1-clusters.[184] (**B**) The majority of HK1-rings and HK1-clusters are localized at the ER. Bar graph shows the percentage of HK1-rings and HK1-clusters that colocalize with the ER membrane after 15 min of glucose depletion (n = 456).[184] (**C**) HK1-clusters of neighboring mitochondria were frequently observed in contact. Structured illumination microscopy images of HeLa cells expressing HK1-GFP and mitoDsRed, showing that HK1-clusters from neighboring mitochondria are in lattice contacts. Images are maximum intensity projections of z-stacks (33 sections, spaced 0.1 µm apart).[184] (**D**) ER is present before the formation of HK1-rings. Time-lapse images of a HeLa cell expressing HK1-GFP and mCh-Seq61β were acquired at intervals of 30 s as glucose was removed right before the formation of HK1-

rings. Arrows indicate positions of HK1-rings. (**E**) Mitochondrial DNA is present before the formation of HK1-rings. Time-lapse images of a HeLa cell expressing HK1-mRuby3 and the nucleic acid dye SYTO13 were acquired at intervals of 60 s as glucose was removed right before the formation of HK1-rings. Arrows indicate positions of HK1-rings. [Figure panels A-C reproduced from Pilic *et al*., 2024.]

3.3 HK1-rings interfere with Drp1 and block mitochondrial fission

Given that Drp1 is vital for the constriction and division of mitochondria,[205] we explored the potential colocalization of HK1-rings with mCh-Drp1 and tracked their dynamics during glucose deprivation. We noted a reduction in Drp1,clusters during glucose deprivation, coinciding with the formation of HK1-rings (Figure 9A and Figure 9B)[184]. The overexpression of HK1 notably diminished the number of Drp1 clusters during glucose deprivation (Figure 9A and Figure 9B)[184]. HK1-rings and Drp1-clusters showed minimal colocalization (Figure 9C and Figure 9D)[184]. Glucose readdition increased Drp1-clusters and led to the disassembly of HK1-rings (Figure 9B)[184]. Mitochondrial fission, mediated by Drp1-clusters, was detected at only a few regions where HK1.rings had disassembled (Figure 9E)[184]. Next, we explored whether HK1-rings affect the localization of other outer mitochondrial membrane proteins by coexpressing HK1-GFP with mTagBFP2-TOMM20-N-10. The TOM20 maker was absent in regions of HK1-rings (Figure 9F)[184]. We then investigated how different receptors for Drp1, including Mff, MiD51, and Fis1, influence HK1-ring-formation. Coexpressing mCh-Mff or mCh-MiD51 with HK1-GFP showed similar percentages of cells with HK1-rings as control cells expressing only HK1-GFP (Figure 9G).[184] However, overexpressing the mCh-Fis1, which only contains the membrane anchor of Fis1, completely inhibited the formation of HK1-rings (Figure 9G)[184], indicating that excessive Fis1 membrane anchors inhibits HK1-ring-formation. Further testing with HK1-mRuby3 in U2OS cells expressing endogenous Fis1-GFP,[206] revealed that the signal of endogenous Fis1 was diminished in areas where HK1 rings were present (Figure 9H),[184] indicating that HK1-rings and Fis1 cannot occupy the same regions. During glucose deprivation, the emergence of HK1-rings coincided with the localized and time-dependent disintegration of Mff-clusters. (Figure 9I)[184]. Mff triggered mitochondrial fission at a few areas where HK1-rings had disassembled during glucose reintroduction, paralleling Drp1's pattern. (Figure 9I)[184]. During glucose deprivation, HK1-rings appeared at sites of MiD51-rings (Figure 9J)[184], which, unlike Mff-clusters, remained stable at these sites (Figure 9J)[184]. Glucose reintroduction led to MiD51-ring disassembly and

mitochondrial division (Figure 9K)[184]. Our data suggest that HK1-rings may obstruct Drp1 from binding to the fission receptors, thereby hindering mitochondrial fission.

The expression of HK1-GFP in HeLa cells appeared to reduce mitochondrial fission events. To substantiate this observation, we compared the mitochondrial morphology of glucose-deprived HeLa cells expressing HK1-GFP with non-expressing counterparts during treatment with FCCP, a potent mitochondrial fission inducer. Mitochondrial morphology changes were assessed by the aspect ratio (AR), where a low AR indicates fragmented mitochondria and a high AR signifies elongated mitochondria. FCCP treatment caused significant mitochondrial fragmentation in HeLa cells without HK1-GFP (Figure 9L, upper panel)[184]. FCCP treatment was ineffective in inducing mitochondrial fission in HeLa cells that expressed HK1-GFP (Figure 9L, lower panel)[184]. The results demonstrate that HK1-rings mitigate mitochondrial fission caused by FCCP in an energy deprived state.

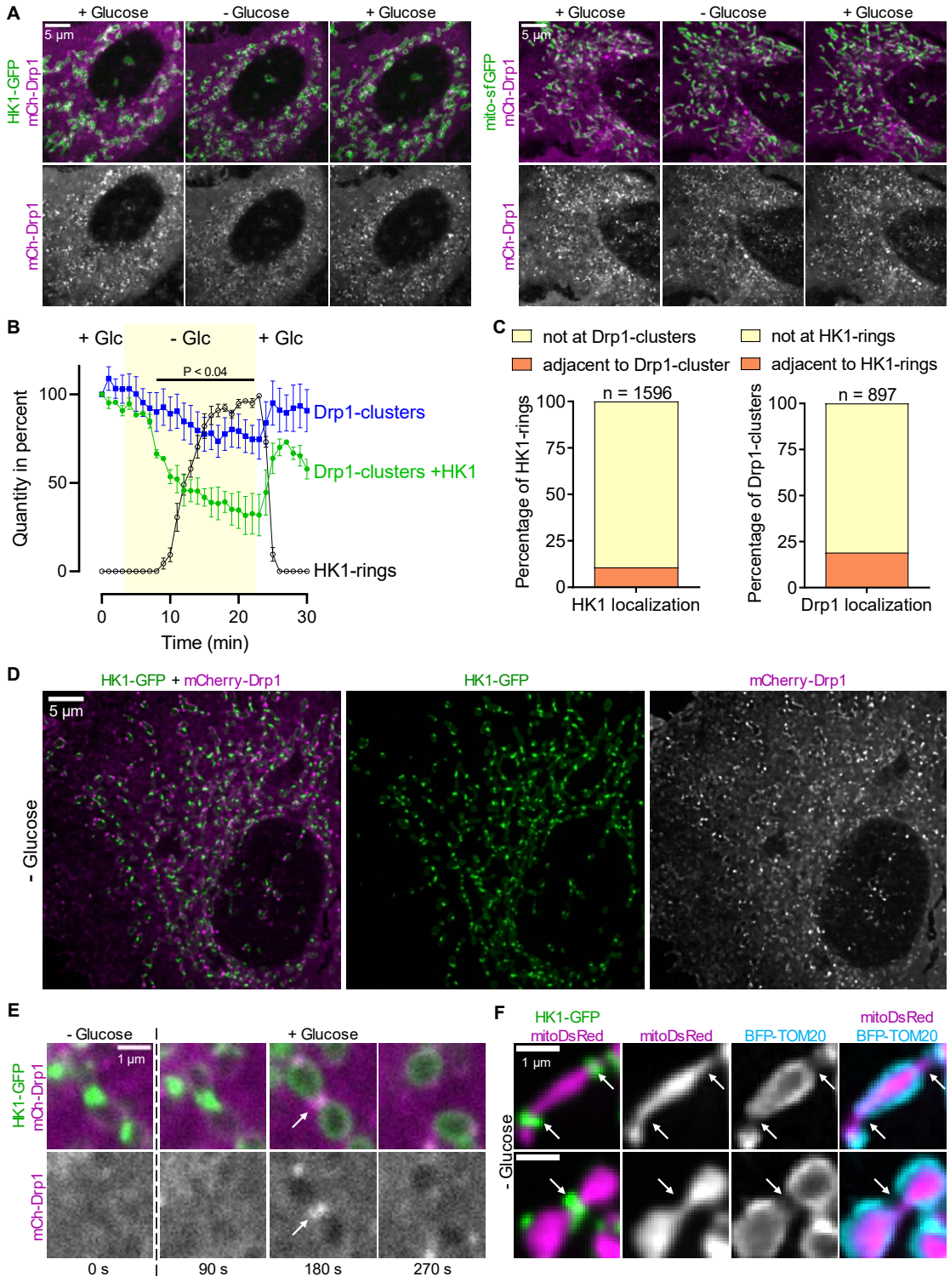
A
+ Glucose
- Glucose
+ Glucose
5 µm
HK1-GFP
mCh-Drp1
mCh-Drp1
mito-sfGFP
mCh-Drp1
B
+ Glc
- Glc
+ Glc
P < 0.04
Quantity in percent
100
50
0
Drp1-clusters
Drp1-clusters +HK1
HK1-rings
0
10
20
30
Time (min)
C
not at Drp1-clusters
adjacent to Drp1-cluster
not at HK1-rings
adjacent to HK1-rings
n = 1596
n = 897
Percentage of HK1-rings
Percentage of Drp1-clusters
100
75
50
25
0
HK1 localization
Drp1 localization
D
HK1-GFP + mCherry-Drp1
HK1-GFP
mCherry-Drp1
5 µm
- Glucose
E
- Glucose
+ Glucose
1 µm
HK1-GFP
mCh-Drp1
mCh-Drp1
0 s
90 s
180 s
270 s
F
HK1-GFP
mitoDsRed
mitoDsRed
BFP-TOM20
mitoDsRed
BFP-TOM20
1 µm
- Glucose

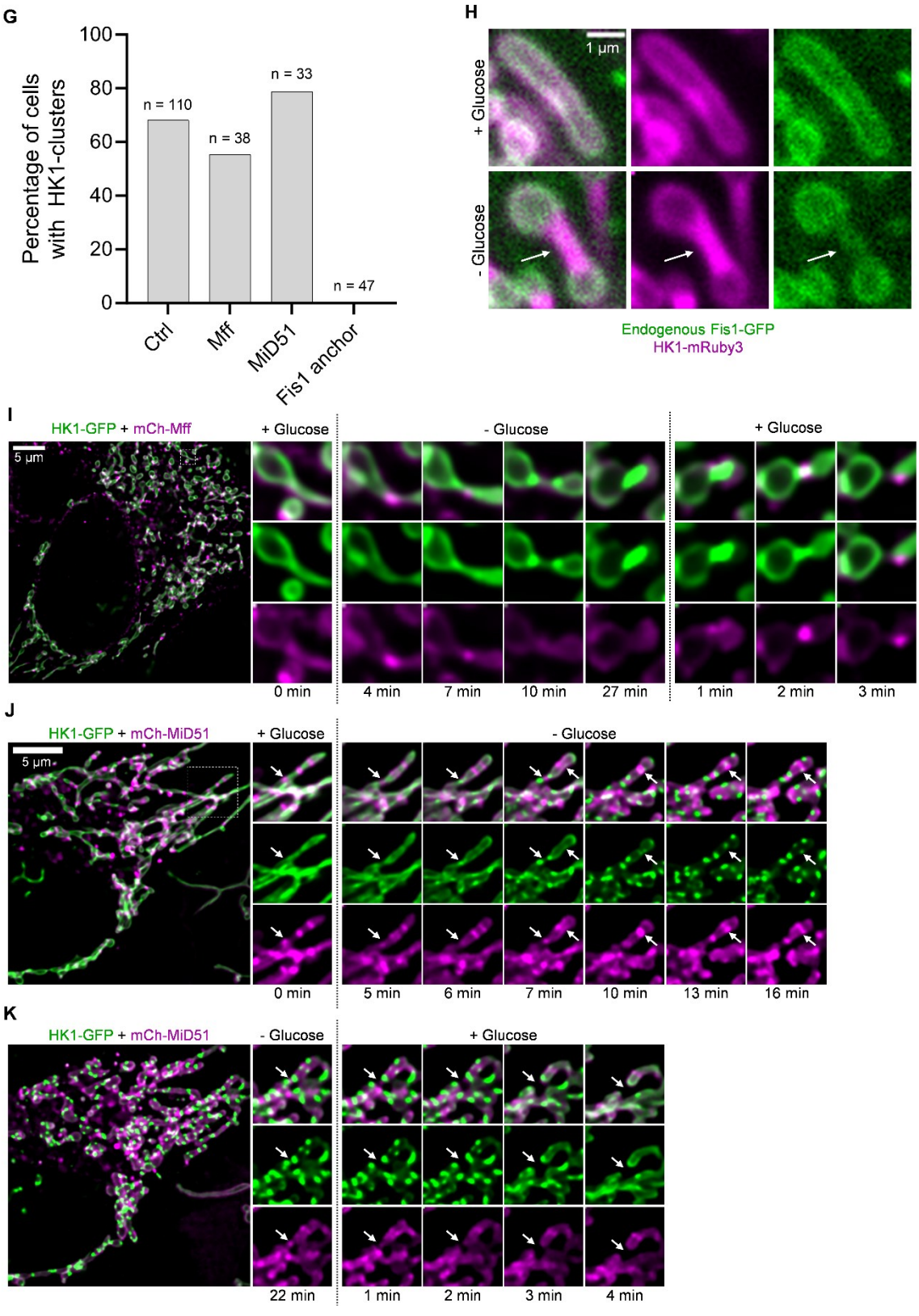
G
Percentage of cells with HK1-clusters
100
80
60
40
20
0
n = 110
n = 38
n = 33
n = 47
Ctrl
Mff
MiD51
Fis1 anchor
H
1 µm
+ Glucose
- Glucose
Endogenous Fis1-GFP
HK1-mRuby3
I
HK1-GFP + mCh-Mff
5 µm
+ Glucose
- Glucose
+ Glucose
0 min
4 min
7 min
10 min
27 min
1 min
2 min
3 min
J
HK1-GFP + mCh-MiD51
5 µm
+ Glucose
- Glucose
0 min
5 min
6 min
7 min
10 min
13 min
16 min
K
HK1-GFP + mCh-MiD51
- Glucose
+ Glucose
22 min
1 min
2 min
3 min
4 min

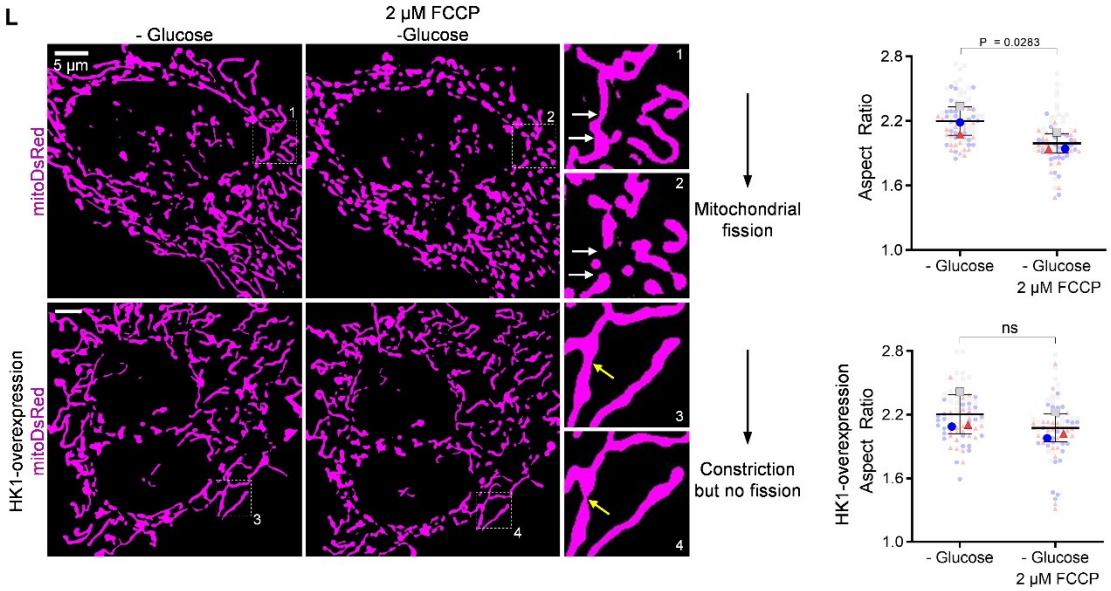

Figure 9. HK1-rings displace Drp1 and prevent mitochondrial fission during energy stress. (**A**) Overexpression of HK1 significantly reduced the number of Drp1-clusters during energy stress. Confocal images of HeLa cells expressing mCherry-Drp1 with HK1-GFP (left panel) or mito-sfGFP (right panel) as 10 mM glucose (left) was removed for 20 min (middle) and readded for 4 min (right).[184] (**B**) HK1-rings reduced the number of Drp1-clusters during energy stress. Curves show the percentage of Drp1-clusters in HeLa cells (blue) and in HeLa cells that express HK1-GFP (green) relative to the percentage of HK1-rings (black) as glucose is removed and readded. Two-tailed unpaired t-test was used for statistical analysis between Drp1-clusters and Drp1-clusters +HK1. Data are presented as mean ± SEM.[184] (**C**) The majority of HK1-rings and Drp1-clusters did not colocalize. Bar graphs show the percentage of HK1-rings (n = 1596) that were adjacent to Drp1-clusters (left) and the percentage of Drp1-clusters (n = 897) that were adjacent to HK1-rings (right) after 15 min of glucose depletion.[184] (**D**) The majority of HK1-rings and Drp1-clusters did not colocalize. Representative confocal image of a HeLa cell expressing HK1-GFP and mCherry-Drp1 after 15 min of glucose depletion. The image is a maximum intensity projection of z-stacks (41 sections, spaced 0.2 µm apart).[184] (**E**) HK1-ring disassembly allowed Drp1-clusters to move into constriction sites and induce mitochondrial fission. Time-lapse images of a glucose-depleted HeLa cell expressing HK1-GFP and mCherry-Drp1 were acquired at intervals of 90 s as 10 mM glucose was readded. Arrow indicates the position of an HK1-ring.[184] (**F**) HK1-rings displace proteins of the outer mitochondrial membrane. Confocal images of a HeLa cell expressing HK1-GFP, mitoDsRed, and mTagBFP2-TOMM20-N-10 after 15 min of glucose depletion. Images are maximum intensity projections of z-stacks (35 sections, spaced 0.2 µm apart). Arrows indicate positions of HK1-rings.[184] (**G**) Fis1 anchor overexpression prevents the formation of HK1-rings. Graph shows the percentages of HeLa cells with clusters after 10 min of glucose depletion. HK1-GFP + mitoDsRed (n = 110), HK1-GFP + mCh-Mff (n = 38), HK1-GFP + mCh-MiD51 (n = 33), HK1-GFP + mCh-Fis1 (n = 47).[184] **(H)** HK1-rings displace endogenous Fis1. Confocal images of a U2OS cell that overexpress HK1-mRuby3 (magenta) and endogenously express Fis1-GFP (green) before (top panel) and after 10 min of glucose depletion (bottom panel). Arrows indicate positions of HK1-rings.[184] (**I**) The formation of HK1-rings correlates with the disassembly of Mff-clusters. Confocal images of a HeLa cell expressing HK1-GFP and mCh-Mff. The left image shows an overview of the cell in the presence of glucose, and the dashed square is magnified on the right side. Time-lapse images were acquired as glucose was removed and readded.[184] (**J**) HK1-rings formed at sites of MiD51-rings. Confocal images of a HeLa cell expressing HK1-GFP and mCh-MiD51.The left image shows an overview of the cell in the presence of glucose, and the dashed square is magnified on the right side. Time-lapse images were acquired as glucose was removed. White arrows point to positions of HK1-rings.[184] (**K**) MiD51 disassembly leads to mitochondrial fission. Confocal images of a HeLa cell expressing HK1-GFP and mCh-MiD51. The left image shows an overview of the cell in the absence of glucose, and the dashed square is magnified on the right side. Time-lapse images were acquired as glucose was readded.[184] (**L**) HK1-rings prevent FCCP-induced mitochondrial fission during energy stress. Thresholded images of mitoDsRed signal in HeLa cells (top panel) and in HeLa cells that overexpress HK1-GFP (bottom panel). Glucose was depleted for 30 min before imaging (leftmost images). The

middle images show the cells after perfusion with 2 µM FCCP for 20 min. Numbered dashed squares are magnified on the right side of the overview images. White arrows indicate mitochondrial fission, and yellow arrows indicate mitochondrial constriction. The beeswarm SuperPlot represents each cell with a color-coded dot according to the experimental day (right). Two-tailed paired t-test was used for statistical analysis (n = 3). Data are presented as mean ± SD.[184] [Figure panels reproduced from Pilic *et al*., 2024.]

3.4 Influence of HK1-rings on Parkin translocation during energy stress

As mitochondrial fission is required for mitochondrial degradation,[206] we explored the potential impact of HK1-rings on Parkin translocation from the cytosol to the mitochondria, which promotes the degradation of damaged mitochondria.[207] Using HeLa cells expressing HK1-GFP and mCherry-Parkin, we observed that Parkin did not translocate to the mitochondria during glucose depletion (Figure 10A). Furthermore, mitochondrial depolarization with FCCP failed to induce Parkin translocation in the absence of glucose in HeLa cells (Figure 10B), aligning with previous observations.[208] In contrast, FCCP treatment facilitated Parkin translocation to the mitochondria in the presence of glucose (Figure 10C). FCCP treatment failed to induce the formation of HK1-rings when glucose was present (Figure 10D), making it challenging to assess the influence of HK1-rings on Parkin translocation.

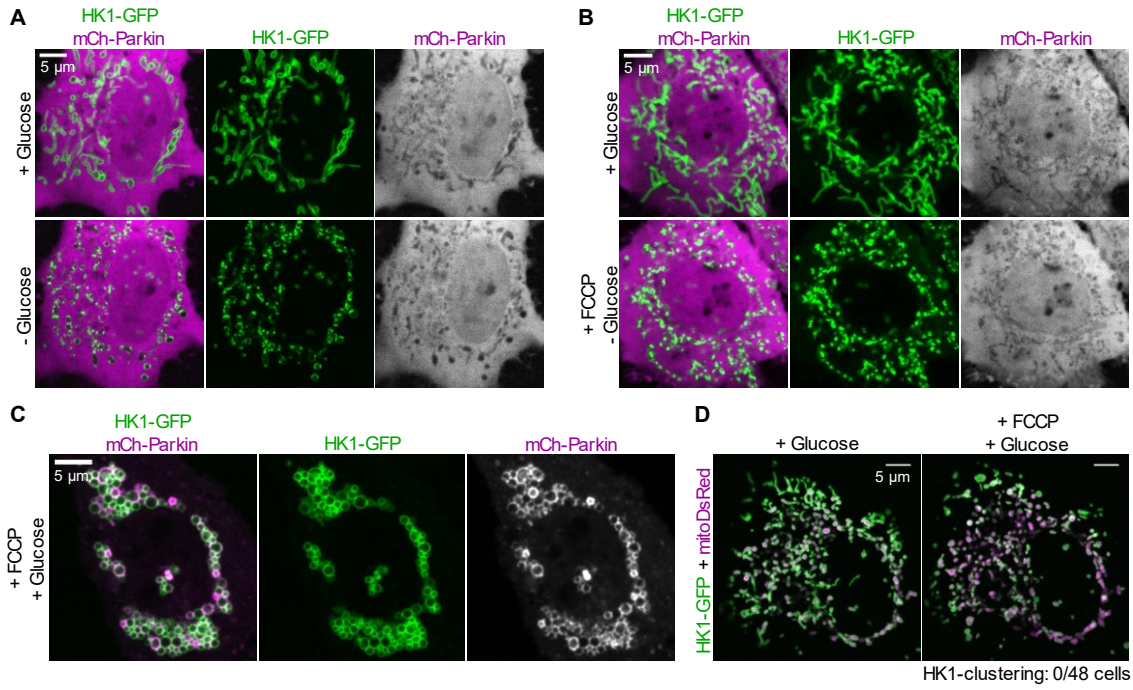

Figure 10. Influence of HK1-rings on Parkin translocation. (**A**) Parkin does not translocate to mitochondria during glucose depletion. Confocal images of a HeLa cell expressing HK1-GFP and

mCh-Parkin with glucose (top row) and after 15 min of glucose depletion (bottom row). (**B**) Parkin does not translocate to mitochondria during FCCP treatment in the absence of glucose. Confocal images of a HeLa cell expressing HK1-GFP and mCh-Parkin with glucose (top row) and after 30 min of treatment with 10 µM FCCP in the absence of glucose (bottom row). (**C**) Parkin translocates to mitochondria during FCCP treatment in the presence of glucose. Confocal images of a HeLa cell expressing HK1-GFP and mCh-Parkin after 2 h of treatment with 10 µM FCCP in the presence of glucose. (**D**) HK1 does not form rings during FCCP treatment in the presence of glucose. Confocal images of a HeLa cell expressing HK1-GFP and mitoDsRed with glucose (left) and after 10 min of treatment with 10 µM FCCP (right).

3.5 The structure of HK1 regulates the formation of HK1-rings

Next, we tested whether other mitochondrial hexokinases are able to form rings. Although HK2 shares high structural similarity with HK1, HK2 did not form rings in the absence of glucose (Figure 12A)[184]. In contrast, HKDC1, which also shares high structural similarity with HK1,[54] did form clusters in the absence of glucose (Figure 12A)[184], however, HKDC1-clusters were less prominent and less frequently observed than HK1-clusters. These results suggest that the clustering ability of hexokinases is influenced by enzyme-specific structural features.

HK1 consists of two halves that share high structural similarity (Figure 11)[184]. Interestingly, the N-terminal half of HK1 is catalytically inactive and believed to have regulatory functions. The C-terminal half of HK1 is catalytically active. In HK2, both halves are catalytically active.[209] To determine the functional domain of HK1 responsible for clustering during glucose depletion, we engineered two chimeric proteins, combining the N-terminal and C-terminal regions of HK1 and HK2, each fused to GFP: HK1N-HK2C and HK2N-HK1C (Figure 12C)[184]. We then evaluated the extent of cluster formation in response to glucose deprivation. The majority of cells expressing the native HK1-GFP construct formed clusters after 10 min of glucose deprivation. In stark contrast, the HK2N-HK1C-GFP chimera failed to form clusters under these conditions (Figure 12B and Figure 12C),[184] indicating that the N-terminal half of HK1 is indispensable for clustering. Interestingly, a minority of cells expressing the HK1N-HK2C-GFP chimera showed clustering activity (Figure 12C and Figure 12D),[184] suggesting that the C-terminal region of HK1 contributes to but is not essential for clustering.

The N-terminal domain of HK1 harbors a 15-residue hydrophobic sequence that functions as a mitochondrial binding domain (MBD) (Figure 11)[184]. To determine the role of the MBD in HK1-clustering during glucose deprivation, we analyzed a

truncated form of HK1 that lacks this domain.[63] The truncated variant of HK1, confined to the cytosol, did not demonstrate clustering in the absence of glucose (Figure 12B and Figure 12E)[184]. This suggests that the MBD is required for clustering to occur. We tested the clustering capability of the isolated MBD by attaching it to GFP, resulting in the HK1MBD-GFP fusion protein. Expression of this construct in HeLa cells showed that HK1MBD-GFP was localized uniformly around mitochondria and did not cluster during glucose deprivation (Figure 12B and Figure 12E)[184]. Analysis of HK1-mRuby3 and HK1MBD-GFP during glucose starvation showed that HK1MBD-GFP was not present in the HK1-mRuby3 ring structures (Figure 12F)[184]. This observation implies that the MBD alone is not sufficient for incorporation into the HK1-ring complexes.

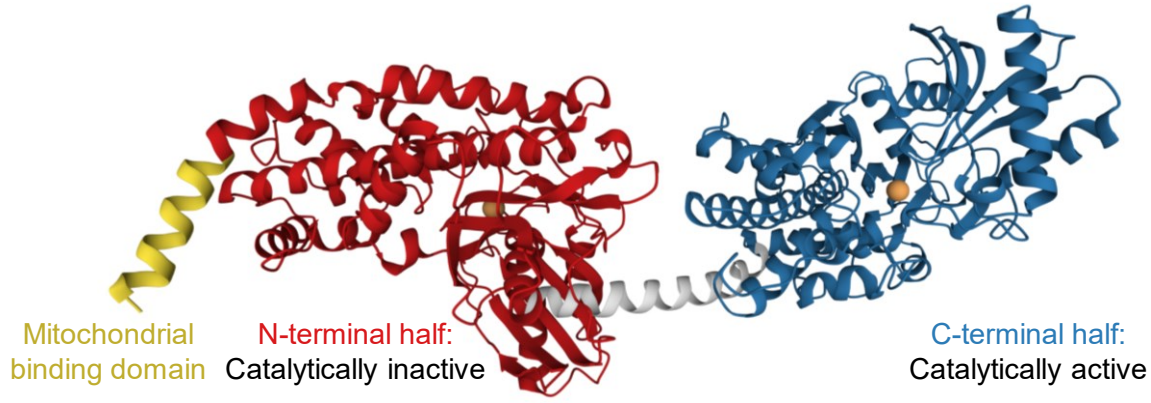

Figure 11. Structure of HK1. X-ray structures of full-length rat HK1 (PDB accession no. 1BG3). HK1 contains a mitochondrial binding domain (yellow), a catalytically inactive N-terminal half (red), and a catalytically active C-terminal half (blue). Glucose is shown as orange balls.[184] [Figure reproduced from Pilic *et al.*, 2024.]

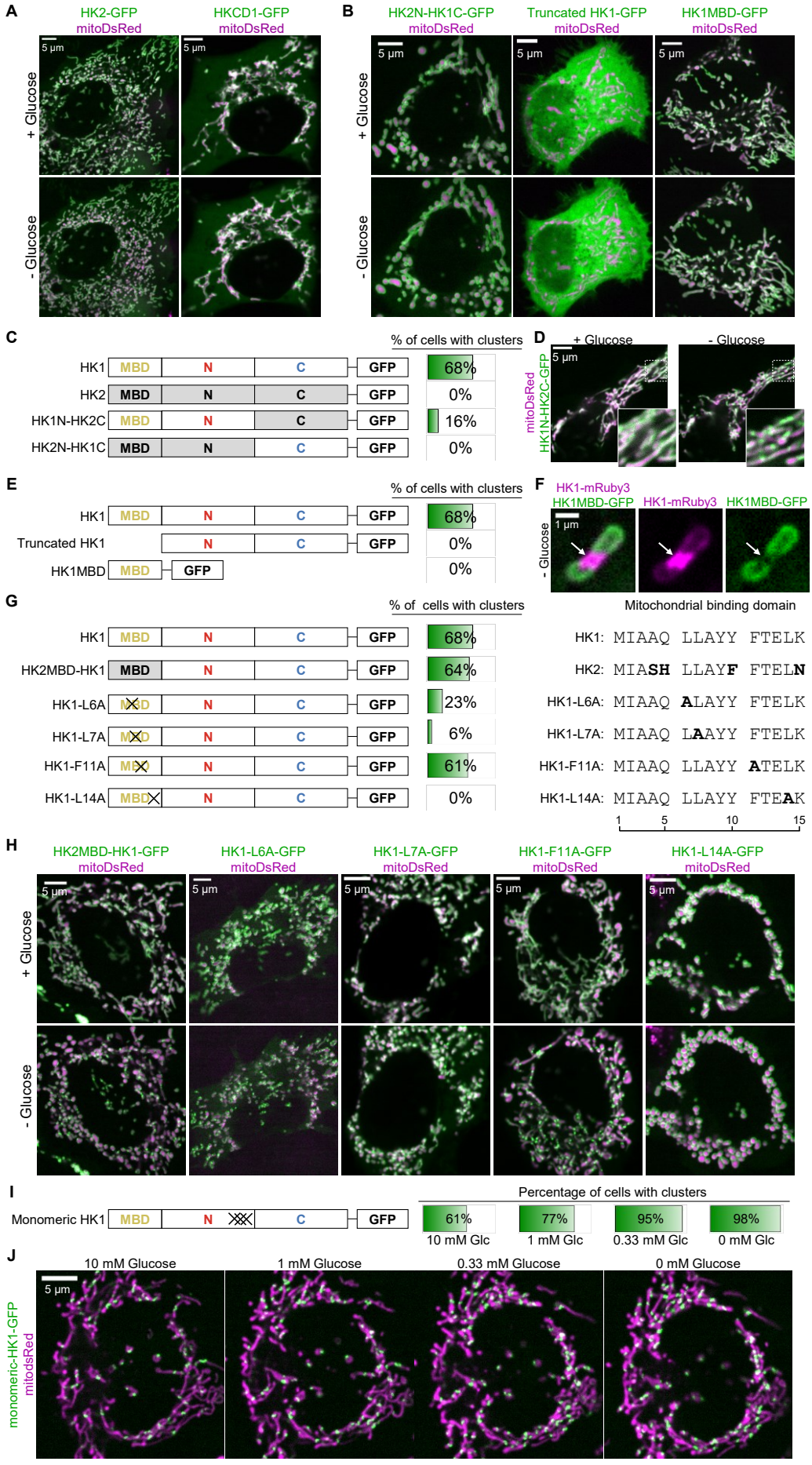
A
HK2-GFP
mitoDsRed
HKCD1-GFP
mitoDsRed
+ Glucose
- Glucose
5 µm
B
HK2N-HK1C-GFP
mitoDsRed
Truncated HK1-GFP
mitoDsRed
HK1MBD-GFP
mitoDsRed
C
% of cells with clusters
HK1 MBD N C GFP 68%
HK2 MBD N C GFP 0%
HK1N-HK2C MBD N C GFP 16%
HK2N-HK1C MBD N C GFP 0%
D
+ Glucose
- Glucose
mitoDsRed
HK1N-HK2C-GFP
E
% of cells with clusters
HK1 MBD N C GFP 68%
Truncated HK1 N C GFP 0%
HK1MBD MBD GFP 0%
F
HK1-mRuby3
HK1MBD-GFP
HK1-mRuby3
HK1MBD-GFP
1 µm
- Glucose
G
% of cells with clusters
HK1 MBD N C GFP 68%
HK2MBD-HK1 MBD N C GFP 64%
HK1-L6A N C GFP 23%
HK1-L7A N C GFP 6%
HK1-F11A N C GFP 61%
HK1-L14A N C GFP 0%
Mitochondrial binding domain
HK1: MIAAQ LLAYY FTELK
HK2: MIASH LLAYF FTELN
HK1-L6A: MIAAQ ALAYY FTELK
HK1-L7A: MIAAQ LAAYY FTELK
HK1-F11A: MIAAQ LLAYY ATELK
HK1-L14A: MIAAQ LLAYY FTEAK
1 5 10 15
H
HK2MBD-HK1-GFP
mitoDsRed
HK1-L6A-GFP
mitoDsRed
HK1-L7A-GFP
mitoDsRed
HK1-F11A-GFP
mitoDsRed
HK1-L14A-GFP
mitoDsRed
+ Glucose
- Glucose
I
Monomeric HK1 MBD N C GFP
Percentage of cells with clusters
61% 10 mM Glc
77% 1 mM Glc
95% 0.33 mM Glc
98% 0 mM Glc
J
10 mM Glucose
1 mM Glucose
0.33 mM Glucose
0 mM Glucose
monomeric-HK1-GFP
mitodsRed

Figure 12. Sructural features dictate the formation of HK1-clusters. (**A**) HK2 does not form clusters, and HKCD1 has a moderate ability to form clusters when glucose is depleted. Confocal images of HeLa cells expressing mitoDsRed and HK2-GFP (left) or HKCD1-GFP (right) with 10 mM glucose (top) and after 10 min of glucose depletion (bottom).[184] (**B**) HK2N-HK1C, truncated HK1, and HK1MBD do not form clusters when glucose is depleted. Confocal images of HeLa cells expressing mitoDsRed and HK2N-HK1C-GFP (left), truncated HK1-GFP (middle), or HK1MBD-GFP (right) with 10 mM glucose (top) and after 10 min of glucose depletion (bottom). MBD, mitochondrial binding domain; N, N-terminal half; C-terminal half.[184] (**C**) The N-terminal half of HK1 is essential for the formation of HK1-clusters. Domain organization of HK1, HK2, and chimera constructs are shown on the left next to the percentages of HeLa cells with clusters after 10 min of glucose depletion. HK1 (n = 110), HK2 (n = 57), HK1N-HK2C (n = 81), HK2N-HK1C (n = 40). MBD, mitochondrial binding domain; N, N-terminal half; C-terminal half.[184] (**D**) The C-terminal half of HK1 is not essential but supports cluster formation. Confocal images of a HeLa cell expressing HK1N-HK2C-GFP and mitoDsRed with 10 mM glucose (left) and after 10 min of glucose depletion (right). Dashed squares in the overview images are magnified in the bottom right corner.[184] (**E**) The MBD is necessary for the formation of HK1-clusters. Domain organization of HK1, truncated HK1, and HK1MBD are shown on the left next to the percentages of HeLa cells with clusters after 10 min of glucose depletion. HK1 (n = 110), truncated HK1 (n = 10), HK1MBD (n = 97). MBD, mitochondrial binding domain; N, N-terminal half; C, C-terminal half.[184] (**F**) HK1MBD-GFP was absent at HK1-rings. Confocal images of a HeLa cell expressing HK1MBD-GFP and HK1-mRuby3 after 20 min of glucose depletion. Arrow indicates the position of an HK1-ring.[184] (**G**) Leucine residues within the MBD are crucial for the formation of HK1-clusters. Domain organization of HK1, HK2MBD-HK1, and mutants in the MBD are shown on the left next to the percentages of HeLa cells with clusters after 10 min of glucose depletion. HK1 (n = 110), HK2MBD-HK1 (n = 33), HK1-L6A (n = 31), HK1-L7A (n = 33), HK1-F11A (n = 28), HK1-L14A (n = 26). Residues in the MBD of constructs that differ from HK1 are highlighted in bold (right). MBD, mitochondrial binding domain; N, N-terminal half; C, C-terminal half. Crosses indicate mutated positions.[184] (**H**) Leucine residues within the MBD are crucial for the formation of HK1-clusters. Confocal images of HeLa cells expressing mitoDsRed and HK2MBD-HK1-GFP, HK1-L6A-GFP, HK1-L7A-GFP, HK1-F11A-GFP, and HK1-L14A-GFP with 10 mM glucose (top) and after 10 min of glucose depletion (bottom).[184] (**I**) Monomeric HK1 forms clusters even in the presence of glucose. Domain organization of monomeric HK1 (E280A, R283A, and G284Y) is shown on the left next to the percentage of HeLa cells with clusters of monomeric HK1 (n = 44) as glucose was gradually depleted in intervals of 7 min. MBD, mitochondrial binding domain; N, N-terminal half; C, C-terminal half. Crosses indicate mutated positions.[184] (**J**) Monomeric HK1 (E280A, R283A, and G284Y) forms clusters even in the presence of glucose. Time-lapse images of a HeLa cell expressing monomeric HK1-GFP and mitoDsRed were acquired at intervals of 7 min as glucose was gradually depleted.[184] [Figure panels reproduced from Pilic *et al.*, 2024.]

To pinpoint which residues in the MBD are crucial for HK1-clustering, we created a chimera construct combining HK1 with the MBD of HK2, resulting in HK2MBD-HK1-GFP. The MBD of HK2 differs from that of HK1 in residues 4, 5, 10, and 15 (Figure 12G)[184]. The clustering behavior of HK2MBD-HK1-GFP was comparable to HK1-GFP (Figure 12G and Figure 12H)[184]. It has been established that altering hydrophobic or charged residues to alanine can compromise the membrane deformation capabilities of proteins.[210,211] Consequently, we created four HK1 constructs with specific alanine substitutions in the MBD: HK1-L6A, HK1-L7A, HK1-F11A, and HK1-L14A. The mitochondrial localization of these mutant constructs was not affected (Figure 12H)[184]. Among the cells expressing these constructs, 61% of those with HK1-F11A-GFP, 23% of those with HK1-L6A-GFP, and only 6% of those with HK1-L7A-GFP were capable of forming HK1-clusters during glucose depletion (Figure 12G and Figure 12H)[184]. Cells expressing HK1-L14A-GFP did not exhibit

HK1-cluster formation upon glucose deprivation (Figure 12G and Figure 12H)[184]. These observations point to the importance of leucine residues in the MBD for the formation of HK1-clusters when cells are under energetic stress.

We then investigated if oligomerization of HK1 influences HK1-clustering. HK1, while monomeric in solution,[212] has been shown to assemble into tetramers upon interaction with the outer mitochondrial membrane.[213,214] The functional role of HK1 in its monomeric state is not fully elucidated. To explore this, we constructed a GFP-tagged version of HK1 with specific mutations (E280A, R283A, and G284Y), which prevents dimerization at the dimer interface.[190] In the majority of cells expressing this monomeric HK1-GFP, HK1-clustering was observed with glucose present and increased further during glucose deprivation (Figure 12I and Figure 12J)[184]. These results suggest that monomeric HK1 supports the formation of HK1-clusters.

3.6 HK1 forms tunnels after prolonged glucose starvation

In cells expressing monomeric-HK1-GFP, we occasionally observed long tunnel-like structures in the presence of glucose (Figure 13 A). These HK1-tunnels were also occasionally observed after culturing cells expressing HK1-GFP in glucose-free culture media overnight (Figure 13B).

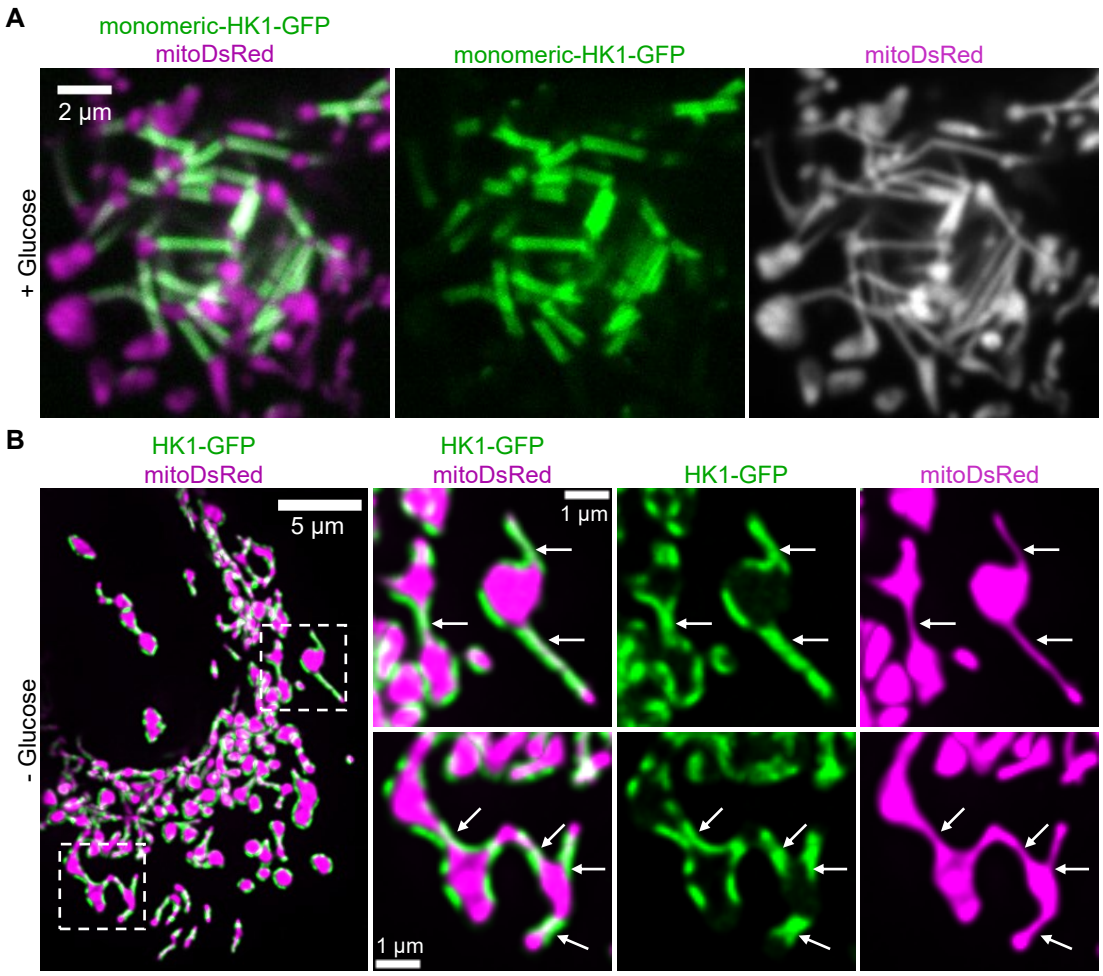

Figure 13. HK1 forms tunnels after prolonged glucose starvation. (**A**) Monomeric HK1 (E280A, R283A, and G284Y) occasionally forms HK1-tunnels in the presence of glucose. Confocal images of a HeLa cell expressing monomeric HK1-GFP and mitoDsRed were acquired in the presence of glucose. (**B**) HK1 forms tunnels after overnight glucose depletion. Confocal images of a HeLa cell expressing HK1-GFP and mitoDsRed were acquired after 16 h of culturing in glucose free medium. Cell was imaged in glucose free storage buffer. Arrows indicate positions of HK1-tunnels.

3.7 Impact of HK1-Rings on Mitochondrial Function and Cellular Metabolism

To elucidate the role of HK1-ring structures, we investigated two specific mutants: HK1-ATPmut, which facilitates ring assembly, and HK1-L14A, which fails to form rings under energy stress. We analyzed the effect of HK1-rings on mitochondrial stability by examining mitochondrial morphology in glucose-deprived HeLa cells expressing either HK1-ATPmut-GFP or HK1-L14A-GFP during FCCP-induced stress. FCCP exposure led to pronounced mitochondrial fragmentation in HeLa cells expressing HK1-L14A-GFP (Figure 14A, upper panel)[184], while cells with HK1-ATPmut-GFP maintained mitochondrial integrity (Figure 14A, lower panel)[184]. This suggests that specific mutations in HK1 affect mitochondrial morphology during stress conditions.

To explore how HK1-rings affect cellular metabolism, we conducted untargeted NMR metabolomics on HeLa cells deprived of glucose. We performed sparse partial least squares-discriminant analysis (sPLS-DA) to differentiate between non-transfected control cells and those expressing either HK1-ATPmut or HK1-L14A. The sPLS-DA analysis revealed distinct metabolic profiles among the groups, with clear separation observed in the score plot (Figure 14B, left), with specific metabolite changes highlighted (Figure 14B, right and Figure 14C). Both HK1 mutants resulted in elevated lactate levels compared to non-transfected controls (Figure 14D), indicating enhanced lactate production. HK1-ATPmut expressing cells exhibited a distinct metabolic shift, characterized by lower glutamine and higher fumarate levels compared to both the control group and cells expressing HK1-L14A (Figure 14D). This suggests that HK1-rings are involved in altering metabolic processes related to glutaminolysis and the TCA cycle (Figure 14E).

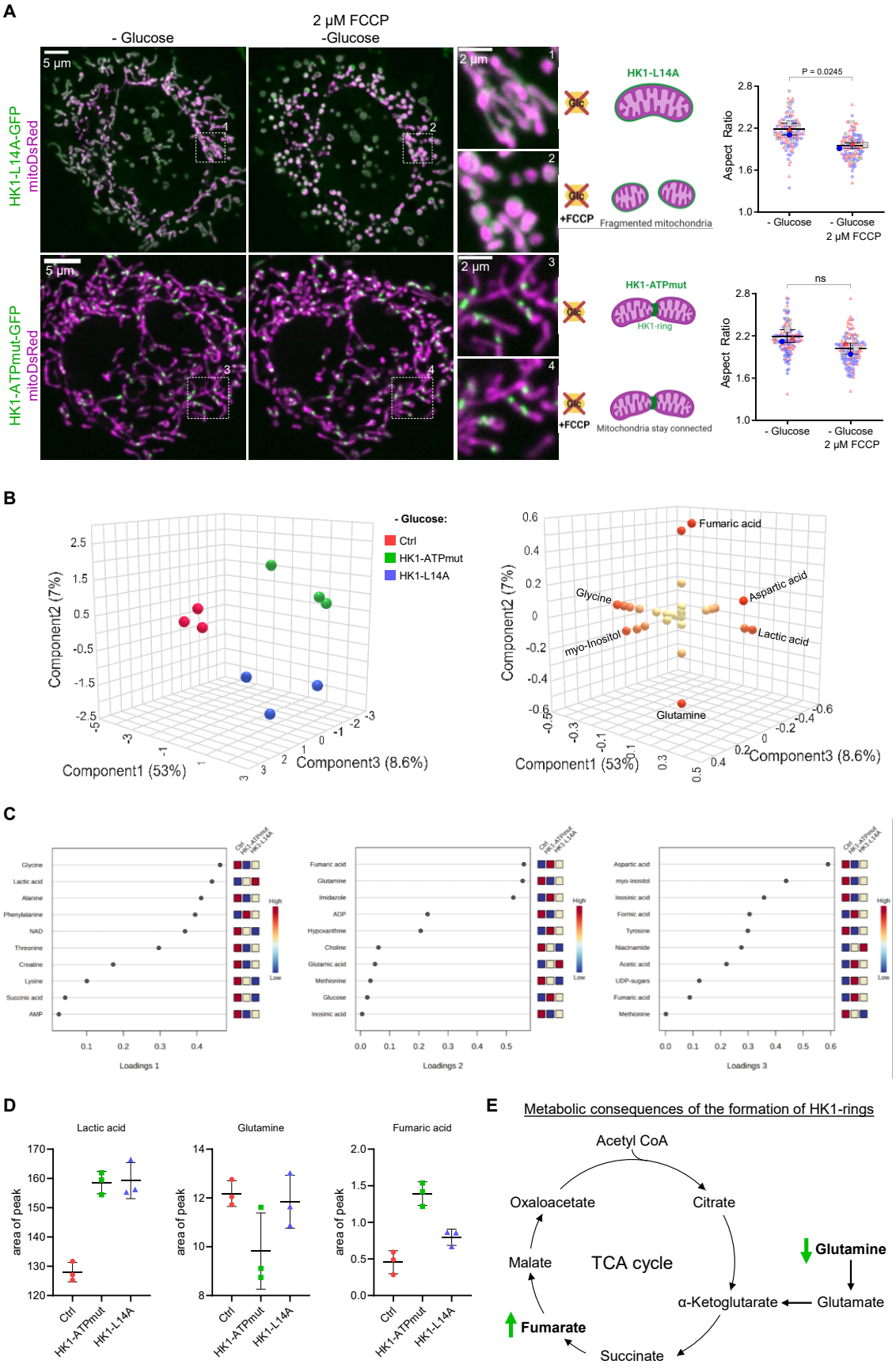

Figure 14. HK1 mutants affect mitochondrial dynamics and metabolism. (**A**) Single point mutations in HK1 alter mitochondrial dynamics during energy stress. Confocal images of HeLa cells

expressing mitoDsRed with HK1-L14A-GFP (top panel) and HeLa cells that express mitoDsRed with HK1-ATPmut-GFP (bottom panel). Glucose was depleted for 30 min before imaging (leftmost images). The middle images show the cells after perfusion with 2 µM FCCP for 20 min. Numbered dashed squares are magnified on the right side of the overview images. The beeswarm SuperPlot represents each cell with a color-coded dot according to the experimental day (right). Two-tailed paired t-test was used for statistical analysis (n = 3). Data are presented as mean ± SD. [184] (**B**) HK1-rings rewire mitochondrial metabolism. Untargeted NMR metabolomics sPLS-DA 3D score plot (left): Component 1 of 53%, Component 2 of 7%, and Component 3 of 8.6%. 3D loading plot indicates most distinctive metabolites (right). (**C**) Loading plots indicate the most distinctive metabolites. The tables with the listed metabolites show changes in concentration. Heatmaps are shown on the right side. (**D**) Graphs show changes in the area of peaks of selected metabolites. (**E**) Proposed model for mitochondrial rewiring by HK1-rings. Green arrows indicate consequences in metabolite levels by the formation of HK1-rings. [Figure panels reproduced from Pilic *et al*., 2024.]

3.8 Fusion of GFP to the N- or C-terminus of VDAC1 induces aggregation and mislocalization

The interaction between HK1 and VDAC1, which is well-documented, might be involved in the formation of HK1-rings. To investigate this interaction dynamically in live cells, we first evaluated whether VDAC1 could fold correctly when fused to fluorescent proteins with a flexible linker. 3D structural models of GFP-VDAC1 and VDAC1-GFP were created using AlphaFold2 (Figure 15A)[185]. The 3D structures indicated that both constructs folded favorably, suggesting that FP fusion does not disrupt the quaternary structure of VDAC1.

To ensure accurate localization of these constructs, we examined HeLa cells transfected with GFP-VDAC1 or VDAC1-GFP and used Mitotracker Red, which labels the inner mitochondrial membrane. We found that both constructs were mostly aggregated in the cytosol (Figure 15B and Figure 15E)[185] or were localized to the cytosol without aggregation (Figure S15D and Figure S15G)[185]. When using less plasmid DNA to minimize potential overexpression artifacts, we observed a decreased percentage of cells with aggregated FP-tagged VDAC1 (Figure 15C and Figure 15F)[185]. However, we did not detect mitochondrial localization (Figure S15D and Figure S15G)[185].

Immunoblot analysis confirmed that FP-tagged VDAC1 is mildly overexpressed compared to the transfection control (Figure S15H)[185]. The results indicate that fusing fluorescent proteins to the N- or C-termini of VDAC1 causes mislocalization and aggregation in HeLa cells, which aligns with earlier studies showing improper targeting of C-terminal FP-tagged VDAC1 in both rat and human cells.[177,178]

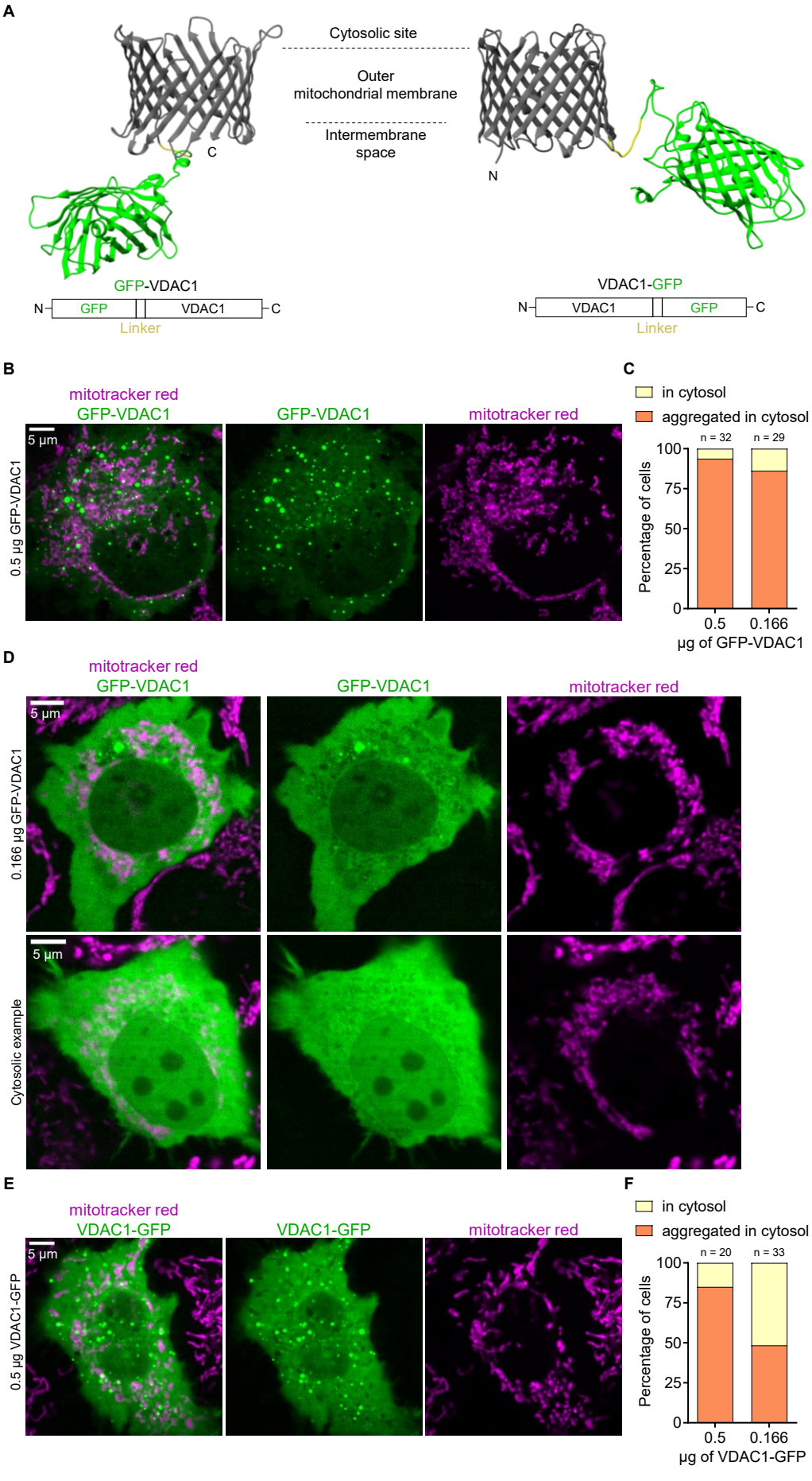
A
Cytosolic site
Outer
mitochondrial membrane
Intermembrane
space
C
N
GFP-VDAC1
N
GFP
VDAC1
C
Linker
VDAC1-GFP
N
VDAC1
GFP
C
Linker
B
mitotracker red
GFP-VDAC1
GFP-VDAC1
mitotracker red
5 µm
0.5 µg GFP-VDAC1
C
in cytosol
aggregated in cytosol
n = 32
n = 29
Percentage of cells
100
75
50
25
0
0.5
0.166
µg of GFP-VDAC1
D
mitotracker red
GFP-VDAC1
GFP-VDAC1
mitotracker red
5 µm
0.166 µg GFP-VDAC1
5 µm
Cytosolic example
E
mitotracker red
VDAC1-GFP
VDAC1-GFP
mitotracker red
5 µm
0.5 µg VDAC1-GFP
F
in cytosol
aggregated in cytosol
n = 20
n = 33
Percentage of cells
100
75
50
25
0
0.5
0.166
µg of VDAC1-GFP

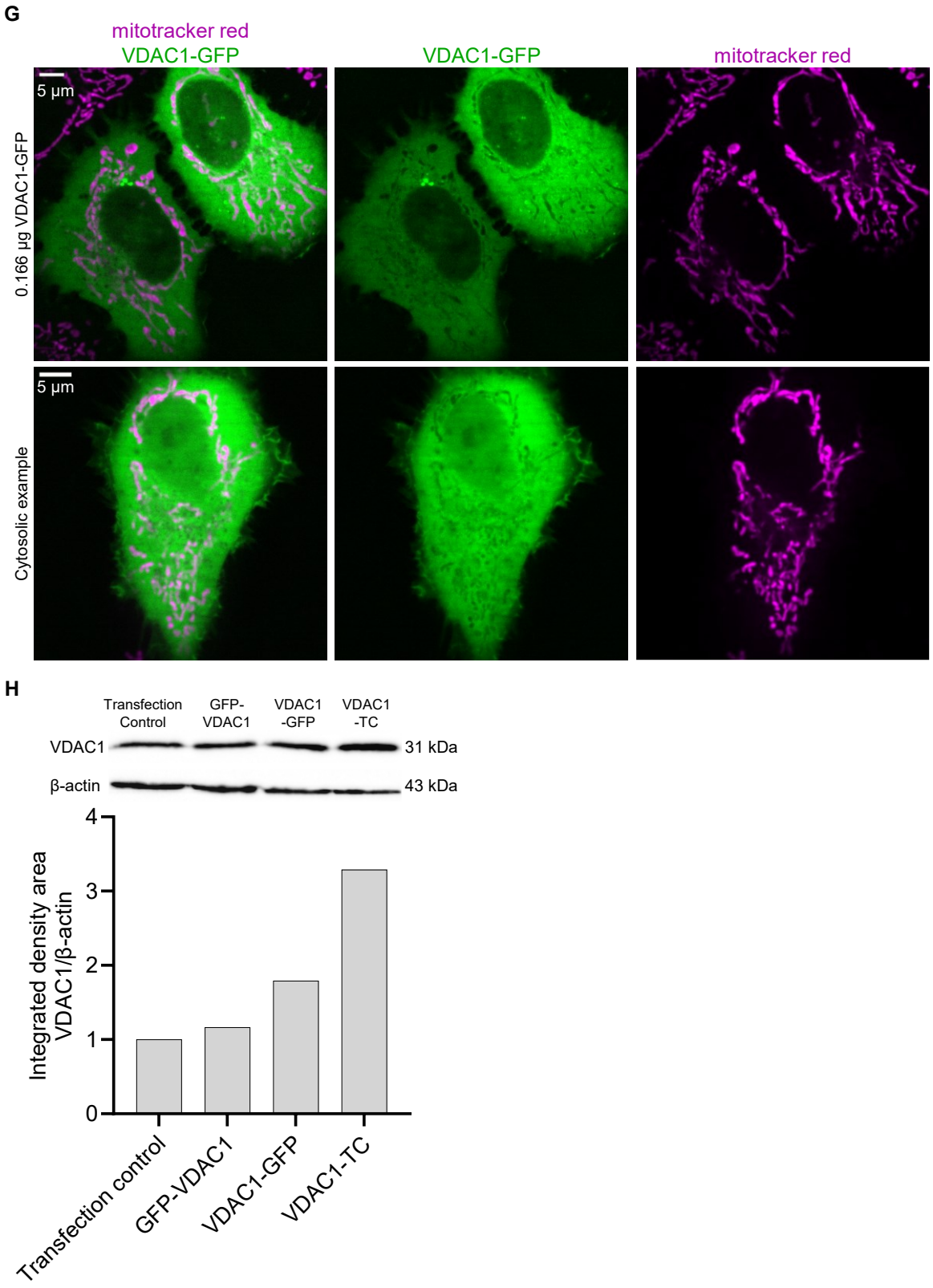

Figure 15. Mistargeting of VDAC1 is induced by N- and C-terminal fusion of GFP. (**A**) AlphaFold2-generated 3D structures and schematic representation of GFP-VDAC1 and VDAC1-GFP fusion constructs. [185] (**B**) Confocal images of a HeLa cell transfected with 0.5 µg of GFP-VDAC1 and stained with mitotracker red. [185] (**C**) Bar graph shows the percentage of HeLa cells with different

expression phenotypes of GFP-VDAC1 using different amounts of plasmid DNA. [185] (**D**) Confocal images of HeLa cells transfected with 0.166 µg of GFP-VDAC1 and stained with mitotracker red. The upper panel shows a HeLa cell where GFP-VDAC1 is aggregated in the cytosol and the lower panel shows a HeLa cell where GFP-VDAC1 is in the cytosol without aggregation. [185] (**E**) Confocal images of a HeLa cell transfected with 0.5 µg of VDAC1-GFP and stained with mitotracker red. [185] (**F**) Bar graph shows the percentage of HeLa cells with different expression phenotypes of VDAC1-GFP using different amounts of plasmid DNA. [185] (**G**) Confocal images of HeLa cells transfected with 0.166 µg of VDAC1-GFP and stained with mitotracker red. The upper panel shows a HeLa cell where VDAC1-GFP is aggregated in the cytosol and the lower panel shows a HeLa cell where VDAC1-GFP is in the cytosol without aggregation. [185] (**H**) Protein extracts from transfection control HeLa cells or HeLa cells transfected with 0.5 µg of GFP-VDAC1, VDAC1-GFP, or VDAC1-TC were analyzed with an immunoblot using specific antibodies for VDAC1 and β-actin. Relative optical densities of the bands were determined, and the results were normalized to β-actin. [185] [Figure panels reproduced from Pilic et al., 2023.]

3.9 The use of a short tetracysteine-tag enables the visualization of VDAC1-clusters on mitochondria.

Given the tendency of VDAC1 to mislocalize with C-terminal tags exceeding eight residues,[179] we attached the six-residue tetracysteine (TC) tag at the C-terminus of VDAC1. We chose the C-terminus for tagging to void interference with the N-terminal domain, which is involved in numerous protein interactions.[215] We used FlAsH-EDT_2 to visualize VDAC1-TC (Figure 16A)[185], and determined the optimal dye concentration by imaging HeLa cells coexpressing VDAC1-TC and mitoDsRed with different amounts of FlAsH. We observed two distinct labeling patterns: cells transfected with VDAC1-TC showed a cluster-like distribution of VDAC1 around mitochondria (Figure 16A, second row)[185]. An increase in green fluorescence intensity was noted with higher FlAsH concentrations, and there was significant noise at lower concentrations (Figure 16A, third row)[185]. Untransfected cells displayed uniform FlAsH labeling of mitochondria, indicating non-specific accumulation of the dye (Figure 16A, fourth row)[185]. Notably, transfecting with mitoDsRed alone we did not observe clusters (Figure 16B)[185], ruling out dye-induced clustering.

To verify that the FlAsH signal in VDAC1-TC-transfected cells corresponds to VDAC1, we conducted immunofluorescence using a VDAC1 antibody (Figure 16C)[185]. We observed clear colocalization between the VDAC1 antibody labeling and the VDAC1-TC FlAsH signal (Line scan analysis in Figure 16C)[185] and a cluster-like distribution of endogenous VDAC1 in wild-type cells (Figure 16D)[185]. This cluster-like pattern of VDAC1 on mitochondria was also observed with FLAG-tagged VDAC1 and endogenously labeled VDAC1.[139,216] Given that FlAsH shares structural

similarities with the mitochondrial dye Rhodamine 123 (Figure 16E)[185], we speculated that FCCP, a mitochondrial uncoupler, might lessen the non-specific binding of FlAsH to mitochondria. Treatment with FCCP during labeling significantly reduced FlAsH binding to mitochondria compared to untreated cells (Figure 16E)[185], suggesting that the non-specific binding of FlAsH is influenced by the mitochondrial membrane potential. While the washing buffer used in TC-labeling, British anti-Lewisite (BAL), also decreased FlAsH binding, it was not as effective as FCCP. (Figure 16 E)[185].

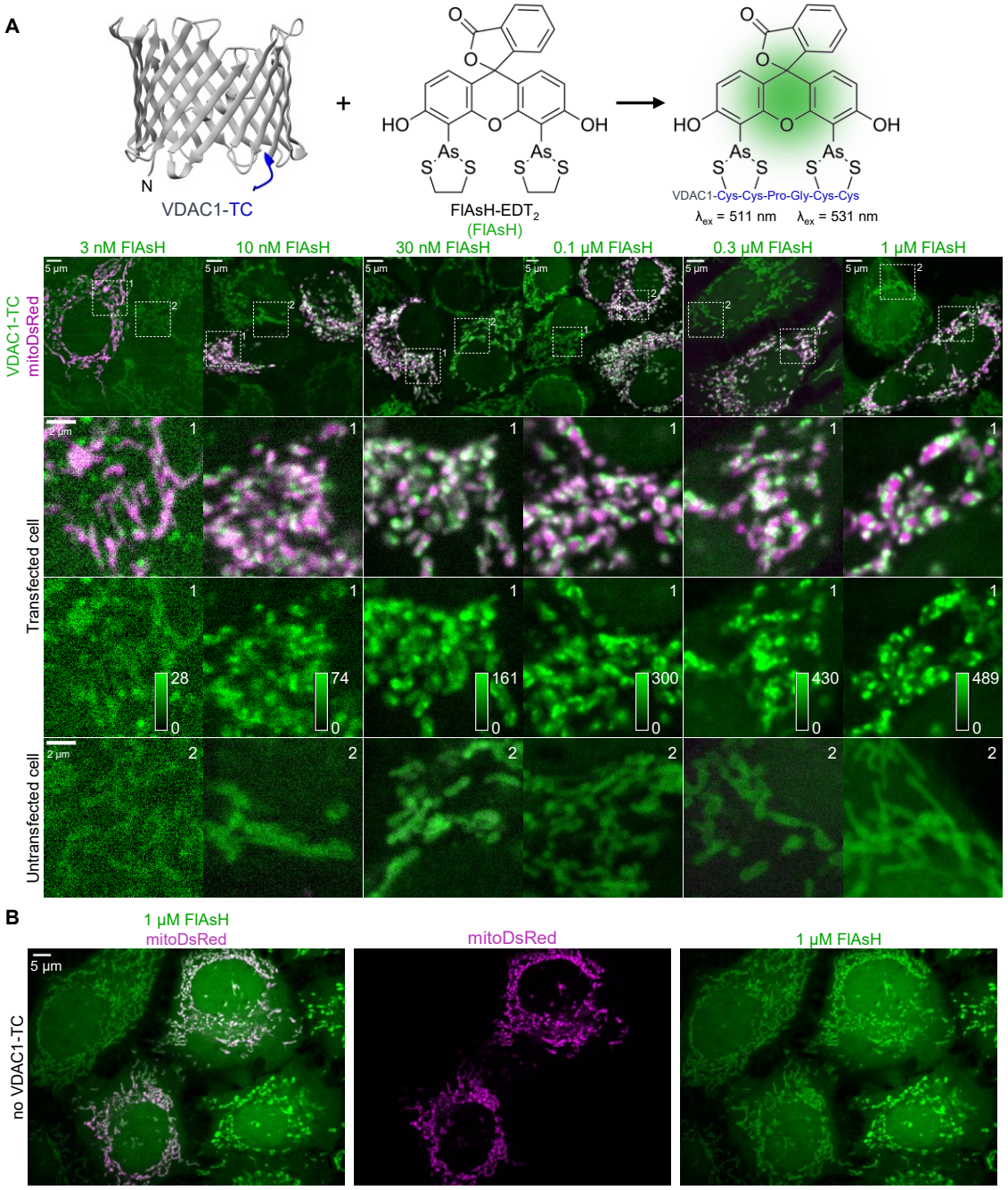

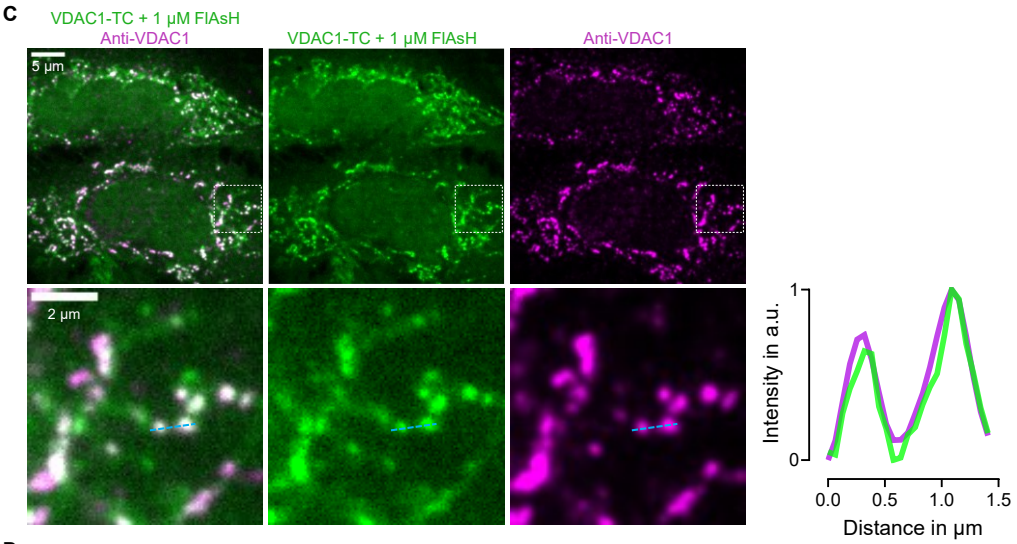
C
VDAC1-TC + 1 µM FlAsH
Anti-VDAC1
VDAC1-TC + 1 µM FlAsH
Anti-VDAC1
5 µm
2 µm
Intensity in a.u.
1
0
0.0
0.5
1.0
1.5
Distance in µm

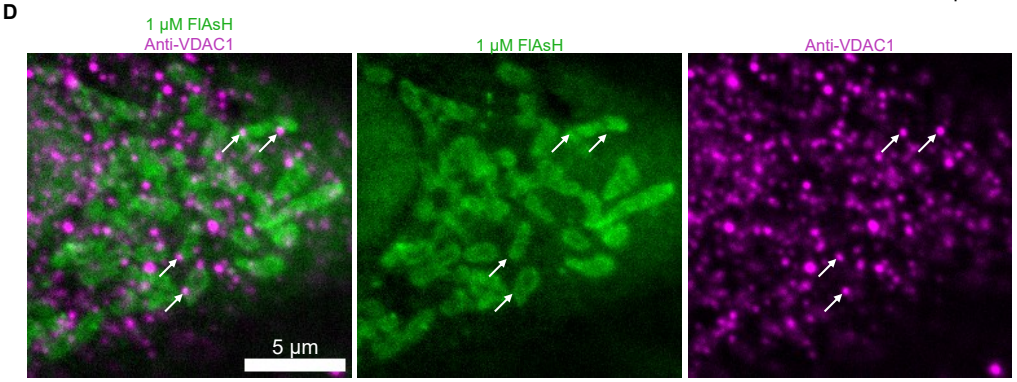
D
1 µM FlAsH
Anti-VDAC1
1 µM FlAsH
Anti-VDAC1
5 µm

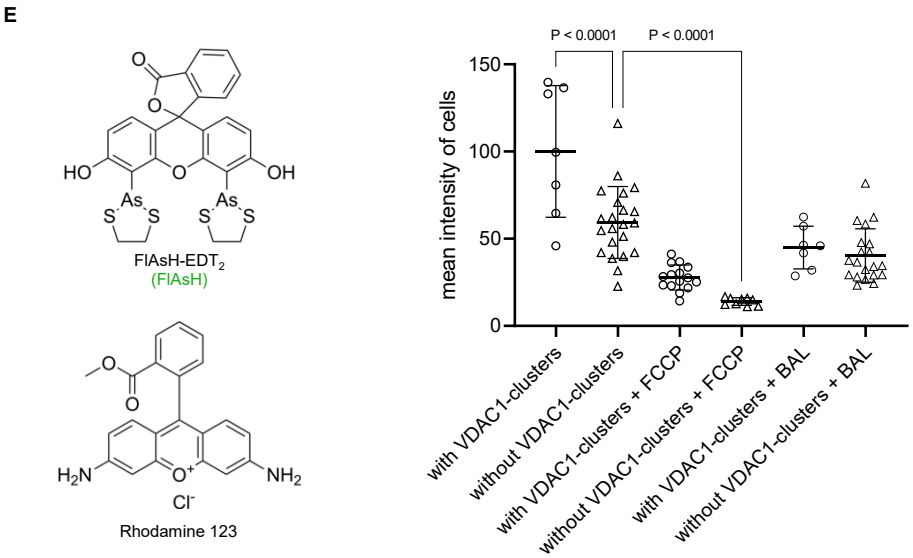
E
FlAsH-EDT2
(FlAsH)
Rhodamine 123
P < 0.0001
P < 0.0001
mean intensity of cells
150
100
50
0
with VDAC1-clusters
without VDAC1-clusters
with VDAC1-clusters + FCCP
without VDAC1-clusters + FCCP
with VDAC1-clusters + BAL
without VDAC1-clusters + BAL

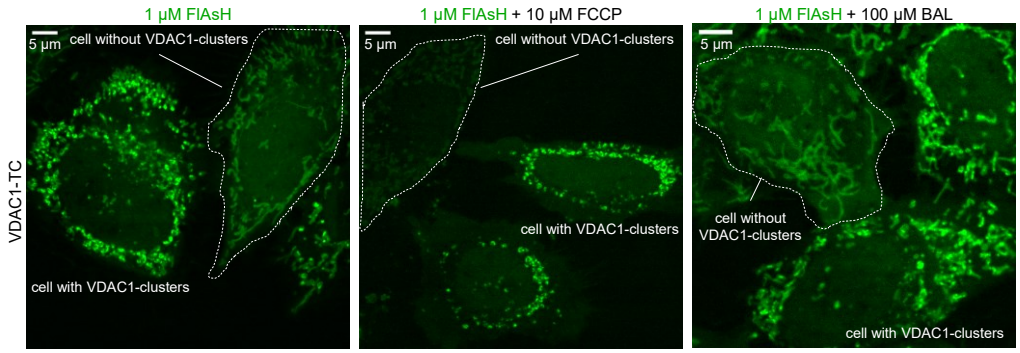
1 µM FlAsH
1 µM FlAsH + 10 µM FCCP
1 µM FlAsH + 100 µM BAL
VDAC1-TC
5 µm
cell without VDAC1-clusters
cell with VDAC1-clusters
cell without VDAC1-clusters
cell with VDAC1-clusters
cell without VDAC1-clusters
cell with VDAC1-clusters

Figure 16. Short tetracysteine-tag allows to visualize VDAC1-clusters on mitochondria. (**A**) 3D structure of VDAC1-TC and chemical structure of FlAsH (top). Confocal images of HeLa cells transfected with VDAC1-TC and mitoDsRed; cells were labeled with FlAsH at increasing concentrations for 30 min (bottom). The first row of images shows an overview of the cells, and the dashed squares are magnified below. In the third row, the intensity levels of FlAsH are depicted in the calibration bar.[185] (**B**) Confocal images of HeLa cells transfected with mitoDsRed; cells were labeled with 1 µM FlAsH for 15 min.[185] (**C**) Immunofluorescence images of HeLa cells expressing VDAC1-TC; cells were labeled with 1 µM FlAsH for 15 min (green) and anti-VDAC1 (magenta). The upper panels show an overview of the cells, and the dashed squares are magnified below. Dashed lines represent the line scan graph on the right and show the relative fluorescence intensity of VDAC1-TC (green) and anti-VDAC1 (magenta) along the length of the line.[185] (**D**) Immunofluorescence images of HeLa cells labeled with 1 µM FlAsH for 15 min (green) and anti-VDAC1 (magenta). Arrows point to VDAC1-clusters at mitochondria. [185] (**E**) Chemical structures of FlAsH and Rhodamine123 (left). Confocal images of HeLa cells transfected with VDAC1-TC; cells were labeled with 1 µM FlAsH for 30 min, in the presence of 10 µM FCCP or washed with 100 µM BAL for 10 min (bottom). The dashed outline indicates cells without VDAC1-clusters. The mean intensity of cells with and without VDAC1-clusters was measured (right graph, n from left to right = 7, 22, 15, 9, 7, and 20). The difference between groups was evaluated using one-way ANOVA with Bonferroni post hoc test. Data are presented as mean ± SD. [185] [Figure panels reproduced from Pilic et al., 2023.]

3.10 Characterizing the effects of FlAsH binding on mitochondrial function

We observed increased mitochondrial fragmentation in cells expressing VDAC1-TC relative to their untransfected counterparts. To investigate this further, we compared the mitochondrial morphology between HeLa cells expressing mitoDsRed alone and those coexpressing both VDAC1-TC and mitoDsRed (Figure 17A)[185]. Aspect Ratio (AR) and Form Factor (FF) were used to evaluate mitochondrial swelling and branching. The data showed a significant decrease in AR and FF, indicating that overexpression of VDAC1-TC leads to mitochondrial fragmentation in HeLa cells (Figure 17A)[185]. Notably, neither FlAsH nor FlAsH combined with BAL had a significant impact on mitochondrial morphology (Figure 17B)[185]. To assess the potential effects of non-specific FlAsH binding on mitochondrial energy status, we measured mitochondrial membrane potential using tetramethylrhodamine methyl ester (TMRM) and evaluated the ratio of oxygen consumption rate (OCR) to extracellular acidification rate (ECAR). We noted variability in TMRM intensity across cells (Figure 17C)[185], but did not observe significant changes in mitochondrial membrane potential (Figure 17C)[185] or OCR/ECAR ratio (Figure 17D)[185] upon labeling cells with FlAsH or washing with BAL.

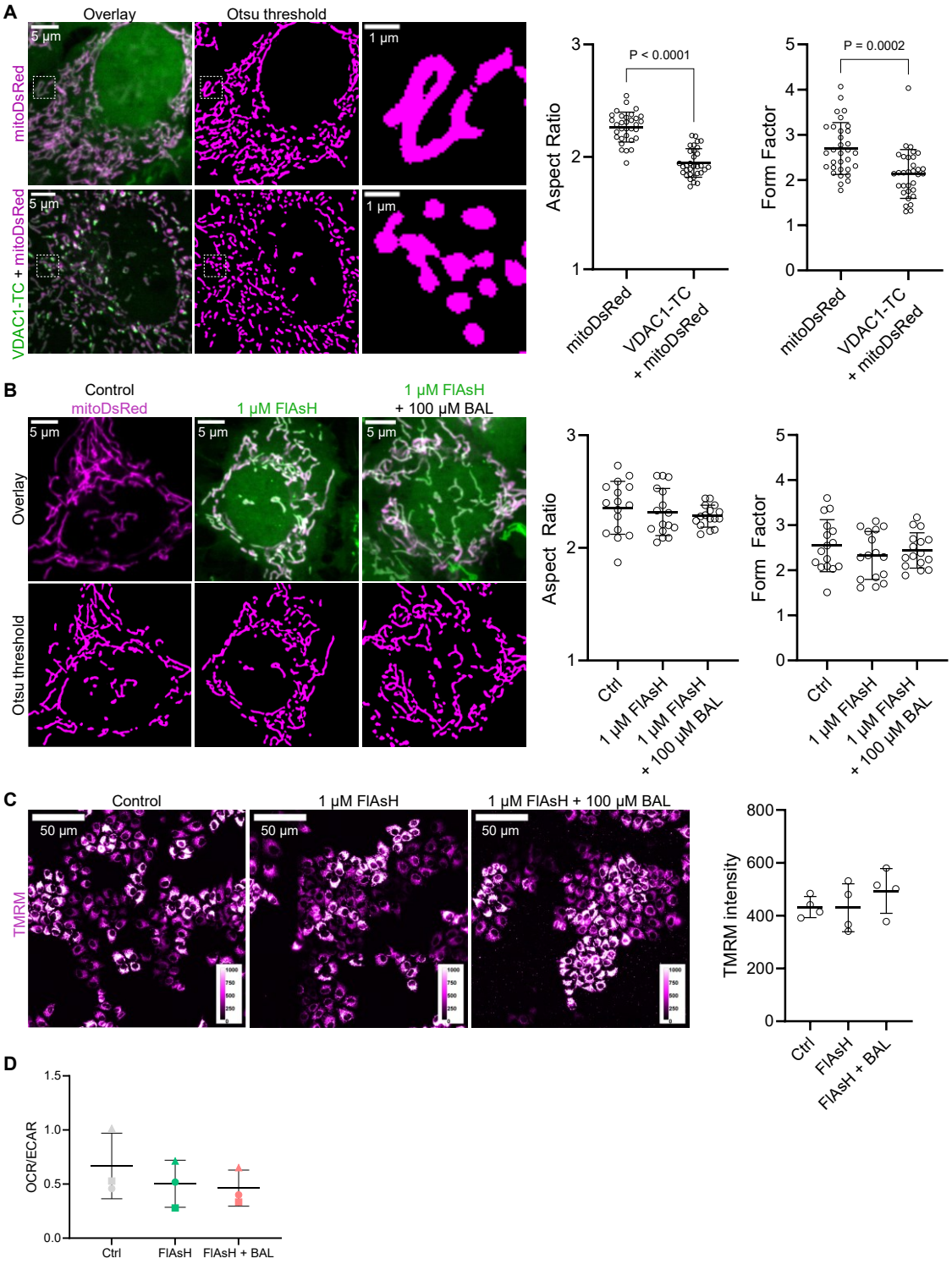

Figure 17. Characterizing the effects of FlAsH binding on mitochondrial function. (**A**) Confocal images of a HeLa cell expressing mitoDsRed (top row) or VDAC1-TC with mitoDsRed (bottom row); cells were labeled with 1 µM FlAsH for 15 min and washed with 100 µM BAL for 10 min. The left column shows an overview of the cell, the middle column shows the Otsu thresholded mitoDsRed signal, and the dashed squares are magnified in the right column. Graphs on the right show the Aspect Ratio and Form Factor of thresholded images (n = 32 per group). The difference between groups was evaluated using unpaired t-test. Data are presented as mean ± SD. [185] (**B**) Confocal images of HeLa cells expressing mitoDsRed; control cells were not labeled (left column); cells were labeled with 1 µM FlAsH for 15 min (middle column) and washed with 100 µM BAL for 10 min (right column). Graphs on the right show the Aspect Ratio and Form Factor of thresholded images (n = 16

per group). The difference between groups was evaluated using unpaired t-test. Data are presented as mean ± SD. [185] (**C**) Confocal images of HeLa cell stained with 25 nM TMRM for 15 min; control cells were not labeled with FlAsH (left image); cells were labeled with 1 µM FlAsH for 15 min (middle image) and washed with 100 µM BAL for 10 min (right image). Graph on the right shows the mean TMRM intensity (control, n = 4/9358 cells; FlAsH n = 4/6375 cells, FlAsH+BAL n = 4/5946 cells). The difference between groups was evaluated using unpaired t-test. Data are presented as mean ± SD. [185] (**D**) Graph shows the ratio between oxygen consumption rate (OCR) and extracellular acidification rate (ECAR) of three groups of HeLa cells: Control cells that were not; cells that were labeled with 1 µM FlAsH for 15 min and cells that were stained with FlAsH and washed with 100 µM BAL for 10 min (n = 3 per group). The difference between groups was evaluated using unpaired t-test. Data are presented as mean ± SD. [185] [Figure panels reproduced from Pilic et al., 2023.]

3.11 HK1 and VDAC1 do not colocalize when glucose is depleted

To determine if overexpression of HK1, which interacts with VDAC1 on the outer mitochondrial membrane,[129] influences the cluster-like distribution of VDAC1, we used HK1-GFP and the red-shifted ReAsH to label VDAC1-TC. Our observations indicated that VDAC1-clusters were localized to the OMM (Figure 18A)[185], suggesting that HK1 overexpression does not alter the subcellular distribution of VDAC1-clusters. Additionally, we investigated whether VDAC1 associates with HK1-rings during glucose depletion but found no significant colocalization between HK1-rings and VDAC1-clusters during this condition (Figure 18B).

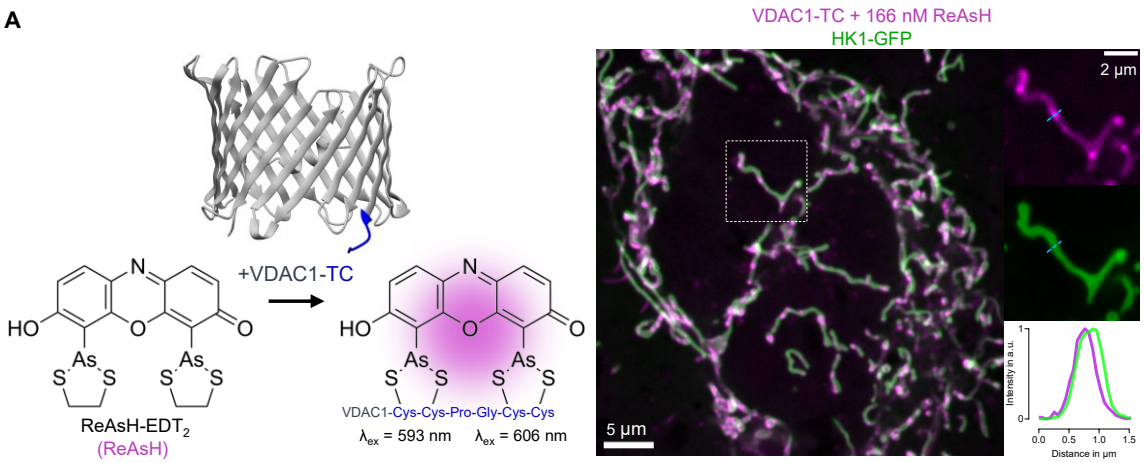

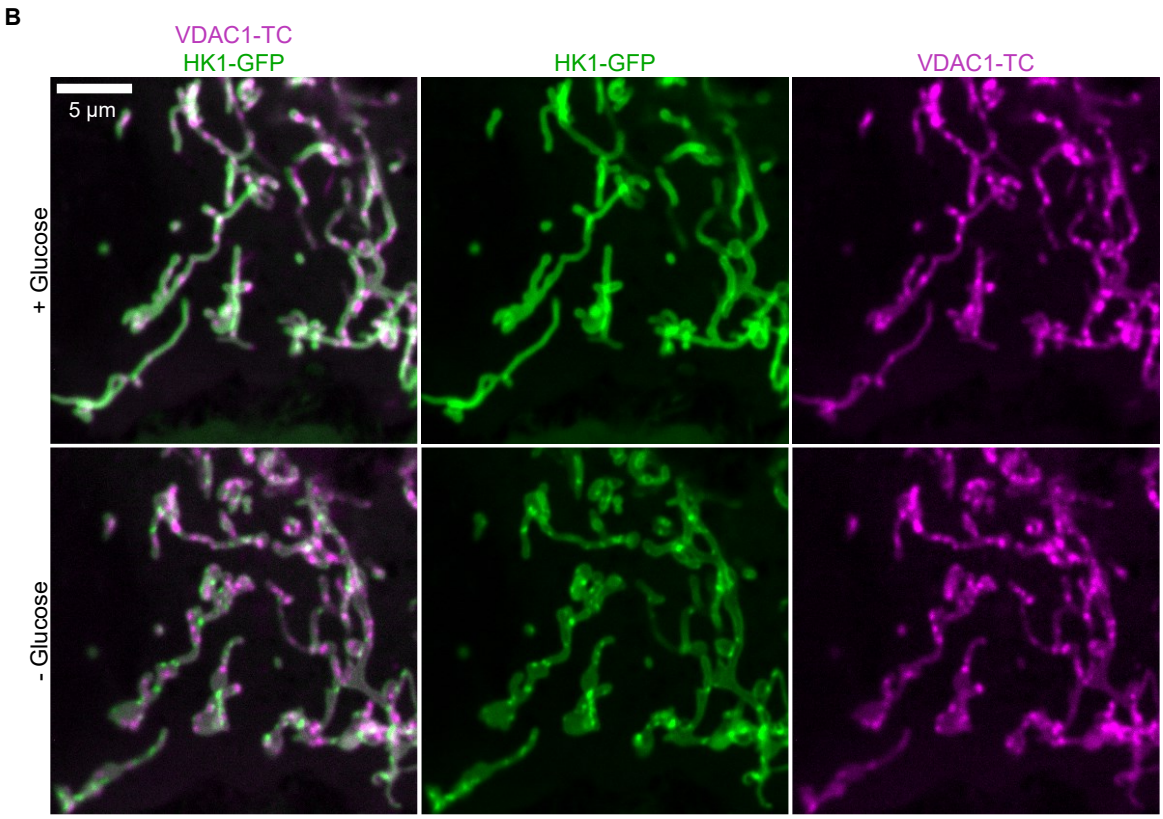

Figure 18. HK1 does not colocalize with VDAC1 during glucose depletion. (**A**) 3D structure of VDAC1-TC and chemical structure of ReAsH (left). Confocal images of a HeLa cell expressing VDAC1-TC and HK1-GFP; cells were labeled with 166 nM ReAsH for 15 min and washed with 100 µM BAL for 10 min (right). Dashed lines represent the line scan graph on the right and show the relative fluorescence intensity of HK1 (green) and VDAC1-TC (magenta) along the length of the line. [185] (**B**) Confocal images of a HeLa cell expressing VDAC1-TC and HK1-GFP; cells were labeled with 166 nM ReAsH for 15 min and washed with 100 µM BAL for 10 min. Top row shows the cell in the presence of glucose and bottom row shows the cell after 20 min of glucose depletion. [185] [Figure panels reproduced from Pilic et al., 2023.]

3.12 VDAC1-clusters are found at the interfaces between the ER and mitochondria.

Given that VDAC1 is known to localize to ER-mitochondrial contact sites,[217,218] we investigated whether VDAC1-clusters overlap with the ER in live cells. For this analysis, we imaged HeLa cells coexpressing VDAC1-TC, the ER marker mCh-ER3, and mitoCFP. Our observations revealed that most VDAC1-clusters are indeed situated at ER-mitochondrial contact sites (Figure 19A)[185]. The majority of VDAC1-clusters colocalize with the ER (Figure 19B)[185]. To further confirm VDAC1 localization at ER-mitochondrial contact sites, we conducted additional colocalization analyses. The Pearson correlation between VDAC1-TC and mCh-ER was significantly reduced when the VDAC1-TC images were rotated by 90 degrees, with consistent changes in Manders' tM1 and tM2 (Figure 19C)[185].

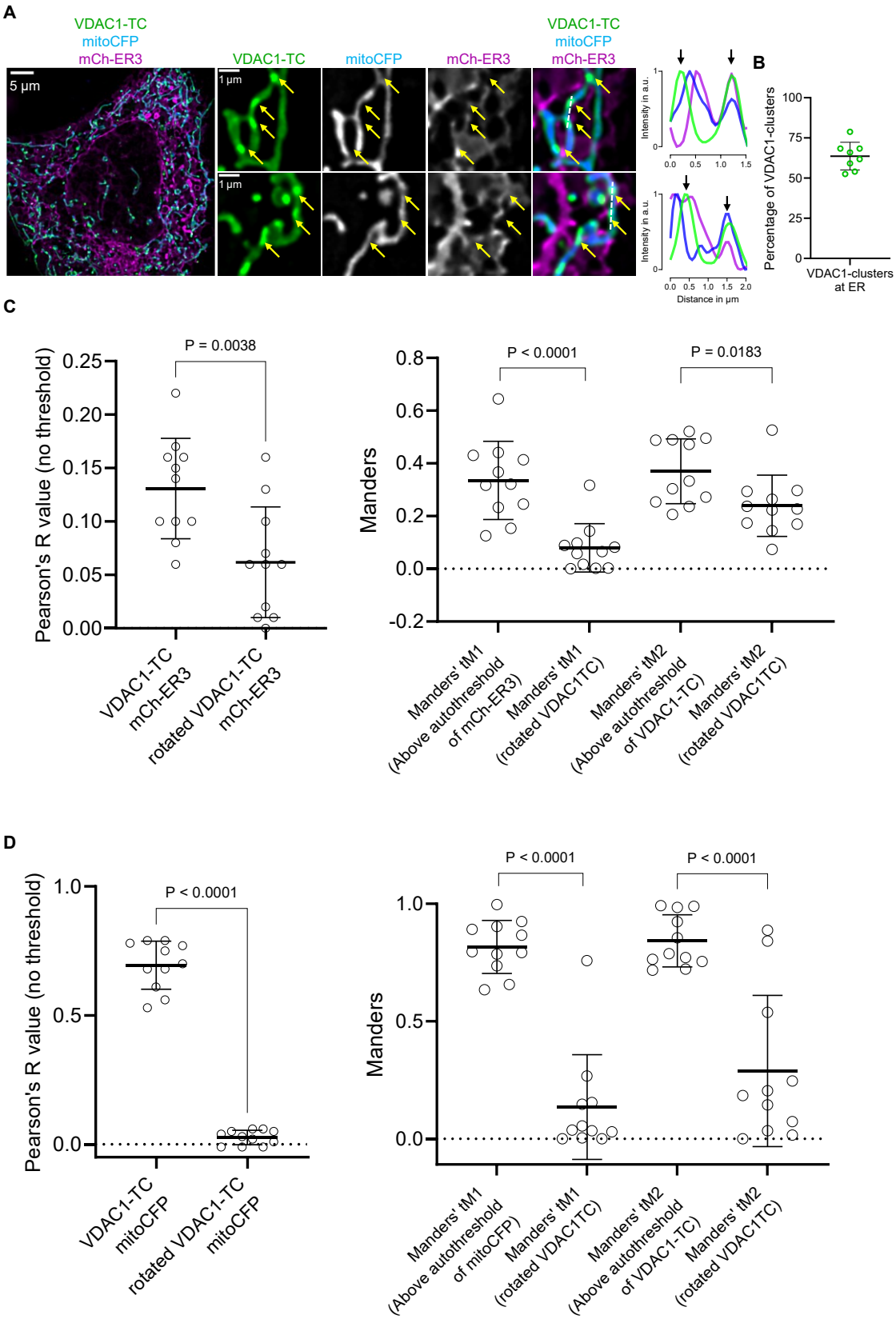
A
VDAC1-TC
mitoCFP
mCh-ER3
5 µm
1 µm
1 µm
Intensity in a.u.
Distance in µm
B
Percentage of VDAC1-clusters
VDAC1-clusters at ER
C
Pearson's R value (no threshold)
P = 0.0038
VDAC1-TC mCh-ER3
rotated VDAC1-TC mCh-ER3
Manders
P < 0.0001
P = 0.0183
Manders' tM1 (Above autothreshold of mCh-ER3)
Manders' tM1 (rotated VDAC1TC)
Manders' tM2 (Above autothreshold of VDAC1-TC)
Manders' tM2 (rotated VDAC1TC)
D
Pearson's R value (no threshold)
P < 0.0001
VDAC1-TC mitoCFP
rotated VDAC1-TC mitoCFP
Manders
P < 0.0001
P < 0.0001
Manders' tM1 (Above autothreshold of mitoCFP)
Manders' tM1 (rotated VDAC1TC)
Manders' tM2 (Above autothreshold of VDAC1-TC)
Manders' tM2 (rotated VDAC1TC)

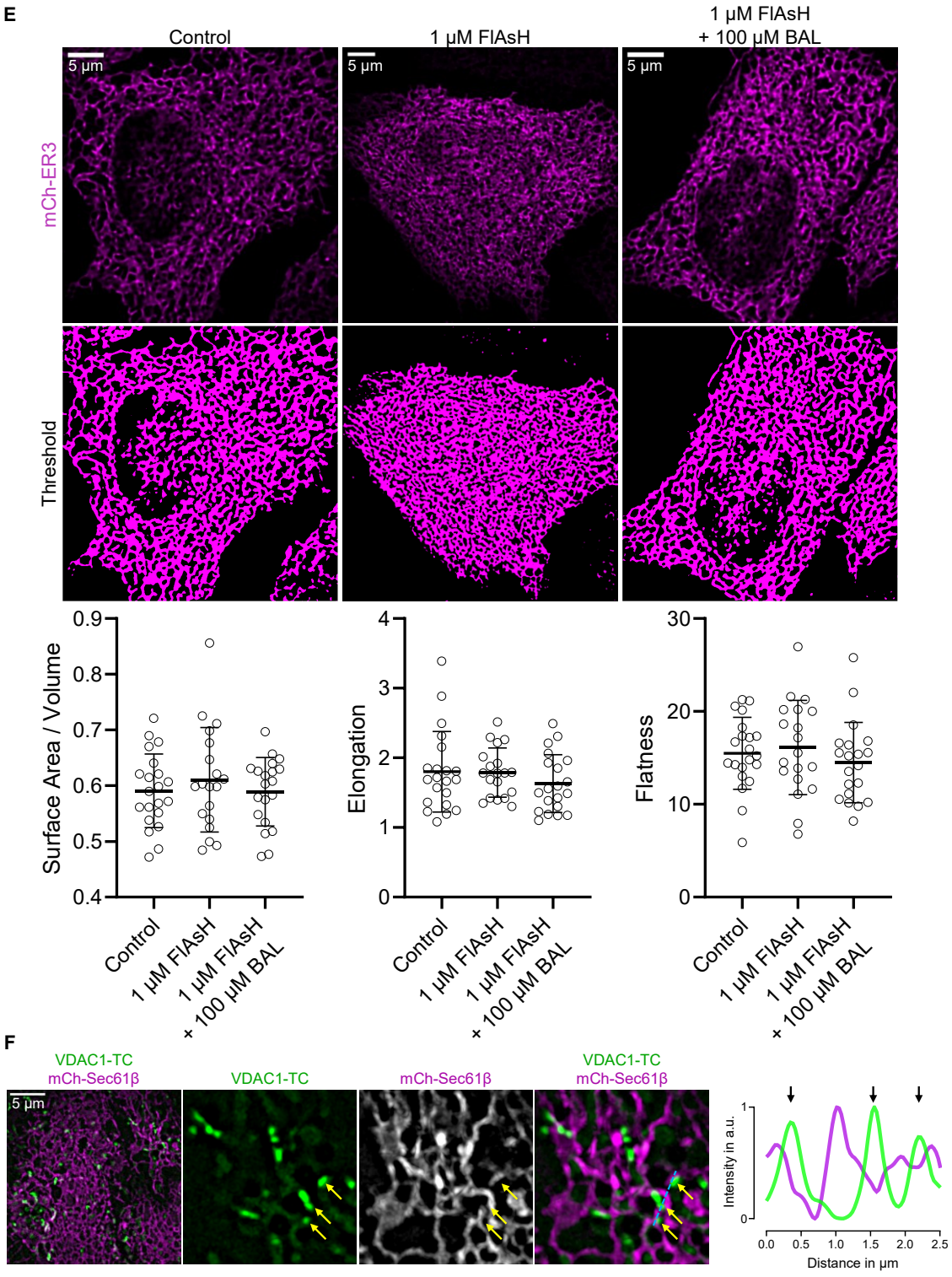

Figure 19. VDAC1-clusters are localized at ER-mitochondria contact sites. (**A**) Confocal images of a HeLa cell expressing VDAC1-TC, mitoCFP, and mCh-ER3; the cell was labeled with 1 µM FlAsH for 15 min and washed with 100 µM Bal for 10 min. The left image shows an overview of the cell, and the dashed squares are magnified on the right side. Yellow arrows point to positions of VDAC1-clusters at ER-mitochondria contact sites. Dashed lines represent the line scan graphs on the right and show the relative fluorescence intensity of VDAC1-TC (green), mitoCFP (blue), and mCh-ER3 (magenta) along the length of the line. [185] (**B**) The graph shows the percentage of VDAC1-clusters that colocalize with the ER (n = 8). [185] (**C**) Graph on the left shows Pearson correlation of VDAC1-TC or 90° rotated VDAC1-TC and mCh-ER3. Graph on the right shows Manders' Colocalization of VDAC1-TC or 90° rotated VDAC1-TC and mCh-ER3. Manders' tM1 represents the ratio of mCh-ER3

colocalized with VDAC1-TC relative to total mCh-ER3, and Manders' tM2 represents the ratio of VDAC1-TC colocalized with mCh-ER3 relative to total VDAC1-TC. The difference between groups was evaluated using unpaired t-test (n = 11). Data are presented as mean ± SD. [185] (**D**) Graph on the left shows the Pearson correlation of VDAC1-TC or 90° rotated VDAC1-TC and mitoCFP. Graph on the right shows Manders' Colocalization of VDAC1-TC or 90° rotated VDAC1-TC and mitoCFP. Manders' tM1 represents the ratio of mitoCFP colocalized with VDAC1-TC relative to total mitoCFP, and Manders' tM2 represents the ratio of VDAC1-TC colocalized with mitoCFP relative to total VDAC1-TC. The difference between groups was evaluated using unpaired t-test (n = 11). Data are presented as mean ± SD. [185] (**E**) Confocal images of HeLa cells expressing mCh-ER3; control cells were not labeled (left column); cells were labeled with 1 µM FlAsH for 15 min (middle column) and washed with 100 µM BAL for 10 min (right column). Graphs show the surface-to-volume ratio, elongation, and flatness of the thresholded ER images (control, n = 21; FlAsH n = 19, FlAsH+BAL n = 20). The difference between groups was evaluated using unpaired t-test. Data are presented as mean ± SD. [185] (**F**) Structured illumination microscopy images of a HeLa cell expressing VDAC1-TC with mCh-Sec61β; cells were labeled with 1 µM FlAsH for 15 min and washed with 100 µM BAL for 10 min. Dashed lines represent the line scan graph on the right and show the relative fluorescence intensity of VDAC1-TC (green) and mCh-Sec61β (magenta) along the length of the line. Arrows point to positions of VDAC1-clusters at ER contact sites. [185] [Figure panels reproduced from Pilic et al., 2023.]

Similarly, we found analogous outcomes for VDAC1-TC and mitoCFP correlations (Figure 19D)[185]. Next, we tested the potential effects of FlAsH and BAL on ER structure. We did not observe significant changes in ER morphology upon labeling with FlAsH or washing with BAL (Figure 19E)[185]. To further substantiate the localization of VDAC1-TC within ER-mitochondria contacts, we used super-resolution microscopy and mCh-Sec61β, an ER membrane marker. We observed high colocalization of VDAC1-TC and mCh-Sec61β (Figure 19F)[185]. Overall, our findings indicate that VDAC1 is situated at the contact points between the ER and mitochondria.

3.13 VDAC1-clusters colocalizes with stress-induced BAK-clusters.

VDAC1 is known to interact with BCL-2 Antagonist/Killer (BAK).[219] To investigate this interaction, we imaged HeLa cells coexpressing VDAC1-TC and GFP-BAK. BAK, a pro-apoptotic protein, typically exists as an inactive monomer on the outer mitochondrial membrane (OMM) but forms clusters and pores in response to cellular stress. We observed that glucose depletion rapidly induced BAK-clustering (Figure 20A)[185]. Our analysis revealed that 39.1% of VDAC1-clusters overlapped with BAK-clusters, and 23.0% of BAK-clusters overlapped with VDAC1-clusters during glucose depletion (Figure 20A)[185]. The Pearson correlation between VDAC1-TC and GFP-BAK decreased significantly when VDAC1-TC images were rotated by 90 degrees, with corresponding changes in Manders' tM1 and tM2 (Figure 20B)[185].

Similar colocalization of BAK with VDAC1 was observed upon treatment with the pro-apoptotic agent staurosporine (Figure 20C)[185] and the ER-stress inducer tunicamycin (Figure 20D) [185]. These findings offer the first evidence of VDAC1-BAK colocalization during cellular stress in live cells.

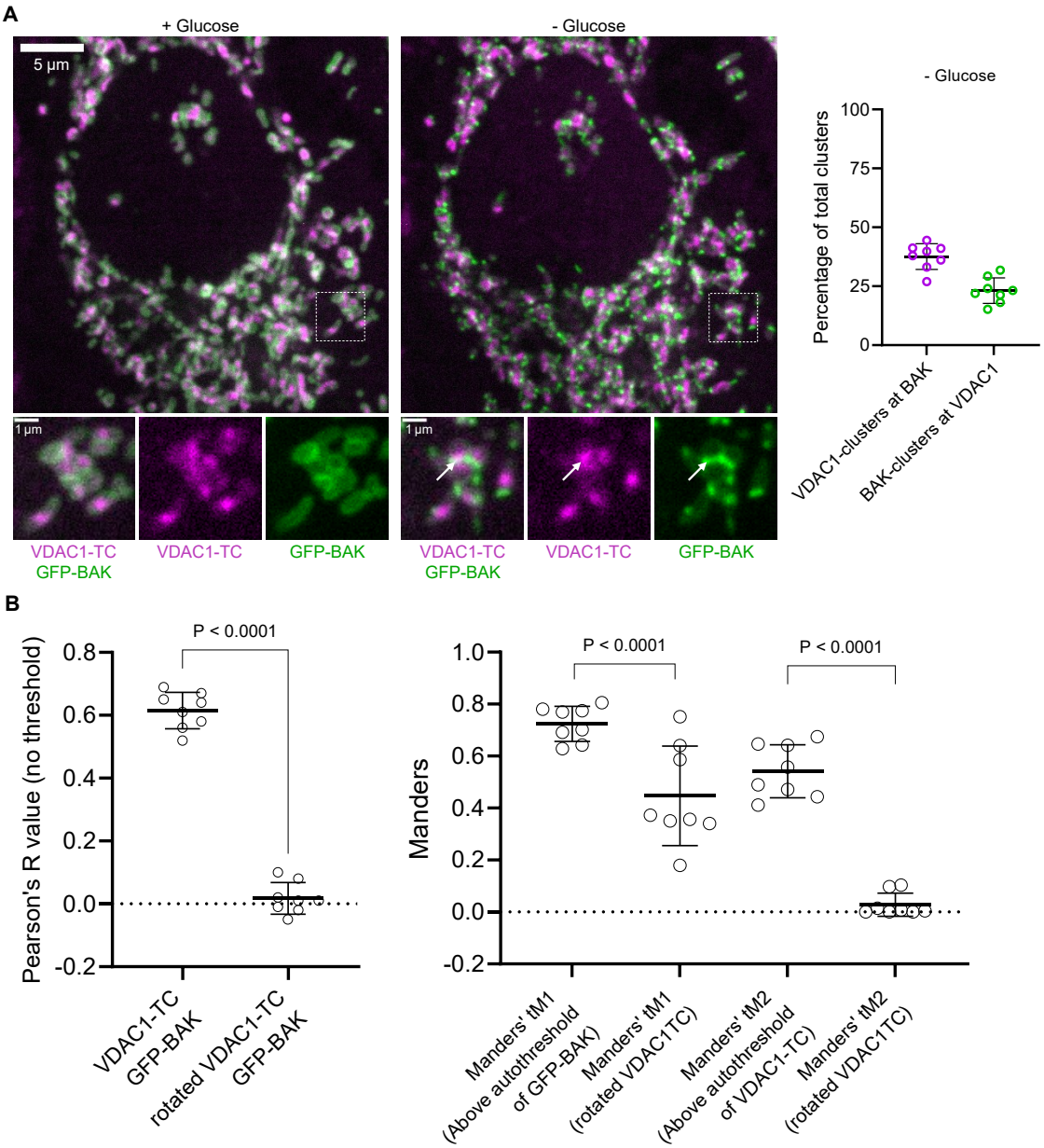

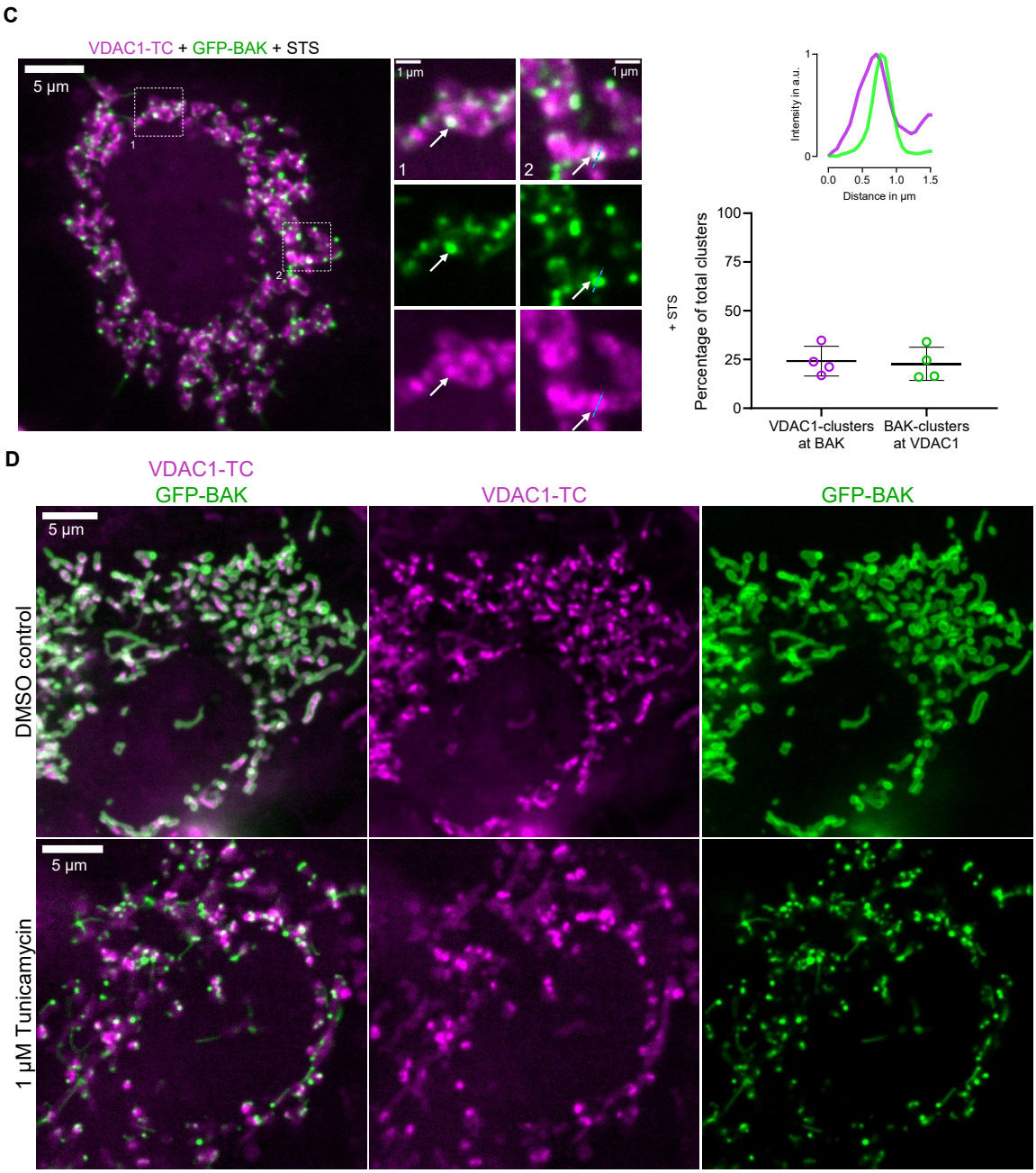

Figure 20. VDAC1 colocalizes with BAK-clusters that form in response to stress. (**A**) Confocal images of a HeLa cell expressing VDAC1-TC and GFP-BAK with 10 mM glucose (left) and after 20 min of glucose depletion (middle); the cell was labeled with 333 nM ReAsH for 15 min. The first row shows an overview of the cell, and the dashed squares are magnified below. White arrows point to the contact site between VDAC1- and BAK-clusters. The graph shows the percentage of VDAC1-clusters that colocalized with BAK-clusters and the percentage of BAK-clusters that colocalized with VDAC1-clusters after 20 min of glucose depletion (right, n = 8 cells). [185] (**B**) Graph on the left shows the Pearson correlation of VDAC1-TC or 90° rotated VDAC1-TC and GFP-BAK. Graph on the right shows Manders' Colocalization of VDAC1-TC or 90° rotated VDAC1-TC and GFP-BAK. Manders' tM1 represents the ratio of GFP-BAK colocalized with VDAC1-TC relative to total GFP-BAK, and Manders' tM2 represents the ratio of VDAC1-TC colocalized with GFP-BAK relative to total VDAC1-TC. The difference between groups was evaluated using unpaired t-test (n = 8). Data are presented as mean ± SD. [185] (**C**) Confocal images of a HeLa cell expressing VDAC1-TC and GFP-BAK after treatment with 10 µM staurosporine for one hour; the cell was labeled with 333 nM ReAsH for 15 min. On the left, an overview of the cell is shown, and the dashed squares are magnified in the middle. White arrows point to the contact sites between VDAC1- and BAK-clusters. Dashed lines represent the line scan graph on the right and show the relative fluorescence intensity of GFP-BAK

(green) and VDAC1-TC (magenta) along the length of the line. The graph shows the percentage of VDAC1-clusters that colocalized with BAK-clusters and the percentage of BAK-clusters that colocalized with VDAC1-clusters after treatment with 10 µM staurosporine for one hour (right, n = 4 cells). [185] (**D**) Confocal images of a HeLa cell expressing VDAC1-TC and GFP-BAK; cells were labeled with 333 nM ReAsH for 15 min. On the top row, a DMSO control cell is shown, and on the bottom row, a cell is shown after treatment with 1 µM tunicamycin for two hours. [185] [Figure panels reproduced from Pilic et al., 2023.]

3.14 VDAC1 is observed at mitochondrial fission sites

Since we observed that VDAC1-TC overexpression induces mitochondrial fragmentation (Figure 17A)[185], we investigated whether VDAC1 plays a role in mitochondrial fission events. Application of FCCP, which strongly promotes mitochondrial fission, revealed that VDAC1-clusters were present at the locations where fission occured (Figure 21A)[185]. To determine if VDAC1 is involved in mitochondrial fission triggered by increased cellular Ca^{2+} levels, we treated cells with ionomycin, a potent Ca^{2+} ionophore. Ionomycin treatment caused ER swelling, indicated by a reduced surface-to-volume ratio and decreased ER flatness (Figure 21C)[185]. Ionomycin caused mitochondria to divide, with VDAC1-clusters positioned at the sites of division (Figure 21B)[185]. This suggests a potential involvement of VDAC1 in mitochondrial fission.

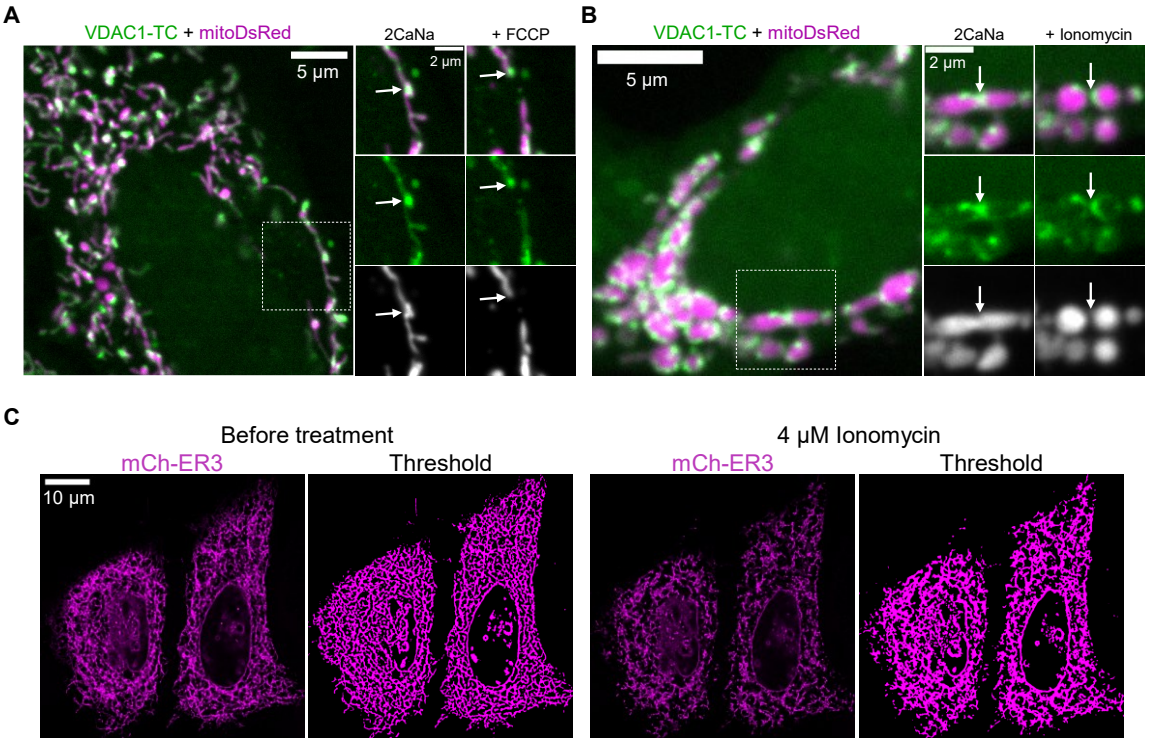

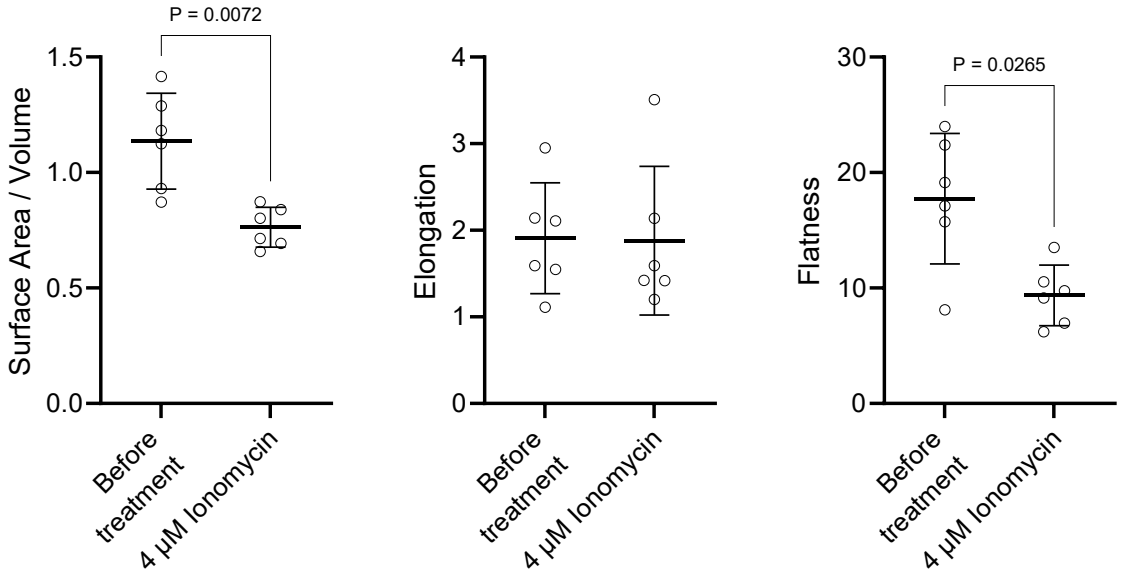

Figure 21. VDAC1 is observed at mitochondrial fission sites. (**A**) Confocal images of a HeLa cell expressing VDAC1-TC and mitoDsRed; the cell was labeled with 1 µM FlAsH for 15 min and washed with 100 µM BAL for 10 min (right). On the left, an overview of the cell is shown, and the dashed square is magnified on the right before (middle) and 10 min after perfusion with 2 µM FCCP. White arrows point to a VDAC1-cluster before and after mitochondrial fission. [185] (**B**) Confocal images of a HeLa cell expressing VDAC1-TC and mitoDsRed; the cell was labeled with 1 µM FlAsH for 15 min and washed with 100 µM BAL for 10 min (right). On the left, an overview of the cell is shown, and the dashed square is magnified on the right before (middle) and 10 min after perfusion with 4 µM Ionomycin. White arrows point to a VDAC1-cluster before and after mitochondrial fission. [185] (**C**) Confocal images of HeLa cells expressing mCh-ER3. ER morphology was assessed before and after treatment with 4 µM Ionomycin for 10 min. Graphs show the surface-to-volume ratio, elongation, and flatness of the thresholded ER images (n = 6). The difference between groups was evaluated using paired t-test. Data are presented as mean ± SD. [185] [Figure panels reproduced from Pilic et al., 2023.]

3.15 HK2 detaches from mitochondria during glucose depletion and 3BP treatment

One goal of my PhD was to identify treatments that affect the binding of HKs to mitochondria. Both glucose depletion and 3-bromopyruvate (3BP) treatment have been described to detach HK2 from mitochondria [80,107,188]. To confirm these reports, we imaged HeLa cells expressing HK2-GFP. Upon glucose removal, HK2 appeared to detach partially from mitochondria (Figure 22A). This detachment was reversed upon glucose readdition (Figure 22A). Treatment with 3BP also leads to a partial detachment of HK2 from mitochondria (Figure 22B). Interestingly, the combination of glucose removal and 3BP treatment strongly detached HK2 from mitochondria, indicated by the stark increase in cytosolic fluorescence brightness (Figure 22C). The synergistic effect of glucose removal and 3BP treatment in detaching HK2 from mitochondria might offer avenues for targeting cancer cell metabolism.

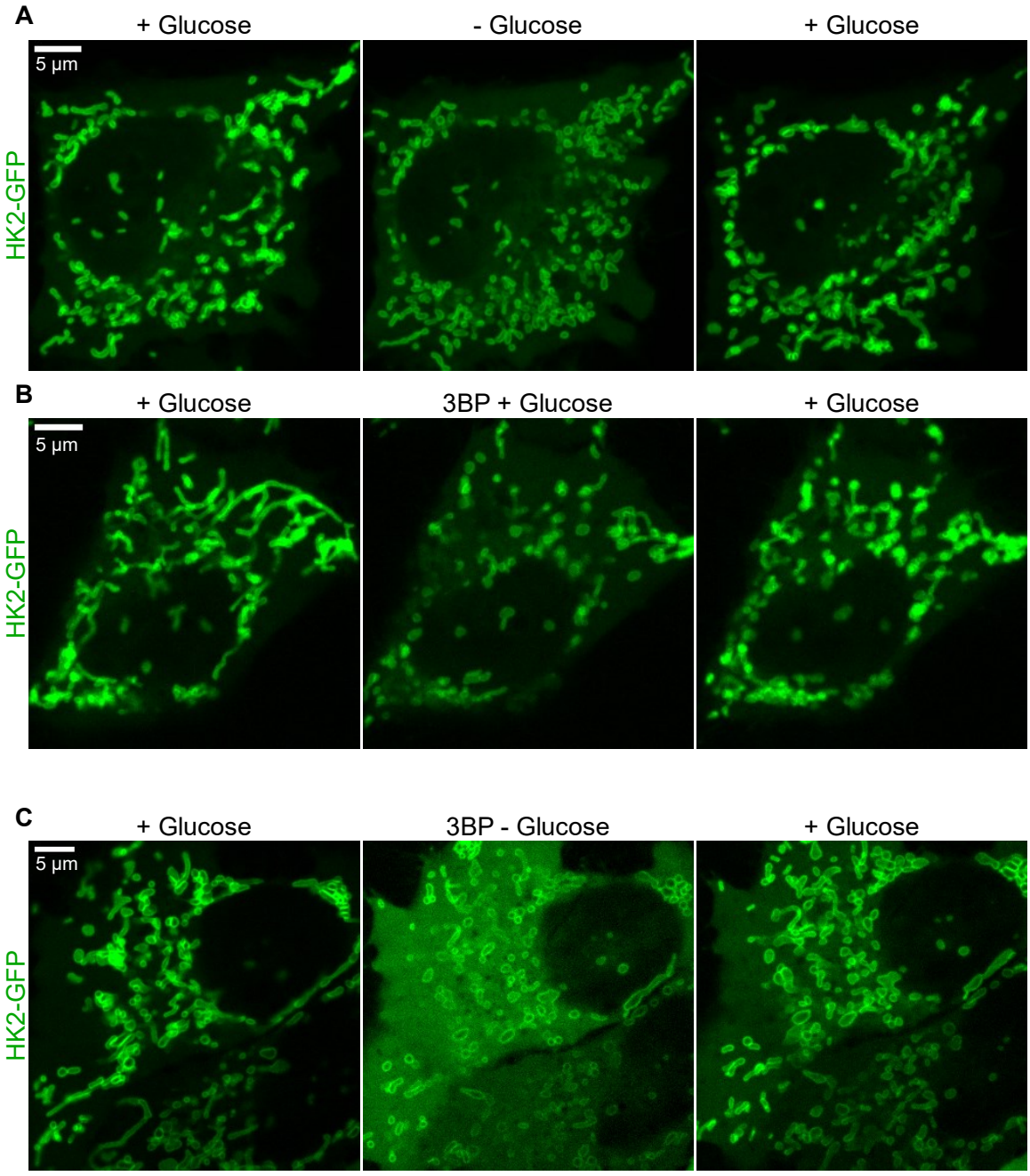

Figure 22. HK2 detaches from mitochondria during glucose depletion and 3BP treatment. (**A**) Confocal images of a HeLa cell expressing HK2-GFP with 10 mM glucose (left), after 30 min of glucose depletion (middle) and after 30 min of glucose readdition (right). (**B**) Confocal images of a HeLa cell expressing HK2-GFP with glucose (left), after 45 min of perfusion with 300 µM 3BP (middle) and after 45 min of wash out (right). (**C**) Confocal images of a HeLa cell expressing HK2-GFP with glucose (left), after 10 min glucose depletion with 3BP (middle) and after 15 min of wash out with glucose (right).

4 Discussion

The findings presented in this thesis shed light on how mitochondrial proteins adapt to metabolic stress and how these adaptations influence mitochondrial function. We identified novel behaviors of HK1, which forms ring-like structures around mitochondria during energy deprivation, regulating mitochondrial dynamics and function. Additionally, we developed a new method to visualize VDAC1 in living cells, revealing its unique distribution and colocalization partners on the surface of mitochondria. These findings improve our understanding of how cells regulate energy stress and maintain mitochondrial function under varying nutrient conditions.

4.1 Mechanism and structural details of the formation of HK1-rings

Building on our observations, we propose a multi-step mechanism for the formation of HK1-clusters (Figure 23)[184]: In summary, the depletion of ATP initiates an open conformation in the C-terminal half, followed by a transition from dimer to monomer and the subsequent oligomerization of monomeric HK1. Our results indicate that the depletion of ATP, rather than glucose, is the pivotal factor that triggers the formation of HK1-clusters. This insight may account for why previous studies under comparable conditions did not observe HK1-clustering. For example, one report found that glucose deprivation did not alter the subcellular distribution of HK1.[80,220] This discrepancy may be explained by the use of cell types capable of maintaining ATP levels during glucose deprivation or by limitations in spatial resolution.[64]

Notably, glucose alone is not able to stabilize the closed conformation of the catalytically active C-terminal domain of HK1.[221] The presence of ATP or G6P is necessary to stabilize this closed conformation.[221] Therefore, we reasoned that an open conformation of the C-terminal half promotes the formation of HK1-clusters. In support of this idea, we observed that a point mutation within the ATP-binding site favors the formation of HK1-clusters. Additionally, we ruled out the possibility that

AMPK mediates the formation of HK1-rings. Moreover, our data suggest that G6P suppresses HK1-clustering, likely by binding to the active site within the C-terminal domain,[197] thereby promoting the closed conformation.[221]

Our findings indicate that monomeric HK1 plays a key role in promoting HK1-clustering. This suggests that the transition from dimer to monomer might be the second critical step in HK1-cluster formation. However, whether this transition is essential for clustering or whether it naturally occurs during the process remains uncertain. Alternatively, it is conceivable that the previously identified dimer interface is distinct from the one implicated in HK1-clustering.[190] We suggest that the final step in HK1-cluster formation involves the oligomerization of monomeric HK1.

Our results also emphasize the importance of the N-terminal half of HK1 in cluster formation. While the N-terminal halves of both HK1 and HK2 exhibit similar structural folds, only the N-terminal half of HK1 is capable of supporting a partially open conformation.[222] This structural feature may explain why the N-terminal half of HK2 cannot substitute for that of HK1. Furthermore, our data imply that leucine residues within the mitochondrial-binding domain (MBD) of HK1 are crucial for HK1-cluster formation. It is noteworthy that mutations within the MBD can prevent HK1-clustering, similar to how mutations in membrane anchors can impede protein oligomerization by disrupting tight packing or the ability to detect membrane curvature.[223,224]

Other structural details, such as posttranslational modifications, could affect the ability of HK1 to form rings. For example, c-Src, a tyrosine kinase that acts as a proto-oncogene, has been shown to promote glycolytic flux by phosphorylating HK1 at Tyr732.[225] This phosphorylation increases the affinity of HK1 with glucose by disrupting the ability of HK1 to form dimers.[225] Considering our evidence that monomeric HK1 promotes HK1-ring formation, we hypothesize that phosphorylation at Tyr732 by c-Src could facilitate the formation of HK1-rings.

In summary, our findings suggest that HK1-clustering occurs exclusively under conditions of extreme cellular energy stress, characterized by ATP and G6P

depletion. Such severe energy stress is known to occur during intense exercise, ischemia, and stroke,[226–228] indicating that HK1-clustering might play a significant role in these pathological conditions.

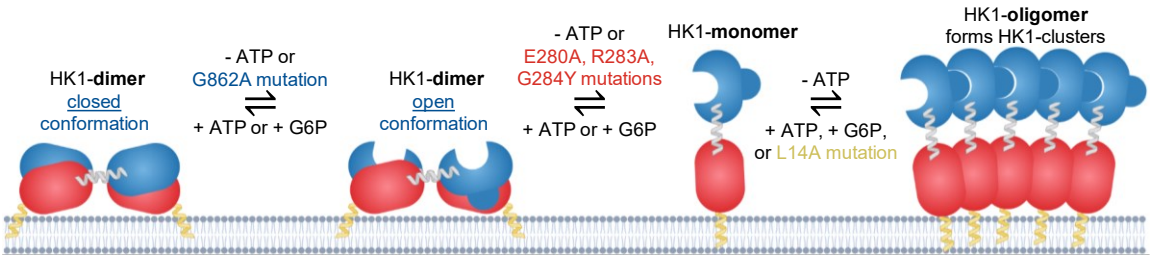

Figure 23. Model of HK1-clustering. The absence of ATP or alterations in the ATP-binding site promotes an open conformation in the C-terminal half (depicted in blue), marking the initial phase of HK1-clustering. Subsequent ATP depletion or mutations affecting the dimer interface trigger a transition from dimeric to monomeric HK1. These monomeric units then polymerize to form new oligomers, which arrange into HK1-clusters. The clustering process can be reversed by mutations in the mitochondrial binding domain or by the reintroduction of ATP or G6P.[184] [Figure reproduced from Pilic *et al*., 2024.]

4.2 Cellular functions of HK1-rings

Our research sheds light on the possible roles of HK1-rings in cellular function. We found that HK1-rings are situated at the ER-mitochondria contact points, which are crucial for several cellular processes including lipid transfer and calcium regulation.[229] Despite these observations, the involvement of HK1-rings in these processes or their impact on ER-mitochondrial communication during energy stress is still not fully understood. The presence of mtDNA at sites of forming HK1-rings suggests that mtDNA may recruit the ER to these locations since mtDNA has been shown to induce ER recruitment in the initial steps of mitochondrial fission.[204] On the other hand, HK1-rings might facilitate the distribution of mtDNA within the mitochondrial network. This distribution of mtDNA could be crucial for maintaining mitochondrial function during energy stress.

Our data indicate that mitochondrial constriction occurs specifically at the sites of HK1-rings, suggesting that these rings might dictate where mitochondrial

constriction takes place under conditions of energy stress. Severe mitochondrial constriction induced by HK1-rings may result in the formation of distinct mitochondrial subcompartments. This constriction likely hinders the diffusion of large molecules within the mitochondrial network. Such subcompartmentalization, driven by HK1-rings, could represent an adaptive response to energy stress.

Although actin is known to influence mitochondrial constriction,[200,201] our findings demonstrate that actin polymerization is not required for the formation of HK1-rings. The structural similarities between HK1 and actin point to a potential evolutionary connection.[230] Previously, it was believed that HK1 had lost its ability to polymerize and generate mechanical force,[39] but our results reveal that HK1 can indeed polymerize into rings that constrict mitochondria.

Additionally, we observed that severe constriction of mitochondria caused by HK1-rings leads to the displacement of cristae membranes. While mitochondrial constriction and decreased cristae density are early markers of mitochondrial fission,[173,200] we did not detect fission at HK1-rings. As illustrated in our model of how energy stress influences the interaction between HK1-rings and players in mitochondrial fission (Figure 24)[184], HK1-rings seem to inhibit mitochondrial fission, even when exposed to chemical uncouplers. This inhibition is likely due to the prevention of Drp1 recruitment to mitochondrial fission receptors by HK1-rings. HK1-rings, with their dense structure, appear to block outer mitochondrial membrane proteins. In locations where HK1-rings disassembled, Drp1-clustering and subsequent mitochondrial fission were observed. Hence, we suggest that HK1-rings prevent mitochondrial fission during energy stress but may facilitate it when cellular energy is restored. The functional benefit of promoting mitochondrial fission after energy restoration remains unclear. However, the inhibition of mitochondrial fission has been linked to reduced apoptosis and decreased mitochondrial degradation,[231,232] and has shown potential in mitigating neurodegenerative conditions like Huntington's disease.[233] Thus, we hypothesize that HK1-rings could provide protective effects by preventing excessive mitochondrial fission in various pathological scenarios, such as ischemia/reperfusion injury and heart failure.[234]

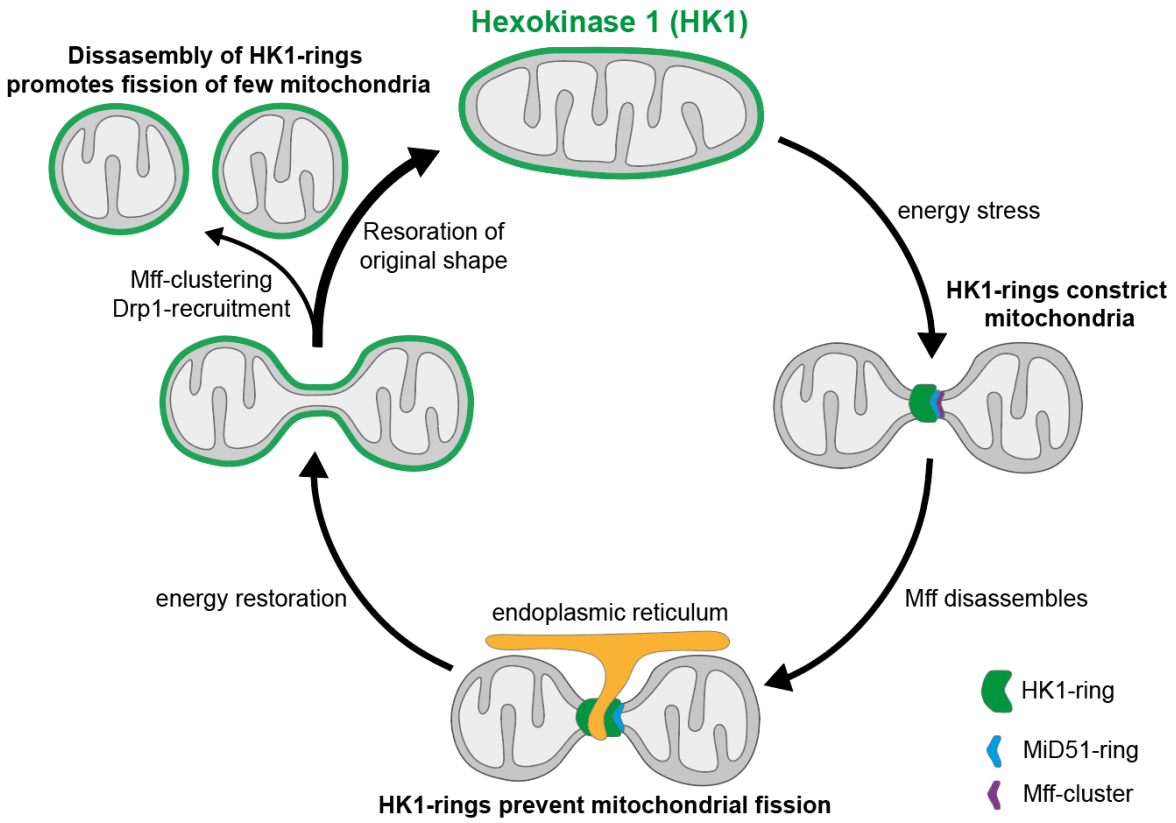

Figure 24. Model of the interplay between HK1 and Drp1-receptors. During energy stress, HK1-rings form at the ER and MiD51-ring sites while Mff-clusters disassemble. HK1-rings inhibit mitochondrial fission during energy stress. Upon energy restoration, HK1-rings disassemble, leading most mitochondria to revert to their original shape, while MiD51-ring disassembly and Mff-cluster reassembly trigger mitochondrial fission in a subset of mitochondria.[184] [Figure reproduced from Pilic *et al*., 2024.]

Our data indicate that HK1-rings can induce substantial constriction without Drp1, revealing a novel mechanism for constriction and suggesting that metabolic enzymes can influence mitochondrial dynamics. Furthermore, our research indicates that HK1-rings might drive a shift in cellular metabolism towards glutaminolysis and enhance TCA cycle activity. This metabolic alteration could be associated with the constriction of mitochondria by HK1-rings, as changes in mitochondrial structure may affect enzyme sensitivity to substrates.[235] Further studies are necessary to clarify how HK1-rings modulate cellular metabolism.

4.3 The connection between mitochondrial morphology and metabolism

One possibility of how HK1-rings could rewire cellular metabolism is by affecting mitochondrial morphology. Changes in mitochondrial shape have been linked to numerous metabolic diseases.[236] The current understanding is that mitochondrial shape affects mitochondrial metabolism, and changes in mitochondrial shape can significantly impact cellular metabolism,[237] but the precise mechanisms of how mitochondrial shape rewires cellular metabolism remains elusive. Typically, a fragmented mitochondrial morphology is associated with an overabundance of nutrients, energy stress, and disturbances in lipid metabolism. Conversely, mitochondria exhibiting an elongated form are often connected with amino acid deficiency and heightened oxidative metabolic activity. In response to these stressors, mitochondria are believed to adapt their shape to optimize their metabolism. Therefore, we reasoned that mitochondrial fragmentation shifts mitochondrial metabolism to increased fatty acid oxidation, whereas mitochondrial elongation shifts mitochondrial metabolism to increased TCA cycle and OXPHOS activity. Identifying the mechanisms of how mitochondrial shape affects mitochondrial metabolism, will contribute to a better understanding of metabolic diseases and potentially lead to the development of new treatments.

We discovered that HK1 forms tunnels during prolonged glucose starvation, leading to severe mitochondrial constriction. A similar mitochondrial phenotype, known as mitochondria on a string (MOAS), has been observed in brain tissue from mice and primates.[238–240] Interestingly, like our findings, MOAS has been associated with altered energetics caused by hypoxia, hypometabolism, and aging.[238–240] Notably, MOAS has also been observed in the brain tissue of Alzheimer's disease patients.[238] It has been suggested that this phenotype represents a mitochondrial fission arrest that prevents mitophagy, thereby affecting mitochondrial quality control[238]. We propose that energy stress may lead to this mitochondrial phenotype

by promoting the formation of HK1-tunnels, which aligns with our observations of mitochondrial changes under conditions of energy stress.

HK1 is the first reported metabolic enzyme forming ring-like structures around mitochondria. However, enzyme filamentation in the context of mitochondria is not entirely new. In the past, there have been reports of enzymes forming filaments inside mitochondria. For example, the mammalian serine beta-lactamase-like protein is located in the mitochondrial intermembrane space, where it forms filaments that regulate the efficiency of metabolic processes.[241] A recent study found that glutaminase forms filaments inside mitochondria during glutamine starvation.[242] Mitochondria with glutaminase filaments were tubulated and protected from mitochondrial degradation,[242] linking mitochondrial morphology to mitochondrial quality control. Our findings and these new reports suggest that enzymes are novel regulators of mitochondrial shape and activity.

4.4 Evaluating the TC-tag to visualize VDAC1 within living cells

We have established that the compact TC-tag is highly effective for observing the dynamics of VDAC1 in living cells. Unlike larger fluorescent proteins, the TC-tag circumvents issues related to bulkiness, making it a valuable tool for investigating the involvement of VDAC1 in cellular activities such as ER-mitochondrial signaling, apoptosis, and mitochondrial dynamics. Our results show that fluorescent protein attachments to both the N- and C-terminal ends of VDAC1 lead to incorrect targeting and aggregation in HeLa cells, which is consistent with prior studies on the inefficacy of C-terminal fluorescent protein-tagged VDAC1 in these cells.[177,178] The TC-tag allowed us to visualize VDAC1-clusters on mitochondria, similar to what has been observed with FLAG-tagged and endogenous VDAC1.[139,216] Fluorescence microscopy revealed that these clusters are positioned at ER-mitochondrial contact sites, aligning with earlier research on VDAC1 localization at these sites,[217,218] and confirming that TC-tagged VDAC1 mirrors the pattern of endogenous VDAC1.

We notably discovered frequent colocalization of VDAC1-clusters and BAK-clusters during glucose deprivation or staurosporine-induced apoptosis. While the involvement of VDAC1 in BAK-mediated apoptosis has been suggested,[219] this is the first evidence of their colocalization. Additionally, VDAC1 was detected at mitochondrial fission sites during treatment with FCCP or ionomycin, suggesting its involvement in mitochondrial fission events. Overexpression of VDAC1 led to significant mitochondrial fragmentation, aligning with previous findings that VDAC1 knockdown prevents glutamate excitotoxicity-induced mitochondrial fragmentation in cultured neurons.[243]

With TC-tagged VDAC1, we could visualize VDAC1 dynamics in the context of HK1-ring formation. Although interactions between VDAC1 and HK1 are documented,[129] our observations indicate that VDAC1-clusters do not overlap with HK1-rings during glucose deprivation. This suggests that HK1 can form rings independently of VDAC1, as HK1 can associate to mitochondria without VDAC1.[136] However, HK1 appears to be not able to bind to mitochondria in the absence of both VDAC1 and VDAC2,[244] suggesting that VDAC2 can compensate for the loss of VDAC1 in facilitating the localization of HK1 to the outer mitochondrial membrane. Interestingly, simulations have shown that the mitochondrial binding domain (MBD) of HK1 interacts with the outer wall of VDAC1 and VDAC2,[244] which might explain why mutations in the MBD prevent the formation of HK1-rings. Therefore, further investigations will be necessary to elucidate the roles of VDAC2 in the formation of HK1-rings.

In conclusion, our approach offers a novel method for VDAC1 imaging in live cells, and we expect this technique to significantly enhance our understanding of the role of VDAC1 in cellular processes.

4.5 Limitations and outlook

The discovery that HK1 rings can induce mitochondrial constriction independently of Drp1 represents a novel mechanism in mitochondrial dynamics. It would be intriguing to explore why HK1-rings have such distinct interactions with the different mitochondrial fission receptors. Research into HK1-rings within living animal models, especially under conditions of severe metabolic stress such as exercise, ischemia, and stroke, could shed light on their role in disease processes and overall mammalian physiology. Given the high expression of HK1 in neurons, considering reports of enzyme polymerization being restricted to axons,[22] could also provide valuable insights.

As the crystal structure of HK1-clusters remains unresolved, studying the full-length HK1 protein in the absence of G6P and ATP might reveal how HK1-clusters are organized. Furthermore, assessing the impact of mutations at G6P binding sites in both the N-terminal and C-terminal domains of HK1 could provide deeper insights into how G6P regulates the formation of HK1-rings

Furthermore, a more comprehensive understanding of the long-term implications and interaction partners of HK1-rings, such as the ER or MiD51-rings is essential. While our initial findings from NMR metabolomics indicate that HK1 rings may significantly affect mitochondrial function during periods of energy stress, further research with larger and more varied sample sizes is required to confirm these observations. Collectively, we hope our work will inspire additional investigations into the role of HK1 and other metabolic enzymes in cellular responses to energy stress, potentially unveiling new mechanisms of mitochondrial regulation and cellular adaptation.

While the TC-tag offers significant advantages for studying the dynamics of VDAC1, its impact on the function and conductivity of VDAC1 should be considered. Future research should focus on optimizing tagging methods, such as inserting the TC-tag into the loops of the VDAC1 structure, to minimize potential artifacts. Additionally, exploring a range of cell types will help validate the generalizability of findings. Given that overexpression of VDAC1-TC was associated with mitochondrial fragmentation, it will also be crucial to visualize VDAC1-TC at endogenous levels to accurately assess its physiological role. These steps will enhance our understanding of the role of VDAC1 in cellular processes.

5 References

1. Muñoz, J. & Heck, A. J. R. From the Human Genome to the Human Proteome. *Angew. Chemie Int. Ed.* **53**, 10864–10866 (2014).
2. Jester, J. V. Corneal crystallins and the development of cellular transparency. *Semin. Cell Dev. Biol.* **19**, 82–93 (2008).
3. Ingolia, T. D. & Craig, E. A. Four small Drosophila heat shock proteins are related to each other and to mammalian alpha-crystallin. *Proc. Natl. Acad. Sci. U. S. A.* **79**, 2360–2364 (1982).
4. Iwaki, T., Kume-Iwaki, A., Liem, R. K. & Goldman, J. E. Alpha B-crystallin is expressed in non-lenticular tissues and accumulates in Alexander's disease brain. *Cell* **57**, 71–78 (1989).
5. Bhat, S. P. & Nagineni, C. N. alpha B subunit of lens-specific protein alpha-crystallin is present in other ocular and non-ocular tissues. *Biochem. Biophys. Res. Commun.* **158**, 319–325 (1989).
6. Dubin, R. A., Wawrousek, E. F. & Piatigorsky, J. Expression of the murine alpha B-crystallin gene is not restricted to the lens. *Mol. Cell. Biol.* **9**, 1083–1091 (1989).
7. Wistow, G. J., Mulders, J. W. & de Jong, W. W. The enzyme lactate dehydrogenase as a structural protein in avian and crocodilian lenses. *Nature*

326, 622–624 (1987).

8. Hendriks, W. *et al.* Duck lens epsilon-crystallin and lactate dehydrogenase B4 are identical: a single-copy gene product with two distinct functions. *Proc. Natl. Acad. Sci. U. S. A.* **85**, 7114–7118 (1988).

9. Piatigorsky, J. Multifunctional lens crystallins and corneal enzymes. More than meets the eye. *Ann. N. Y. Acad. Sci.* **842**, 7–15 (1998).

10. Jeffery, C. J. Moonlighting proteins. *Trends Biochem. Sci.* **24**, 8–11 (1999).

11. Chang, C. *et al.* AMPK-Dependent Phosphorylation of GAPDH Triggers Sirt1 Activation and Is Necessary for Autophagy upon Glucose Starvation. *Mol. Cell* **60**, 930–940 (2015).

12. Boukouris, A. E., Zervopoulos, S. D. & Michelakis, E. D. Metabolic Enzymes Moonlighting in the Nucleus: Metabolic Regulation of Gene Transcription. *Trends Biochem. Sci.* **41**, 712–730 (2016).

13. Jiang, X. & Wang, X. Cytochrome C-mediated apoptosis. *Annu. Rev. Biochem.* **73**, 87–106 (2004).

14. Hao, Z. *et al.* Specific ablation of the apoptotic functions of cytochrome C reveals a differential requirement for cytochrome C and Apaf-1 in apoptosis. *Cell* **121**, 579–591 (2005).

15. Jeffery, C. J. Moonlighting proteins. *Trends Biochem. Sci.* **24**, 8–11 (1999).

16. Singh, N. & Bhalla, N. Moonlighting Proteins. *Annu. Rev. Genet.* **54**, 265–285 (2020).

17. Kennedy, M. C., Mende-Mueller, L., Blondin, G. A. & Beinert, H. Purification and characterization of cytosolic aconitase from beef liver and its relationship to the iron-responsive element binding protein. *Proc. Natl. Acad. Sci. U. S. A.* **89**, 11730–11734 (1992).

18. Zheng, L., Kennedy, M. C., Blondin, G. A., Beinert, H. & Zalkin, H. Binding of cytosolic aconitase to the iron responsive element of porcine mitochondrial aconitase mRNA. *Arch. Biochem. Biophys.* **299**, 356–360 (1992).

19. Philpott, C. C., Klausner, R. D. & Rouault, T. A. The bifunctional iron-responsive element binding protein/cytosolic aconitase: the role of active-site

residues in ligand binding and regulation. *Proc. Natl. Acad. Sci. U. S. A.* **91**, 7321–7325 (1994).

20. Espinosa-Cantú, A. *et al.* Protein Moonlighting Revealed by Noncatalytic Phenotypes of Yeast Enzymes. *Genetics* **208**, 419–431 (2018).

21. Narayanaswamy, R. *et al.* Widespread reorganization of metabolic enzymes into reversible assemblies upon nutrient starvation. *Proc. Natl. Acad. Sci. U. S. A.* **106**, 10147–10152 (2009).

22. Noree, C., Sato, B. K., Broyer, R. M. & Wilhelm, J. E. Identification of novel filament-forming proteins in Saccharomyces cerevisiae and Drosophila melanogaster. *J. Cell Biol.* **190**, 541–551 (2010).

23. Shen, Q.-J. *et al.* Filamentation of Metabolic Enzymes in Saccharomyces cerevisiae. *J. Genet. Genomics* **43**, 393–404 (2016).

24. Noree, C. *et al.* A quantitative screen for metabolic enzyme structures reveals patterns of assembly across the yeast metabolic network. *Mol. Biol. Cell* **30**, 2721–2736 (2019).

25. Liu, J.-L. Intracellular compartmentation of CTP synthase in Drosophila. *J. Genet. Genomics* **37**, 281–296 (2010).

26. Pony, P., Rapisarda, C., Terradot, L., Marza, E. & Fronzes, R. Filamentation of the bacterial bi-functional alcohol/aldehyde dehydrogenase AdhE is essential for substrate channeling and enzymatic regulation. *Nat. Commun.* **11**, 1426 (2020).

27. Lynch, E. M., Kollman, J. M. & Webb, B. A. Filament formation by metabolic enzymes-A new twist on regulation. *Curr. Opin. Cell Biol.* **66**, 28–33 (2020).

28. Park, C. K. & Horton, N. C. Structures, functions, and mechanisms of filament forming enzymes: a renaissance of enzyme filamentation. *Biophys. Rev.* **11**, 927–994 (2019).

29. Stoddard, P. R. *et al.* Polymerization in the actin ATPase clan regulates hexokinase activity in yeast. *Science (80-.).* **367**, 1039–1042 (2020).

30. Petrovska, I. *et al.* Filament formation by metabolic enzymes is a specific adaptation to an advanced state of cellular starvation. *Elife* **3**, (2014).

31. Lynch, E. M. *et al.* Human CTP synthase filament structure reveals the active enzyme conformation. *Nat. Struct. Mol. Biol.* **24**, 507–514 (2017).

32. Jin, M. *et al.* Glycolytic Enzymes Coalesce in G Bodies under Hypoxic Stress. *Cell Rep.* **20**, 895–908 (2017).

33. Bitinaite, J. & Schildkraut, I. Self-generated DNA termini relax the specificity of SgrAI restriction endonuclease. *Proc. Natl. Acad. Sci. U. S. A.* **99**, 1164–1169 (2002).

34. Park, C. K. *et al.* Activation of DNA cleavage by oligomerization of DNA-bound SgrAI. *Biochemistry* **49**, 8818–8830 (2010).

35. Shah, S. *et al.* Probing the run-on oligomer of activated SgrAI bound to DNA. *PLoS One* **10**, e0124783 (2015).

36. Goodsell, D. S. & Olson, A. J. Structural symmetry and protein function. *Annu. Rev. Biophys. Biomol. Struct.* **29**, 105–153 (2000).

37. Wild, K., Grafmüller, R., Wagner, E. & Schulz, G. E. Structure, catalysis and supramolecular assembly of adenylate kinase from maize. *Eur. J. Biochem.* **250**, 326–331 (1997).

38. Ingerson-Mahar, M., Briegel, A., Werner, J. N., Jensen, G. J. & Gitai, Z. The metabolic enzyme CTP synthase forms cytoskeletal filaments. *Nat. Cell Biol.* **12**, 739–746 (2010).

39. Barry, R. M. & Gitai, Z. Self-assembling enzymes and the origins of the cytoskeleton. *Curr. Opin. Microbiol.* **14**, 704–711 (2011).

40. Paukštytė, J. *et al.* Global analysis of aging-related protein structural changes uncovers enzyme-polymerization-based control of longevity. *Mol. Cell* **83**, 3360-3376.e11 (2023).

41. Miura, N. Condensate Formation by Metabolic Enzymes in Saccharomyces cerevisiae. *Microorganisms* **10**, (2022).

42. Lynch, E. M. & Kollman, J. M. Coupled structural transitions enable highly cooperative regulation of human CTPS2 filaments. *Nat. Struct. Mol. Biol.* **27**, 42–48 (2020).

43. Hansen, J. M. *et al.* Cryo-EM structures of CTP synthase filaments reveal

mechanism of pH-sensitive assembly during budding yeast starvation. *Elife* **10**, e73368 (2021).

44. Zhang, J., Hulme, L. & Liu, J.-L. Asymmetric inheritance of cytoophidia in Schizosaccharomyces pombe. *Biol. Open* **3**, 1092–1097 (2014).

45. Carcamo, W. C. *et al.* Induction of Cytoplasmic Rods and Rings Structures by Inhibition of the CTP and GTP Synthetic Pathway in Mammalian Cells. *PLoS One* **6**, e29690 (2011).

46. Chen, K. *et al.* Glutamine analogs promote cytoophidium assembly in human and Drosophila cells. *J. Genet. Genomics* **38**, 391–402 (2011).

47. Mishra, B. & Johnson, M. E. Speed limits of protein assembly with reversible membrane localization. *J. Chem. Phys.* **154**, 194101 (2021).

48. Dietrich, H. M. *et al.* Membrane-anchored HDCR nanowires drive hydrogen-powered CO2 fixation. *Nature* **607**, 823–830 (2022).

49. Tanner, L. B. *et al.* Four Key Steps Control Glycolytic Flux in Mammalian Cells. *Cell Syst.* **7**, 49-62.e8 (2018).

50. Webb, B. A., Dosey, A. M., Wittmann, T., Kollman, J. M. & Barber, D. L. The glycolytic enzyme phosphofructokinase-1 assembles into filaments. *J. Cell Biol.* **216**, 2305–2313 (2017).

51. van Schattingen, E. Energy metabolism: Hexokinase/Glucokinase. *Encycl. Biol. Chem. Third Ed.* **1**, 149–161 (2021).

52. Wilson, J. E. Isozymes of mammalian hexokinase: structure, subcellular localization and metabolic function. *J. Exp. Biol.* **206**, 2049–2057 (2003).

53. Middleton, R. J. Hexokinases and glucokinases. *Biochem. Soc. Trans.* **18**, 180–183 (1990).

54. Irwin, D. M. & Tan, H. Molecular evolution of the vertebrate hexokinase gene family: Identification of a conserved fifth vertebrate hexokinase gene. *Comp. Biochem. Physiol. Part D. Genomics Proteomics* **3**, 96–107 (2008).

55. Lowry, O. H. & Passonneau, J. V. The Relationships between Substrates and Enzymes of Glycolysis in Brain. *J. Biol. Chem.* **239**, 31–42 (1964).

56. Ludvik, A. E. *et al.* HKDC1 Is a novel hexokinase involved in Whole-Body

glucose use. *Endocrinology* **157**, 3452–3461 (2016).

57. Federzoni, E. A. *et al.* PU.1 is linking the glycolytic enzyme HK3 in neutrophil differentiation and survival of APL cells. *Blood* **119**, 4963–4970 (2012).

58. Matschinsky, F. M. & Wilson, D. F. The central role of glucokinase in glucose homeostasis: A perspective 50 years after demonstrating the presence of the enzyme in islets of Langerhans. *Front. Physiol.* **10**, 148 (2019).

59. Preller, A. & Wilson, J. E. Localization of the type III isozyme of hexokinase at the nuclear periphery. *Arch. Biochem. Biophys.* **294**, 482–492 (1992).

60. Sui, D. & Wilson, J. E. Structural determinants for the intracellular localization of the isozymes of mammalian hexokinase: Intracellular localization of fusion constructs incorporating structural elements from the hexokinase isozymes and the green fluorescent protein. *Arch. Biochem. Biophys.* **345**, 111–125 (1997).

61. Pusec, C. M. *et al.* Hepatic HKDC1 Expression Contributes to Liver Metabolism. *Endocrinology* **160**, 313–330 (2019).

62. Rose, I. A. & Warms, J. V. B. Mitochondrial Hexokinase. *J. Biol. Chem.* **242**, 1635–1645 (1967).

63. Sun, L., Shukair, S., Naik, T. J., Moazed, F. & Ardehali, H. Glucose phosphorylation and mitochondrial binding are required for the protective effects of hexokinases I and II. *Mol. Cell. Biol.* **28**, 1007–1017 (2008).

64. Depaoli, M. R. *et al.* Real-Time Imaging of Mitochondrial ATP Dynamics Reveals the Metabolic Setting of Single Cells. *Cell Rep.* **25**, 501–512 (2018).

65. Zaid, H., Abu-Hamad, S., Israelson, A., Nathan, I. & Shoshan-Barmatz, V. The voltage-dependent anion channel-1 modulates apoptotic cell death. *Cell Death Differ.* **12**, 751–760 (2005).

66. Arzoine, L., Zilberberg, N., Ben-Romano, R. & Shoshan-Barmatz, V. Voltage-dependent anion channel 1-based peptides interact with hexokinase to prevent its anti-apoptotic activity. *J. Biol. Chem.* **284**, 3946–3955 (2009).

67. Chiara, F., Castellaro, D., Marin, O., Petronilli, V. & Brusilow, W. S. Hexokinase II Detachment from Mitochondria Triggers Apoptosis through the

Permeability Transition Pore Independent of Voltage-Dependent Anion Channels. *PLoS One* **3**, 1852 (2008).

68. Wolf, A. *et al.* Hexokinase 2 is a key mediator of aerobic glycolysis and promotes tumor growth in human glioblastoma multiforme. *J. Exp. Med.* **208**, 313–326 (2011).

69. Schindler, A. & Foley, E. Hexokinase 1 blocks apoptotic signals at the mitochondria. *Cell. Signal.* **25**, 2685–2692 (2013).

70. Machida, K., Ohta, Y. & Osada, H. Suppression of apoptosis by cyclophilin D via stabilization of hexokinase II mitochondrial binding in cancer cells. *J. Biol. Chem.* **281**, 14314–14320 (2006).

71. Roberts, D. J., Tan-Sah, V. P., Smith, J. M. & Miyamoto, S. Akt phosphorylates HK-II at Thr-473 and increases mitochondrial HK-II association to protect cardiomyocytes. *J. Biol. Chem.* **288**, 23798–23806 (2013).

72. De Jesus, A. *et al.* Hexokinase 1 cellular localization regulates the metabolic fate of glucose. *Mol. Cell* **82**, 1261-1277.e9 (2022).

73. Rossi, A. *et al.* Defective Mitochondrial Pyruvate Flux Affects Cell Bioenergetics in Alzheimer's Disease-Related Models. *Cell Rep.* **30**, 2332-2348.e10 (2020).

74. Tatekoshi, Y. *et al.* [WITHDRAWN] Hexokinase-1 mitochondrial dissociation and protein O-GlcNAcylation drive heart failure with preserved ejection fraction. *Research square* at https://doi.org/10.21203/rs.3.rs-2448086/v1 (2023).

75. Rodríguez-Saavedra, C. *et al.* Moonlighting Proteins: The Case of the Hexokinases. *Front. Mol. Biosci.* **8**, 701975 (2021).

76. Mathupala, S. P., Ko, Y. H. & Pedersen, P. L. Hexokinase II: cancer's double-edged sword acting as both facilitator and gatekeeper of malignancy when bound to mitochondria. *Oncogene* **25**, 4777–4786 (2006).

77. Ciscato, F. *et al.* Hexokinase 2 displacement from mitochondria-associated membranes prompts Ca(2+) -dependent death of cancer cells. *EMBO Rep.* **21**, e49117 (2020).

78. Baik, S. H. *et al.* Hexokinase dissociation from mitochondria promotes oligomerization of VDAC that facilitates NLRP3 inflammasome assembly and activation. *Sci. Immunol.* **8**, eade7652 (2023).

79. Thomas, G. E. *et al.* The metabolic enzyme hexokinase 2 localizes to the nucleus in AML and normal haematopoietic stem and progenitor cells to maintain stemness. *Nat. Cell Biol.* **24**, 872–884 (2022).

80. John, S., Weiss, J. N. & Ribalet, B. Subcellular localization of hexokinases I and II directs the metabolic fate of glucose. *PLoS One* **6**, e17674 (2011).

81. Wolf, A. J. *et al.* Hexokinase Is an Innate Immune Receptor for the Detection of Bacterial Peptidoglycan. *Cell* **166**, 624 (2016).

82. Adams, V., Griffin, L. D., Gelb, B. D. & McCabe, E. R. Protein kinase activity of rat brain hexokinase. *Biochem. Biophys. Res. Commun.* **177**, 1101–1106 (1991).

83. Fouquerel, E. *et al.* ARTD1/PARP1 negatively regulates glycolysis by inhibiting hexokinase 1 independent of NAD+ depletion. *Cell Rep.* **8**, 1819–1831 (2014).

84. Kanwal, S. *et al.* Novel homozygous mutations in Pakistani families with Charcot-Marie-Tooth disease. *BMC Med. Genomics* **14**, 174 (2021).

85. Hantke, J. *et al.* A mutation in an alternative untranslated exon of hexokinase 1 associated with hereditary motor and sensory neuropathy -- Russe (HMSNR). *Eur. J. Hum. Genet.* **17**, 1606–1614 (2009).

86. Okur, V. *et al.* De novo variants in HK1 associated with neurodevelopmental abnormalities and visual impairment. *Eur. J. Hum. Genet.* **27**, 1081–1089 (2019).

87. Sullivan, L. S. *et al.* A dominant mutation in hexokinase 1 (HK1) causes retinitis pigmentosa. *Invest. Ophthalmol. Vis. Sci.* **55**, 7147–7158 (2014).

88. Wang, F. *et al.* A missense mutation in HK1 leads to autosomal dominant retinitis pigmentosa. *Invest. Ophthalmol. Vis. Sci.* **55**, 7159–7164 (2014).

89. Rempel, A., Mathupala, S. P., Griffin, C. A., Hawkins, A. L. & Pedersen, P. L. Glucose catabolism in cancer cells: amplification of the gene encoding type II

hexokinase. *Cancer Res.* **56**, 2468–2471 (1996).

90. Bryson, J. M., Coy, P. E., Gottlob, K., Hay, N. & Robey, R. B. Increased hexokinase activity, of either ectopic or endogenous origin, protects renal epithelial cells against acute oxidant-induced cell death. *J. Biol. Chem.* **277**, 11392–11400 (2002).

91. Gottlob, K. *et al.* Inhibition of early apoptotic events by Akt/PKB is dependent on the first committed step of glycolysis and mitochondrial hexokinase. *Genes Dev.* **15**, 1406–1418 (2001).

92. Gao, Y., Xu, D., Yu, G. & Liang, J. Overexpression of metabolic markers HK1 and PKM2 contributes to lymphatic metastasis and adverse prognosis in Chinese gastric cancer. *Int. J. Clin. Exp. Pathol.* **8**, 9264–9271 (2015).

93. Warburg, O. On respiratory impairment in cancer cells. *Science* **124**, 269–270 (1956).

94. Warburg, O. On the origin of cancer cells. *Science* **123**, 309–314 (1956).

95. Lunt, S. Y. & Vander Heiden, M. G. Aerobic glycolysis: meeting the metabolic requirements of cell proliferation. *Annu. Rev. Cell Dev. Biol.* **27**, 441–464 (2011).

96. Brand, K. Glutamine and glucose metabolism during thymocyte proliferation. Pathways of glutamine and glutamate metabolism. *Biochem. J.* **228**, 353–361 (1985).

97. Zu, X. L. & Guppy, M. Cancer metabolism: facts, fantasy, and fiction. *Biochem. Biophys. Res. Commun.* **313**, 459–465 (2004).

98. Fernandez-de-Cossio-Diaz, J. & Vazquez, A. Limits of aerobic metabolism in cancer cells. *Sci. Rep.* **7**, 13488 (2017).

99. Fischer, K. *et al.* Inhibitory effect of tumor cell-derived lactic acid on human T cells. *Blood* **109**, 3812–3819 (2007).

100. García-Cañaveras, J. C., Chen, L. & Rabinowitz, J. D. The Tumor Metabolic Microenvironment: Lessons from Lactate. *Cancer Res.* **79**, 3155–3162 (2019).

101. Abdel-Wahab, A. F., Mahmoud, W. & Al-Harizy, R. M. Targeting glucose

metabolism to suppress cancer progression: prospective of anti-glycolytic cancer therapy. *Pharmacol. Res.* **150**, 104511 (2019).

102. Fulda, S., Galluzzi, L. & Kroemer, G. Targeting mitochondria for cancer therapy. *Nat. Rev. Drug Discov.* **9**, 447–464 (2010).

103. Zhang, D. *et al.* 2-Deoxy-D-glucose targeting of glucose metabolism in cancer cells as a potential therapy. *Cancer Lett.* **355**, 176–183 (2014).

104. Dwarakanath, B. & Jain, V. Targeting glucose metabolism with 2-deoxy-D-glucose for improving cancer therapy. *Future oncology (London, England)* vol. 5 581–585 at https://doi.org/10.2217/fon.09.44 (2009).

105. Muley, P., Olinger, A. & Tummala, H. 2-Deoxyglucose induces cell cycle arrest and apoptosisin colorectal cancer cells independent of its glycolysis inhibition. *Nutr. Cancer* **67**, 514–522 (2015).

106. Dwarakanath, B. S. *et al.* Clinical studies for improving radiotherapy with 2-deoxy-D-glucose: present status and future prospects. *J. Cancer Res. Ther.* **5 Suppl 1**, S21-6 (2009).

107. Chen, Z., Zhang, H., Lu, W. & Huang, P. Role of mitochondria-associated hexokinase II in cancer cell death induced by 3-bromopyruvate. *Biochim. Biophys. Acta* **1787**, 553–560 (2009).

108. Bischof, H. *et al.* Potassium ions promote hexokinase-II dependent glycolysis. *iScience* **24**, 102346 (2021).

109. Pereira da Silva, A. P. *et al.* Inhibition of energy-producing pathways of HepG2 cells by 3-bromopyruvate. *Biochem. J.* **417**, 717–726 (2009).

110. Jae, H. J. *et al.* The antitumor effect and hepatotoxicity of a hexokinase II inhibitor 3-bromopyruvate: in vivo investigation of intraarterial administration in a rabbit VX2 hepatoma model. *Korean J. Radiol.* **10**, 596–603 (2009).

111. Rostovtseva, T. & Colombini, M. ATP flux is controlled by a voltage-gated channel from the mitochondrial outer membrane. *J. Biol. Chem.* **271**, 28006–28008 (1996).

112. Camara, A. K. S., Zhou, Y., Wen, P.-C., Tajkhorshid, E. & Kwok, W.-M. Mitochondrial VDAC1: A Key Gatekeeper as Potential Therapeutic Target.

Front. Physiol. **8**, 460 (2017).

113. Hodge, T. & Colombini, M. Regulation of metabolite flux through voltage-gating of VDAC channels. *J. Membr. Biol.* **157**, 271–279 (1997).

114. Pastorino, J. G., Shulga, N. & Hoek, J. B. Mitochondrial binding of hexokinase II inhibits Bax-induced cytochrome c release and apoptosis. *J. Biol. Chem.* **277**, 7610–7618 (2002).

115. Doran, E. & Halestrap, A. P. Cytochrome c release from isolated rat liver mitochondria can occur independently of outer-membrane rupture: possible role of contact sites. *Biochem. J.* **348 Pt 2**, 343–350 (2000).

116. Shimizu, S., Matsuoka, Y., Shinohara, Y., Yoneda, Y. & Tsujimoto, Y. Essential role of voltage-dependent anion channel in various forms of apoptosis in mammalian cells. *J. Cell Biol.* **152**, 237–250 (2001).

117. Azoulay-Zohar, H., Israelson, A., Abu-Hamad, S. & Shoshan-Barmatz, V. In self-defence: hexokinase promotes voltage-dependent anion channel closure and prevents mitochondria-mediated apoptotic cell death. *Biochem. J.* **377**, 347–355 (2004).

118. Zhou, H. *et al.* Mff-Dependent Mitochondrial Fission Contributes to the Pathogenesis of Cardiac Microvasculature Ischemia/Reperfusion Injury via Induction of mROS-Mediated Cardiolipin Oxidation and HK2/VDAC1 Disassociation-Involved mPTP Opening. *J. Am. Heart Assoc.* **6**, (2017).

119. Arbel, N., Ben-Hail, D. & Shoshan-Barmatz, V. Mediation of the antiapoptotic activity of Bcl-xL protein upon interaction with VDAC1 protein. *J. Biol. Chem.* **287**, 23152–23161 (2012).

120. Banerjee, J. & Ghosh, S. Bax increases the pore size of rat brain mitochondrial voltage-dependent anion channel in the presence of tBid. *Biochem. Biophys. Res. Commun.* **323**, 310–314 (2004).

121. Lan, C. H. *et al.* Involvement of VDAC1 and Bcl-2 family of proteins in VacA-induced cytochrome c release and apoptosis of gastric epithelial carcinoma cells. *J. Dig. Dis.* **11**, 43–49 (2010).

122. Tomasello, F. *et al.* Outer membrane VDAC1 controls permeability transition of the inner mitochondrial membrane in cellulo during stress-induced

apoptosis. *Cell Res.* **19**, 1363–1376 (2009).

123. Pastorino, J. G. & Hoek, J. B. Regulation of hexokinase binding to VDAC. *J. Bioenerg. Biomembr.* **40**, 171–182 (2008).

124. Goldin, N. *et al.* Methyl jasmonate binds to and detaches mitochondria-bound hexokinase. *Oncogene* **27**, 4636–4643 (2008).

125. Shoshan-Barmatz, V. & Golan, M. Mitochondrial VDAC1: function in cell life and death and a target for cancer therapy. *Curr. Med. Chem.* **19**, 714–735 (2012).

126. Simamura, E., Shimada, H., Hatta, T. & Hirai, K.-I. Mitochondrial voltage-dependent anion channels (VDACs) as novel pharmacological targets for anti-cancer agents. *J. Bioenerg. Biomembr.* **40**, 213–217 (2008).

127. Wenner, C. E. Targeting mitochondria as a therapeutic target in cancer. *J. Cell. Physiol.* **227**, 450–456 (2012).

128. Ko, Y. H. *et al.* A translational study 'case report' on the small molecule 'energy blocker' 3-bromopyruvate (3BP) as a potent anticancer agent: from bench side to bedside. *J. Bioenerg. Biomembr.* **44**, 163–170 (2012).

129. Abu-Hamad, S., Zaid, H., Israelson, A., Nahon, E. & Shoshan-Barmatz, V. Hexokinase-I protection against apoptotic cell death is mediated via interaction with the voltage-dependent anion channel-1: mapping the site of binding. *J. Biol. Chem.* **283**, 13482–13490 (2008).

130. Shoshan-Barmatz, V., Zakar, M., Rosenthal, K. & Abu-Hamad, S. Key regions of VDAC1 functioning in apoptosis induction and regulation by hexokinase. *Biochim. Biophys. Acta* **1787**, 421–430 (2009).

131. Abu-Hamad, S. *et al.* The VDAC1 N-terminus is essential both for apoptosis and the protective effect of anti-apoptotic proteins. *J. Cell Sci.* **122**, 1906–1916 (2009).

132. Rosano, C. Molecular model of hexokinase binding to the outer mitochondrial membrane porin (VDAC1): Implication for the design of new cancer therapies. *Mitochondrion* **11**, 513–519 (2011).

133. Zhang, D., Yip, Y. M. & Li, L. In silico construction of HK2-VDAC1 complex

and investigating the HK2 binding-induced molecular gating mechanism of VDAC1. *Mitochondrion* **30**, 222–228 (2016).

134. Haloi, N. *et al.* Structural basis of complex formation between mitochondrial anion channel VDAC1 and Hexokinase-II. *Commun. Biol.* **4**, 667 (2021).

135. Ujwal, R. *et al.* The crystal structure of mouse VDAC1 at 2.3 A resolution reveals mechanistic insights into metabolite gating. *Proc. Natl. Acad. Sci. U. S. A.* **105**, 17742–17747 (2008).

136. Liu, M. Y. & Colombini, M. A soluble mitochondrial protein increases the voltage dependence of the mitochondrial channel, VDAC. *J. Bioenerg. Biomembr.* **24**, 41–46 (1992).

137. Xie, G. C. & Wilson, J. E. Rat brain hexokinase: the hydrophobic N-terminus of the mitochondrially bound enzyme is inserted in the lipid bilayer. *Arch. Biochem. Biophys.* **267**, 803–810 (1988).

138. Bryan, N. & Raisch, K. P. Identification of a mitochondrial-binding site on the N-terminal end of hexokinase II. *Biosci. Rep.* **35**, (2015).

139. Neumann, D., Bückers, J., Kastrup, L., Hell, S. W. & Jakobs, S. Two-color STED microscopy reveals different degrees of colocalization between hexokinase-I and the three human VDAC isoforms. *PMC Biophys.* **3**, 4 (2010).

140. Depaoli, M. R. *et al.* Live cell imaging of signaling and metabolic activities. *Pharmacol. Ther.* **202**, 98–119 (2019).

141. Chandris, P., Giannouli, C. C. & Panayotou, G. Imaging Approaches for the Study of Metabolism in Real Time Using Genetically Encoded Reporters. *Front. cell Dev. Biol.* **9**, 725114 (2021).

142. Shimo, O., Johnson, F. H. & Saiga, Y. Extraction, purification and properties of aequorin, a bioluminescent protein from the luminous hydromedusan, Aequorea. *J. Cell. Comp. Physiol.* **59**, 223–239 (1962).

143. Shimomura, O. The discovery of aequorin and green fluorescent protein. *J. Microsc.* **217**, 1–15 (2005).

144. Chalfie, M., Tu, Y., Euskirchen, G., Ward, W. W. & Prasher, D. C. Green fluorescent protein as a marker for gene expression. *Science* **263**, 802–805

(1994).

145. Inouye, S. & Tsuji, F. I. Aequorea green fluorescent protein. Expression of the gene and fluorescence characteristics of the recombinant protein. *FEBS Lett.* **341**, 277–280 (1994).

146. Prasher, D. C., Eckenrode, V. K., Ward, W. W., Prendergast, F. G. & Cormier, M. J. Primary structure of the Aequorea victoria green-fluorescent protein. *Gene* **111**, 229–233 (1992).

147. Rodriguez, E. A. *et al.* The Growing and Glowing Toolbox of Fluorescent and Photoactive Proteins. *Trends Biochem. Sci.* **42**, 111–129 (2017).

148. Shaner, N. C., Steinbach, P. A. & Tsien, R. Y. A guide to choosing fluorescent proteins. *Nat. Methods* **2**, 905–909 (2005).

149. Deponte, M. GFP tagging sheds light on protein translocation: implications for key methods in cell biology. *Cell. Mol. Life Sci.* **69**, 1025–1033 (2012).

150. Kim, J. Y., Yuan, Z., Cilia, M., Khalfan-Jagani, Z. & Jackson, D. Intercellular trafficking of a KNOTTED1 green fluorescent protein fusion in the leaf and shoot meristem of Arabidopsis. *Proc. Natl. Acad. Sci. U. S. A.* **99**, 4103–4108 (2002).

151. Wilson, C. G. M., Magliery, T. J. & Regan, L. Detecting protein-protein interactions with GFP-fragment reassembly. *Nat. Methods* **1**, 255–262 (2004).

152. Westermann, B. & Neupert, W. Mitochondria-targeted green fluorescent proteins: convenient tools for the study of organelle biogenesis in Saccharomyces cerevisiae. *Yeast* **16**, 1421–1427 (2000).

153. Akimzhanov, A. M. & Boehning, D. Monitoring dynamic changes in mitochondrial calcium levels during apoptosis using a genetically encoded calcium sensor. *J. Vis. Exp.* (2011) doi:10.3791/2579.

154. Simonova, M., Weissleder, R., Sergeyev, N., Vilissova, N. & Bogdanov, A. J. Targeting of green fluorescent protein expression to the cell surface. *Biochem. Biophys. Res. Commun.* **262**, 638–642 (1999).

155. Eroglu, E. *et al.* Development of novel FP-based probes for live-cell imaging of nitric oxide dynamics. *Nat. Commun.* **7**, 10623 (2016).

156. Bischof, H. *et al.* Novel genetically encoded fluorescent probes enable real-time detection of potassium in vitro and in vivo. *Nat. Commun.* **8**, 1422 (2017).

157. Tsou, P., Zheng, B., Hsu, C.-H., Sasaki, A. T. & Cantley, L. C. A fluorescent reporter of AMPK activity and cellular energy stress. *Cell Metab.* **13**, 476–486 (2011).

158. Zhou, X. *et al.* Dynamic Visualization of mTORC1 Activity in Living Cells. *Cell Rep.* **10**, 1767–1777 (2015).

159. Chi, W.-Y. *et al.* Imaging and analysis for simultaneous tracking of fluorescent biosensors in barcoded cells. *STAR Protoc.* **3**, 101611 (2022).

160. Spiering, D., Bravo-Cordero, J. J., Moshfegh, Y., Miskolci, V. & Hodgson, L. Quantitative ratiometric imaging of FRET-biosensors in living cells. *Methods Cell Biol.* **114**, 593–609 (2013).

161. Waldeck-Weiermair, M. *et al.* Generation of Red-Shifted Cameleons for Imaging Ca^{2+} Dynamics of the Endoplasmic Reticulum. *Sensors (Basel).* **15**, 13052–13068 (2015).

162. Wu, J. *et al.* Red fluorescent genetically encoded Ca2+ indicators for use in mitochondria and endoplasmic reticulum. *Biochem. J.* **464**, 13–22 (2014).

163. Asgari, Y., Zabihinpour, Z., Salehzadeh-Yazdi, A., Schreiber, F. & Masoudi-Nejad, A. Alterations in cancer cell metabolism: The Warburg effect and metabolic adaptation. *Genomics* **105**, 275–281 (2015).

164. Bezprozvanny, I. B. Calcium signaling and neurodegeneration. *Acta Naturae* **2**, 72–82 (2010).

165. Costantino, S., Paneni, F. & Cosentino, F. Ageing, metabolism and cardiovascular disease. *J. Physiol.* **594**, 2061–2073 (2016).

166. Chandrasekharan, A. *et al.* A high-throughput real-time in vitro assay using mitochondrial targeted roGFP for screening of drugs targeting mitochondria. *Redox Biol.* **20**, 379–389 (2019).

167. Glancy, B. Visualizing Mitochondrial Form and Function within the Cell. *Trends Mol. Med.* **26**, 58–70 (2020).

168. Zhang, H. *et al.* NAD^+ repletion improves mitochondrial and stem cell function

and enhances life span in mice. *Science* **352**, 1436–1443 (2016).

169. Weidberg, H. & Amon, A. MitoCPR-A surveillance pathway that protects mitochondria in response to protein import stress. *Science* **360**, (2018).

170. Gray, M. W. Mosaic nature of the mitochondrial proteome: Implications for the origin and evolution of mitochondria. *Proc. Natl. Acad. Sci.* **112**, 10133–10138 (2015).

171. Perry, S. W., Norman, J. P., Barbieri, J., Brown, E. B. & Gelbard, H. A. Mitochondrial membrane potential probes and the proton gradient: a practical usage guide. *Biotechniques* **50**, 98–115 (2011).

172. Irgen-Gioro, S., Yoshida, S., Walling, V. & Chong, S. Fixation can change the appearance of phase separation in living cells. *Elife* **11**, e79903 (2022).

173. Segawa, M. *et al.* Quantification of cristae architecture reveals time-dependent characteristics of individual mitochondria. *Life Sci. alliance* **3**, (2020).

174. Gottschalk, B., Klec, C., Waldeck-Weiermair, M., Malli, R. & Graier, W. F. Intracellular Ca2+ release decelerates mitochondrial cristae dynamics within the junctions to the endoplasmic reticulum. *Pflügers Arch. - Eur. J. Physiol.* **470**, 1193–1203 (2018).

175. Gottschalk, B. *et al.* MICU1 controls cristae junction and spatially anchors mitochondrial Ca(2+) uniporter complex. *Nat. Commun.* **10**, 3732 (2019).

176. Kremers, G.-J., Gilbert, S. G., Cranfill, P. J., Davidson, M. W. & Piston, D. W. Fluorescent proteins at a glance. *J. Cell Sci.* **124**, 157–160 (2011).

177. Rapizzi, E. *et al.* Recombinant expression of the voltage-dependent anion channel enhances the transfer of Ca2+ microdomains to mitochondria. *J. Cell Biol.* **159**, 613–624 (2002).

178. Dubey, A. K., Godbole, A. & Mathew, M. K. Regulation of VDAC trafficking modulates cell death. *Cell death Discov.* **2**, 16085 (2016).

179. Kozjak-Pavlovic, V., Ross, K., Götz, M., Goosmann, C. & Rudel, T. A Tag at the Carboxy Terminus Prevents Membrane Integration of VDAC1 in Mammalian Mitochondria. *J. Mol. Biol.* **397**, 219–232 (2010).

180. Jores, T. *et al.* Characterization of the targeting signal in mitochondrial β-barrel proteins. *Nat. Commun.* **7**, 12036 (2016).

181. Feng, S. *et al.* Improved split fluorescent proteins for endogenous protein labeling. *Nat. Commun.* **8**, 370 (2017).

182. Griffin, B. A., Adams, S. R. & Tsien, R. Y. Specific covalent labeling of recombinant protein molecules inside live cells. *Science* **281**, 269–272 (1998).

183. Hoffmann, C. *et al.* Fluorescent labeling of tetracysteine-tagged proteins in intact cells. *Nat. Protoc.* **5**, 1666–1677 (2010).

184. Pilic, J. *et al.* Hexokinase 1 forms rings that regulate mitochondrial fission during energy stress. *Mol. Cell* (2024) doi:10.1016/j.molcel.2024.06.009.

185. Pilic, J. *et al.* Visualizing interactions of VDAC1 in live cells using a tetracysteine tag. *bioRxiv* 2023.09.08.556841 (2023) doi:10.1101/2023.09.08.556841.

186. Kreuzer, K. *et al.* The PROVIT Study-Effects of Multispecies Probiotic Add-on Treatment on Metabolomics in Major Depressive Disorder-A Randomized, Placebo-Controlled Trial. *Metabolites* **12**, (2022).

187. Zhang, F. *et al.* Tissue-Specific Landscape of Metabolic Dysregulation during Ageing. *Biomolecules* **11**, (2021).

188. Bischof, H. *et al.* Potassium ions promote hexokinase-II dependent glycolysis Highlights HKII expression sensitizes cellular metabolism for intracellular K Intracellular K + depletion abates the metabolic activity of HKII-positive cells (Re-)elevations of intracellular K + r. doi:10.1016/j.isci.2021.102346.

189. Zeng, C., Aleshin, A. E., Chen, G., Honzatko, R. B. & Fromm, H. J. The Roles of Glycine Residues in the ATP Binding Site of Human Brain Hexokinase. *J. Biol. Chem.* **273**, 700–704 (1998).

190. Aleshin, A. E. *et al.* Crystal structures of mutant monomeric hexokinase I reveal multiple ADP binding sites and conformational changes relevant to allosteric regulation. *J. Mol. Biol.* **296**, 1001–1015 (2000).

191. Ramadani-Muja, J. *et al.* Visualization of Sirtuin 4 Distribution between Mitochondria and the Nucleus, Based on Bimolecular Fluorescence Self-

Complementation. *Cells* **8**, (2019).

192. Waldeck-Weiermair, M. *et al.* Development and Application of Sub-Mitochondrial Targeted Ca2 + Biosensors. *Front. Cell. Neurosci.* **13**, (2019).

193. Wong, Y. C. *et al.* Mid51/Fis1 mitochondrial oligomerization complex drives lysosomal untethering and network dynamics. *J. Cell Biol.* **221**, (2022).

194. Takanaga, H., Chaudhuri, B. & Frommer, W. B. GLUT1 and GLUT9 as major contributors to glucose influx in HepG2 cells identified by a high sensitivity intramolecular FRET glucose sensor. *Biochim. Biophys. Acta* **1778**, 1091–1099 (2008).

195. Moore, I. & Murphy, A. Validating the location of fluorescent protein fusions in the endomembrane system. *Plant Cell* **21**, 1632–1636 (2009).

196. Imamura, H. *et al.* Visualization of ATP levels inside single living cells with fluorescence resonance energy transfer-based genetically encoded indicators. *Proc. Natl. Acad. Sci. U. S. A.* **106**, 15651–15656 (2009).

197. Fang, T. Y., Alechina, O., Aleshin, A. E., Fromm, H. J. & Honzatko, R. B. Identification of a phosphate regulatory site and a low affinity binding site for glucose 6-phosphate in the N-terminal half of human brain hexokinase. *J. Biol. Chem.* **273**, 19548–19553 (1998).

198. Ellison, W. R., Lueck, J. D. & Fromm, H. J. Studies on the mechanism of orthophosphate regulation of bovine brain hexokinase. *J. Biol. Chem.* **250**, 1864–1871 (1975).

199. Drake, J. C. *et al.* Mitochondria-localized AMPK responds to local energetics and contributes to exercise and energetic stress-induced mitophagy. *Proc. Natl. Acad. Sci. U. S. A.* **118**, (2021).

200. Korobova, F., Ramabhadran, V. & Higgs, H. N. An Actin-Dependent Step in Mitochondrial Fission Mediated by the ER-Associated Formin INF2. *Science (80-.).* **339**, 464–467 (2013).

201. Manor, U. *et al.* A mitochondria-anchored isoform of the actin-nucleating spire protein regulates mitochondrial division. *Elife* **4**, e08828 (2015).

202. Friedman, J. R. *et al.* ER tubules mark sites of mitochondrial division. *Science*

334, 358–362 (2011).

203. Nguyen, T. T. & Voeltz, G. K. An ER phospholipid hydrolase drives ER-associated mitochondrial constriction for fission and fusion. *Elife* **11**, e84279 (2022).

204. Lewis, S. C., Uchiyama, L. F. & Nunnari, J. ER-mitochondria contacts couple mtDNA synthesis with mitochondrial division in human cells. *Science* **353**, aaf5549 (2016).

205. Kraus, F., Roy, K., Pucadyil, T. J. & Ryan, M. T. Function and regulation of the divisome for mitochondrial fission. *Nature* **590**, 57–66 (2021).

206. Kleele, T. *et al.* Distinct fission signatures predict mitochondrial degradation or biogenesis. *Nature* **593**, 435–439 (2021).

207. Yoshii, S. R., Kishi, C., Ishihara, N. & Mizushima, N. Parkin Mediates Proteasome-dependent Protein Degradation and Rupture of the Outer Mitochondrial Membrane*♦. *J. Biol. Chem.* **286**, 19630–19640 (2011).

208. Van Laar, V. S. *et al.* Bioenergetics of neurons inhibit the translocation response of Parkin following rapid mitochondrial depolarization. *Hum. Mol. Genet.* **20**, 927–940 (2011).

209. Ardehali, H. *et al.* Functional organization of mammalian hexokinase II. Retention of catalytic and regulatory functions in both the NH2- and COOH-terminal halves. *J. Biol. Chem.* **271**, 1849–1852 (1996).

210. Ford, M. G. J. *et al.* Curvature of clathrin-coated pits driven by epsin. *Nature* **419**, 361–366 (2002).

211. Lee, M. C. S. *et al.* Sar1p N-terminal helix initiates membrane curvature and completes the fission of a COPII vesicle. *Cell* **122**, 605–617 (2005).

212. Aleshin, A. E. E. *et al.* Nonaggregating mutant of recombinant human hexokinase I exhibits wild-type kinetics and rod-like conformations in solution. *Biochemistry* **38**, 8359–8366 (1999).

213. Xie, G. & Wilson, J. E. Tetrameric structure of mitochondrially bound rat brain hexokinase: a crosslinking study. *Arch. Biochem. Biophys.* **276**, 285–293 (1990).

214. Beutner, G., Rück, A., Riede, B. & Brdiczka, D. Complexes between porin, hexokinase, mitochondrial creatine kinase and adenylate translocator display properties of the permeability transition pore. Implication for regulation of permeability transition by the kinases. *Biochim. Biophys. Acta* **1368**, 7–18 (1998).

215. Shoshan-Barmatz, V., Krelin, Y., Shteinfer-Kuzmine, A. & Arif, T. Voltage-Dependent Anion Channel 1 As an Emerging Drug Target for Novel Anti-Cancer Therapeutics. *Front. Oncol.* **7**, 154 (2017).

216. Durel, B., Kervrann, C. & Bertolin, G. Quantitative dSTORM super-resolution microscopy localizes Aurora kinase A/AURKA in the mitochondrial matrix. *Biol. cell* **113**, 458–473 (2021).

217. Szabadkai, G. *et al.* Chaperone-mediated coupling of endoplasmic reticulum and mitochondrial Ca2+ channels. *J. Cell Biol.* **175**, 901–911 (2006).

218. Liu, Y. *et al.* DJ-1 regulates the integrity and function of ER-mitochondria association through interaction with IP3R3-Grp75-VDAC1. *Proc. Natl. Acad. Sci. U. S. A.* **116**, 25322–25328 (2019).

219. Tajeddine, N. *et al.* Hierarchical involvement of Bak, VDAC1 and Bax in cisplatin-induced cell death. *Oncogene* **27**, 4221–4232 (2008).

220. Calmettes, G., John, S. A. A., Weiss, J. N. N. & Ribalet, B. Hexokinase-mitochondrial interactions regulate glucose metabolism differentially in adult and neonatal cardiac myocytes. *J. Gen. Physiol.* **142**, 425–436 (2013).

221. Aleshin, A. E., Zeng, C., Bartunik, H. D., Fromm, H. J. & Honzatko, R. B. Regulation of hexokinase I: crystal structure of recombinant human brain hexokinase complexed with glucose and phosphate. *J. Mol. Biol.* **282**, 345–357 (1998).

222. Aleshin, A. E., Fromm, H. J. & Honzatko, R. B. Multiple crystal forms of hexokinase I: New insights regarding conformational dynamics, subunit interactions, and membrane association. *FEBS Lett.* **434**, 42–46 (1998).

223. Melnyk, R. A. *et al.* The Affinity of GXXXG Motifs in Transmembrane Helix-Helix Interactions Is Modulated by Long-range Communication. *J. Biol. Chem.* **279**, 16591–16597 (2004).

224. Wu, T., Shi, Z. & Baumgart, T. Mutations in BIN1 Associated with Centronuclear Myopathy Disrupt Membrane Remodeling by Affecting Protein Density and Oligomerization. *PLoS One* **9**, e93060 (2014).

225. Zhang, J. *et al.* c-Src phosphorylation and activation of hexokinase promotes tumorigenesis and metastasis. *Nat. Commun.* **8**, 13732 (2017).

226. Vargas-Mendoza, N. *et al.* Oxidative Stress, Mitochondrial Function and Adaptation to Exercise: New Perspectives in Nutrition. *Life* **11**, (2021).

227. Stanley, W. C. Myocardial energy metabolism during ischemia and the mechanisms of metabolic therapies. *J. Cardiovasc. Pharmacol. Ther.* **9**, S31-45 (2004).

228. Arai, K. *et al.* Cellular mechanisms of neurovascular damage and repair after stroke. *J. Child Neurol.* **26**, 1193–1198 (2011).

229. Sassano, M. L., Felipe-Abrio, B. & Agostinis, P. ER-mitochondria contact sites; a multifaceted factory for Ca(2+) signaling and lipid transport. *Front. cell Dev. Biol.* **10**, 988014 (2022).

230. Bork, P., Sander, C. & Valencia, A. An ATPase domain common to prokaryotic cell cycle proteins, sugar kinases, actin, and hsp70 heat shock proteins. *Proc. Natl. Acad. Sci. U. S. A.* **89**, 7290–7294 (1992).

231. Lackner, L. L. & Nunnari, J. Small molecule inhibitors of mitochondrial division: tools that translate basic biological research into medicine. *Chem. Biol.* **17**, 578–583 (2010).

232. Si, L. *et al.* Silibinin-induced mitochondria fission leads to mitophagy, which attenuates silibinin-induced apoptosis in MCF-7 and MDA-MB-231 cells. *Arch. Biochem. Biophys.* **685**, 108284 (2020).

233. Guo, X. *et al.* Inhibition of mitochondrial fragmentation diminishes Huntington's disease-associated neurodegeneration. *J. Clin. Invest.* **123**, 5371–5388 (2013).

234. Disatnik, M. *et al.* Acute Inhibition of Excessive Mitochondrial Fission After Myocardial Infarction Prevents Long-term Cardiac Dysfunction. *J. Am. Heart Assoc.* **2**, e000461 (2013).

235. Ngo, J. *et al.* Mitochondrial morphology controls fatty acid utilization by changing CPT1 sensitivity to malonyl-CoA. *EMBO J.* **42**, e111901 (2023).

236. Galloway, C. A. & Yoon, Y. Mitochondrial morphology in metabolic diseases. *Antioxid. Redox Signal.* **19**, 415–430 (2013).

237. Mishra, P. & Chan, D. C. Metabolic regulation of mitochondrial dynamics. *J. Cell Biol.* **212**, 379–387 (2016).

238. Zhang, L. *et al.* Altered brain energetics induces mitochondrial fission arrest in Alzheimer's Disease. *Sci. Rep.* **6**, 18725 (2016).

239. Morozov, Y. M., Datta, D., Paspalas, C. D. & Arnsten, A. F. T. Ultrastructural evidence for impaired mitochondrial fission in the aged rhesus monkey dorsolateral prefrontal cortex. *Neurobiol. Aging* **51**, 9–18 (2017).

240. Panes, J. *et al.* Partial Inhibition of Complex I Restores Mitochondrial Morphology and Mitochondria-ER Communication in Hippocampus of APP/PS1 Mice. *Cells* **12**, (2023).

241. Polianskyte, Z. *et al.* LACTB is a filament-forming protein localized in mitochondria. *Proc. Natl. Acad. Sci. U. S. A.* **106**, 18960–18965 (2009).

242. Adamoski, D. *et al.* Molecular mechanism of glutaminase activation through filamentation and the role of filaments in mitophagy protection. *Nat. Struct. Mol. Biol.* **30**, 1902–1912 (2023).

243. Oppermann, S. *et al.* Interaction between BID and VDAC1 is required for mitochondrial demise and cell death in neurons. *bioRxiv* 2021.09.14.460262 (2021) doi:10.1101/2021.09.14.460262.

244. Bieker, S. *et al.* Hexokinase-I directly binds to a charged membrane-buried glutamate of mitochondrial VDAC1 and VDAC2. *bioRxiv* 2024.07.22.604557 (2024) doi:10.1101/2024.07.22.604557.